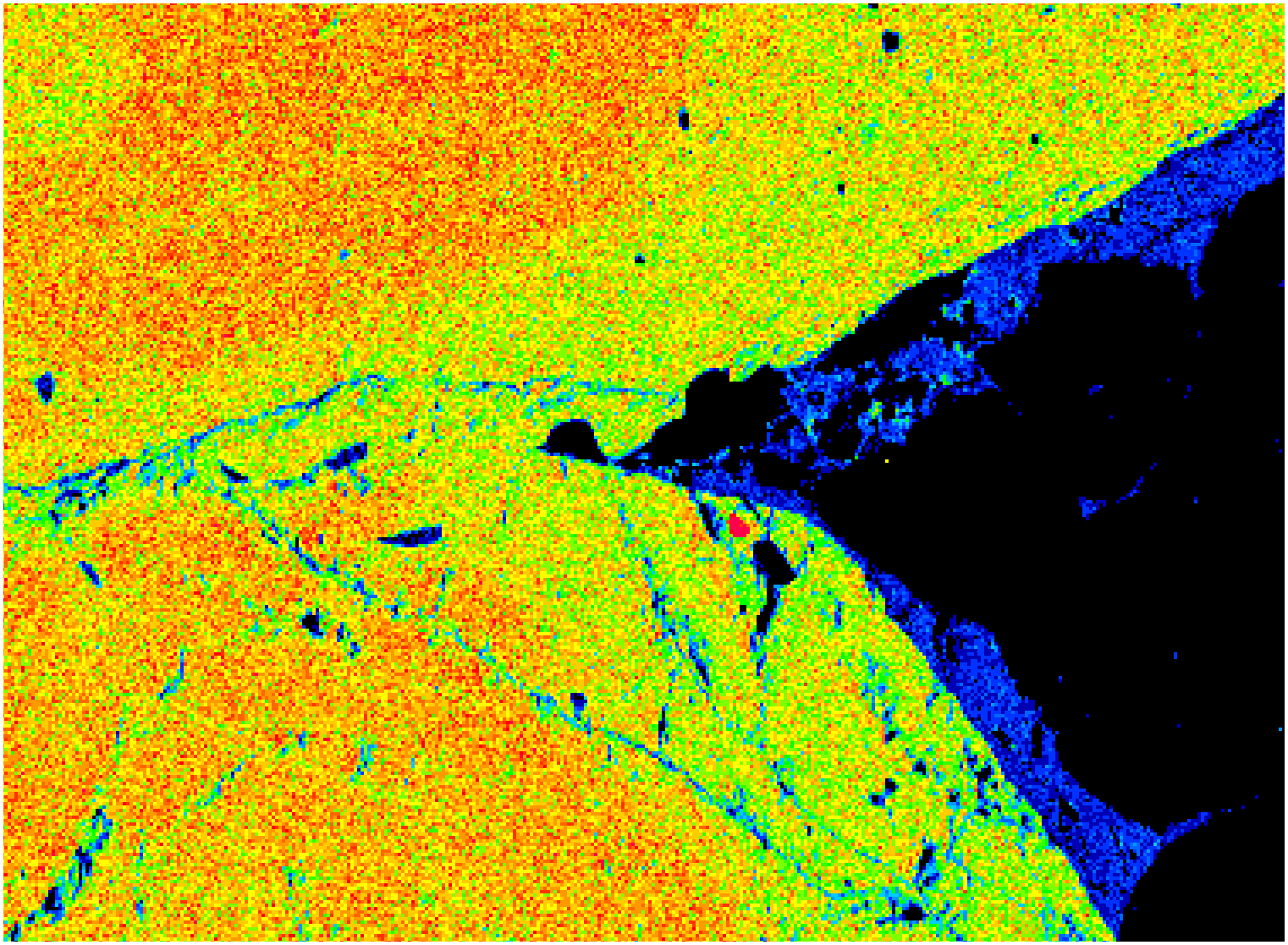

2018 ANNUAL REPORT

HP-HT laboratory

EXPERIMENTAL VOLCANOLOGY AND GEOPHYSICS

laboratory

NEW TECHNOLOGIES

Department of Seismology and Tectonophysics
Istituto Nazionale di Geofisica e Vulcanologia

Via di Vigna Murata 605 | 00143 Roma - Italia | Tel +39-0651860437 | Fax +39-0651860507
www.ingv.it

About the cover:

Electron Micro-Probe (EMP) chemical map of two clinopyroxene crystals from Stromboli volcano (eruption of 01/11/2017).

Credits:

Flavio Di Stefano

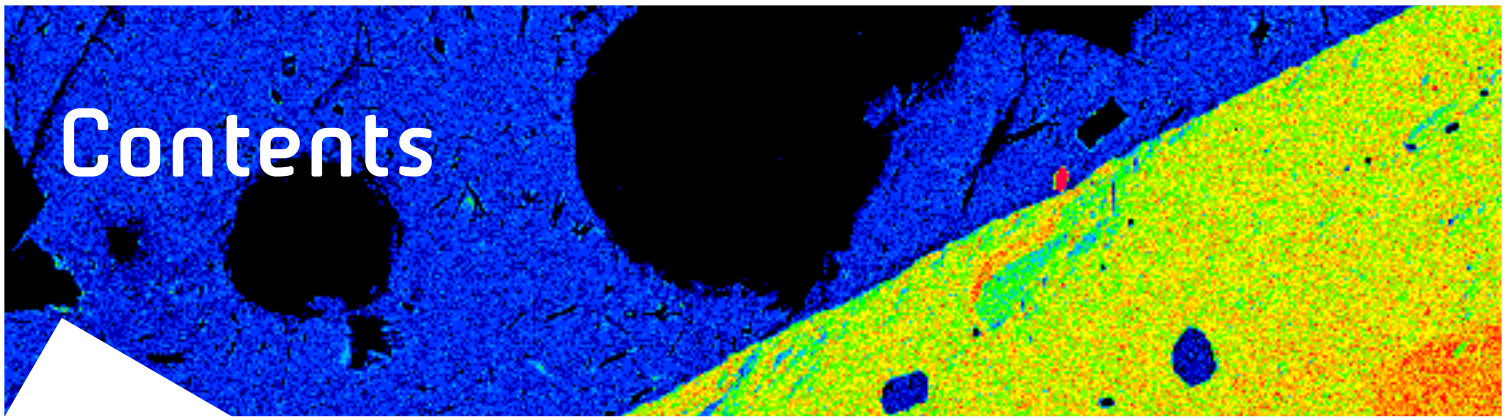

Contents

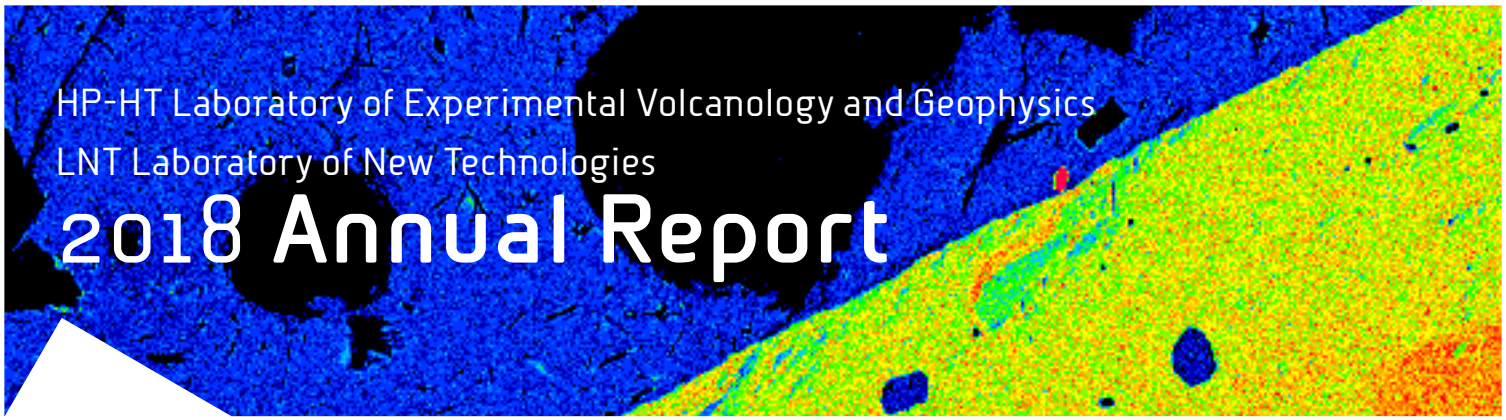

HP-HT Laboratory of Experimental Volcanology and Geophysics

LNT Laboratory of New Technologies

2018 Annual Report

1| ABSTRACT

In this annual report, we have summarized the most important research activities of the High Pressure High Temperature Laboratory of Experimental Volcanology and Geophysics and of the Laboratory of New Technologies that were conducted in 2018. The Labs hosted 4 full-time visiting scientists, 10 associated researchers, 15 PhD/Master students. During this year, 13 national- to international-level projects/collaborations were active, involving more than 9 partner laboratories and institutions. As part of the EPOS TCS 'Multiscale Laboratories' 2nd pilot call for Trans-National Access (TNA) activities, the HPHT lab has hosted two international scientists whose proposals were accepted for physical access.

The HPHT Lab continued its numerous research studies in petrology, mineralogy and volcanology (22 studies) and in rock physics (10 studies), whereas the LNTS Lab designed and developed new measuring systems, sensors and instrumentations (8 prototypes), and submitted 2 patent applications.

Finally, the Lab personnel have organized and participated to 7 meetings, workshops and seminars in Italy and abroad, and have published 37 cientific articles in the most important international journals.

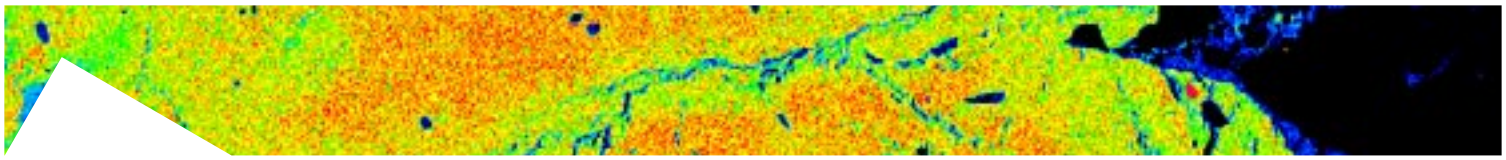

2I PERSONNEL

HPHT Laboratory

Piergiorgio Scarlato I Senior Researcher, Responsible of the HP-HT group

Stefano Aretusini I Contract Researcher

Gianfilippo De Astis I Researcher

Elisabetta Del Bello I Researcher

Christopher Harbord I Contract Researcher

Valeria Misiti I Technologist

Manuela Nazzari I Researcher

Tullio Ricci I Researcher

Elena Spagnuolo I Contract Researcher

Laura Spina I Researcher

Jacopo Taddeucci I Senior Researcher

Laboratory of New Technologies

Giovanni Romeo I Technical Director, Responsible of the Laboratory of New Technologies

Giuseppe Di Stefano I Senior Technologist

Alessandro Iarocci I Engineer Technologist

Massimo Mari I Technician

Francesco Pongetti I Engineer Technician

Giuseppe Spinelli I Engineer Technologist

Mario Tozzi I Engineer Technologist

Giuseppe Urbini I Engineer Technologist

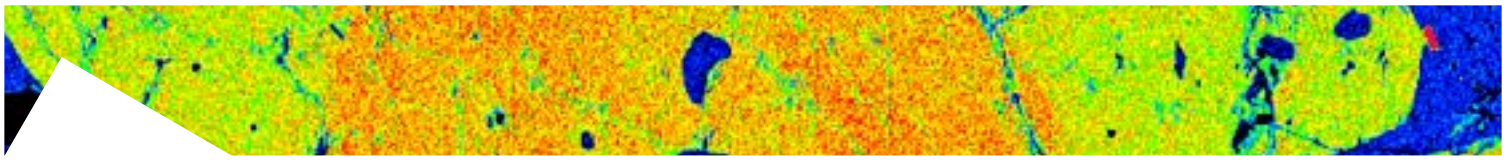

Associated researchers

Cristiano Collettini I Sapienza Università di Roma, Italy **I Associate Professor in Structural Geology**

Frances M. Deegan I Uppsala University, Sweden **I Researcher**

Giancarlo Della Ventura I Università di Roma Tre **I Full Professor in Mineralogy**

Giulio Di Toro I Università degli Studi di Padova, Italy **I Full Professor in Structural Geology**

Gianluca Iezzi I Università di Chieti, Italy **I Associate Professor in Mineralogy**

Silvio Mollo I Sapienza Università di Roma, Italy **I Associate Professor of Petrology**

Valentin R. Troll I Uppsala University, Sweden **I Chair of Petrology**

Collaborators

Matteo Masotta I Università di Pisa, Italy **I Researcher**

Marco M. Scuderi I Sapienza Università di Roma, Italy **I Marie Curie Fellow**

Vincenzo Stagno I Sapienza Università di Roma, Italy **I Researcher**

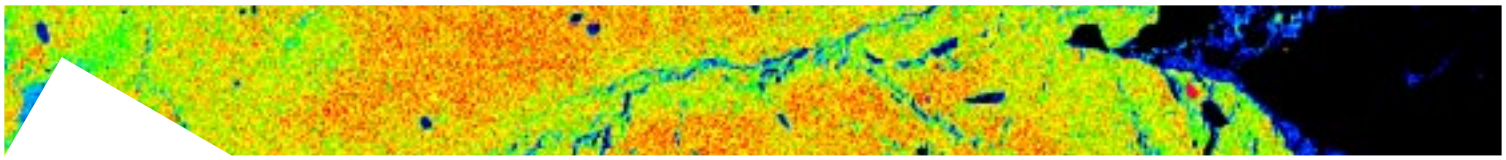

3I INSTRUMENTS and FACILITIES

HPHT Laboratory

- Multiple press 840 ton **|** Voggenreiter
- Piston cylinder - 3/4" and 1" pressure plates **|** Voggenreiter
- Multianvil - Walker type 6/8 **|** Voggenreiter
- Quick Press - Piston Cylinder 3/4" and 1" pressure plates **|** Depth of the Earth
- Bi-Tri-Axial Press (BRAVA) **|** RMP - INGV
- Low to High Velocity Apparatus (SHIVA) **|** RMP - INGV
- Electron microprobe equipped with 5 WDS and 1 EDS **|** JEOL JXA-8200
- Field Emission Scanning Electron Microscope equipped with EDS and BSE detectors **|** JEOL JSM-6500F
- Auto Carbon coater **|** JEOL JEC-530
- Fine coater **|** JEOL JFC-2300HR
- High and low temperature furnaces **|** Lenton
- Impedance analyser **|** Solartron SI1260
- Digital oscilloscope **|** Tektronix DPO4032
- Wave generator **|** Agilent 33250A
- H-Frame presses 10 ton **|** Enerpac
- Uniaxial testing machine with double load cell (15 and 250 kN) and LVDT controller **|** Tecnotest
- Precision balance **|** Sartorius
- Optical and stereo microscopes **|** Leica DMRXP and Euromex
- Ultra-high velocity, intensified, gated digital camera **|** Cordin 204-2
- High speed digital camcorder **|** Optronis and NAC 512 SC
- Stereomicroscopes **|** Leica MZ 9.5

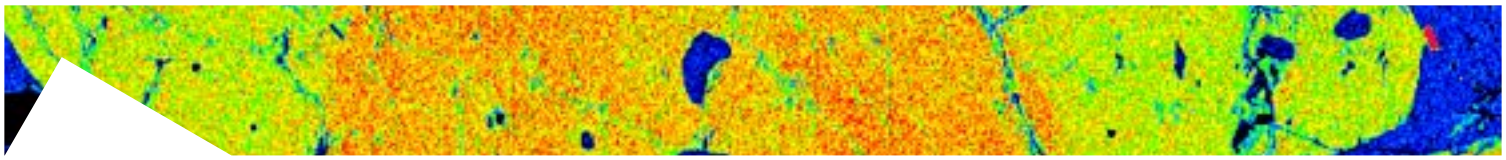

- Semiautomatic polisher **|** Buehler Minimet 1000
- Power Supply **|** Agilent 6575A
- Helium Picnometer **|** AccuPyc II 1340
- Permeameter with double intensifier **|** Rock Physics
- Rheometer MCR 301 Physica **|** Anton Paar
- Vertical Furnace RHTV 120-300/18 **|** Nabertherm
- High Temperature Furnace LHT 04/18 **|** Nabertherm
- Cecchi data acquisition system **|** Applied Seismology
- Rock drilling, cutting, and grinding equipment for samples preparation
- Thermal High speed camera **|** FLIR SC 645
- Welder PUK U3 **|** Lampert
- Laser line generator **|** Edmund optics
- Precision test sieves **|** Endecotts
- Laser MGL-III, 532nm 200mW, PSU-III-LED/Unit **|** Changchun New Industries
- Multi-Wavelenght Analyser with Particle sizing according to ISO 13317 **|** LUMiReader@PSA
- Polarized Free-field Microphones 40AN 1/2", Low Frequency (0.5Hz - 20kHz) **|** G.R.A.S.
- Vacuometro PVG-500 **|** Pirani
- Petrographic microscope ECLIPSE E-50i POL **|** Nikon
- Drying oven UF 75 **|** Memmert
- 4K digital camcorders **|** Sony
- High speed digital camcorder **|** NAC Memrecam-HX6
- Shock-tube apparatus (Jet-Buster) **|** INGV
- High speed digital camcorders **|** NAC 512 SC, Optronis CR600x2, NAC HX6, NAC HX3
- Laser range finder **|** Vectronix VECTOR 21

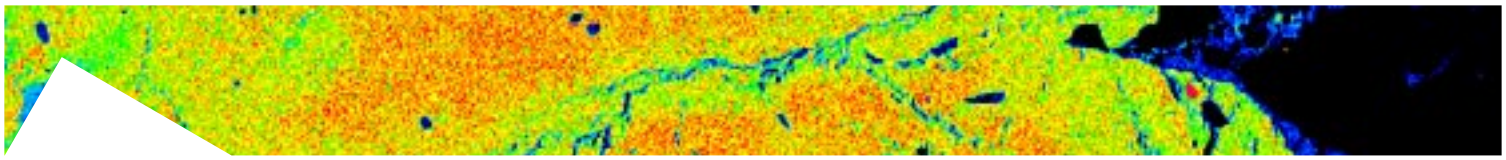

- Time Lapse Camera with 24-70 lens **|** Brinno TLC200 Pro

Acquired in 2018

- Precision Syringe Pumps **|** ISCO
- Ash dispersal/settling apparatus (Ash-Buster) **|** INGV

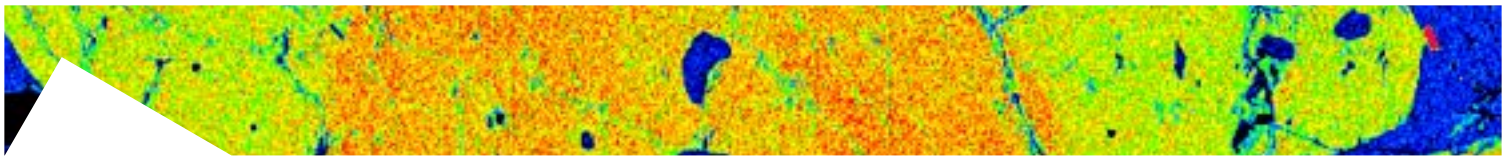

Laboratory of New Technologies

- Analog Oscilloscope | HP
- Analog Oscilloscope | Iwatsu SS5710
- Analog Oscilloscope | Tektronix TDS220
- Analog Oscilloscope | Tektronix
- Oscilloscope | HP54201
- Oscilloscope | HP54602b
- Power supply | Elind HL series
- Power supply | Elind 6TD20
- Power supply | DC DF1731SB
- Signal generator | HP8656A
- Function generator | HP3325A
- Multimeter | HP3478A
- Milling machine for printed circuit boards | T-Tech
- Logic state analyzer | HP16500A
- Superheterodyne spectrum analyzer | Tektronix
- Soldering-reworking station | JBC advanced AM6500
- Oscilloscope | FLUKE 199C
- Oscilloscope | Tektronix DPO4000
- Oscilloscope | Tektronix MSO4034
- Calibrator | FLUKE 5700 (series II)
- Function generator | HP33120
- Function generator | AGILENT 33250 A
- PXI Industrial computer with I/O boards | National Instruments

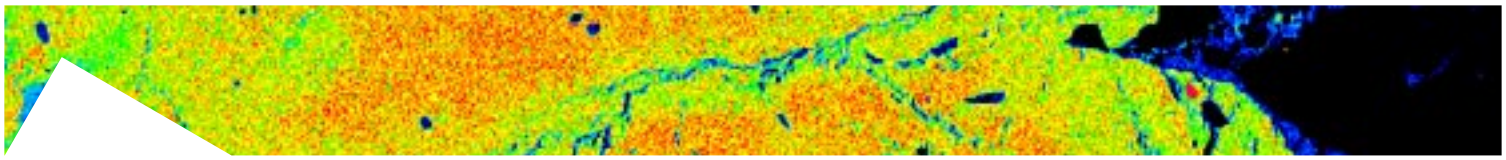

- Universal counter | HP53131A
- Waveform generator | Agilent 33210 A
- Oscilloscope W wave surfer | LeCroy 44MXs-A
- Drone Phantom 3 pro with termination system

Machine shop

- Lathe | Grazioli Fortuna
- Small lathe | Ceriani
- Small milling machine | Schaublin
- Cutting machine | Ercoletta
- Bending machine | Ercoletta
- Drill press | Serrmac
- Small drill press | Webo
- Bandsaw | Femi
- Grinder | Femi
- Extractor hood | Filcar
- Inverter welding machine | Tecnica
- TIG welding machine | Cebora
- Miter saw
- Numerically controlled milling machine

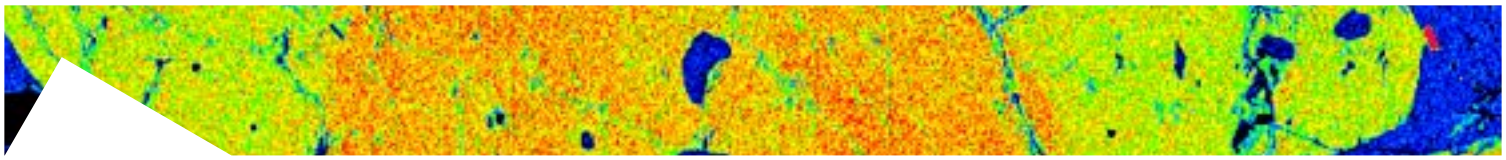

4| LABORATORY ACTIVITIES

Experimental laboratory

Quick press | Piston cylinder

The 1 inch pressure plate has been used for 29 experiments related to the following projects: shale-evaporite interaction with basalt/dolerite; latite experiments and mineral growth. The 3/4 inch pressure plate has been used for 21 experiments.

Slow to HIgh Velocity Apparatus (SHIVA)

The ninth year of activity of SHIVA has been mainly dedicated to:

1. the investigation of fluid – rock interaction in affecting frictional properties of bare rocks and gouges.
2. The study of natural and experimental smectite group clay minerals to understand the mechanical behavior and the deformation processes pertaining to subduction zone fault cores at shallow depth (<1 km) and of large landslides decollements (e.g., Vajont, 1963).

To this end we investigated the properties of fault materials retrieved from IODP (expedition 362 – Sumatra) and WFSD project in the eastern margin of the Tibetan Plateau. We set the basis for a collaboration with the Geophysical Borehole Research center at Koyna (India) to study triggered seismicity by lake impoundment in one of the best instrumented natural laboratory installed worldwide. We studied the effect of fluid chemistry (injecting CO_2-H_2O mixtures) and fluid viscosity (using mixtures of glycerol and water) in fault reactivation for both natural and induced seismicity in cohesive westerly granite, calcite and basalts. We studied the effect of fluid diffusion through pre-existing fractures and we developed models to understand the mechanical and chemical effect of fluid diffusion on faults strength to test the hypothesis of dynamic weakening by thermal pressurization and/or electrodynamic lubrication.

We developed a new system to surpass a challenging technical problem of gouge confinement with pressurized fluids. For the same purpose we bought two ISCO pumps to achieve a better control the fluid flow, volume and pressure. We studied the capability of fault in storing and releasing elastic energy through dissipative versus elastic processes using a new technique of increasing gradually the load (a novel technique for rotary shear devices). We installed a novel device to monitor changes in fault physical properties (Vp, Vs, attenuation, Young modulus) during the seismic cycle. This novel technique is providing exiting scientific results for the next year. Some of the experiments were performed in collaboration with the Royal Hollow University in London (Dr. Paola Vannucchi) with the China Academy

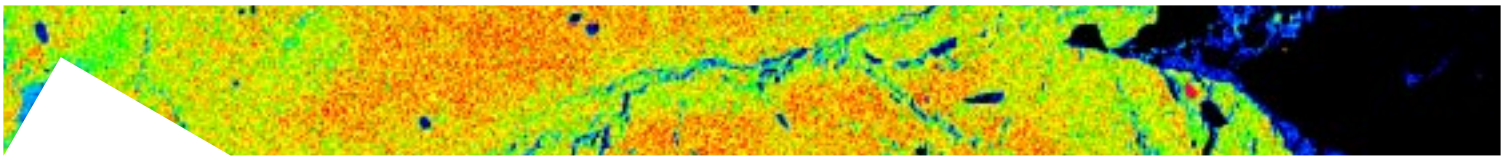

of Sciences (Prof. Haibing Li), with EPFL (Dr. Marie Violay, Dr. Francois Passelegue and PhD Chiara Cornelio), University of Texas at Austin (Dr. Nicola Tisato), Utrecht University (Dr. Oliver Plumper), Dunham University (Dr. Stefan Nielsen). To this end we run 161 experiments during 2018.

BRAVA

During the 2018 we performed about 70 experiments testing most of the capabilities of the apparatus. The experimental work has been focused on consolidating the research lines developed in the past years. In the following we summarize the main research themes:

1) Fault slip behaviour during fluid pressure stimulation in calcite and shales.

2) Fault stability of carbonate-clay mixture, within the ENI Fault stability project.

3) Comparison of laboratory permeability: Darcy's law vs. pressure oscillation technique.

4) Characterization of slip velocity functions recorded for different lithologies during stick-slip laboratory experiments.

Finally, we have used BRAVA for teaching rock-physics at Master students of the Petrophysics course at La Sapienza University of Rome and for outreach with high-school students.

Analog laboratory

The Ash-Buster, an implemented version of the shock-tube apparatus (Jet-burster) is under development for the study of volcanic ash dispersal and settling dynamics.

Rheometer

10 rheological measurements have been conducted on natural muds suspensions from Fermo (Italy).

FaMoUS (Fast Multiparametric Setup)

Seven days of field campaign at Kilauea were carried out to study the dynamics of passive and low- explosivity degassing on the surface of the Halema'uma'u lava lake from multiscale imaging.

An operative workshop BAcIO (Broadband Acquisition and Imaging Operation) was carried out at Stromboli in the framework of the COV10-Naples conference. Twenty-four participants attended the workshop that was aimed at improving the use of field-based techniques for monitoring/observing persistent explosive volcanic activity.

Six days of field campaign at Volcan de Pacaya were carried out to study the dynamics of continuous spattering activity using high-speed imaging and infrasound.

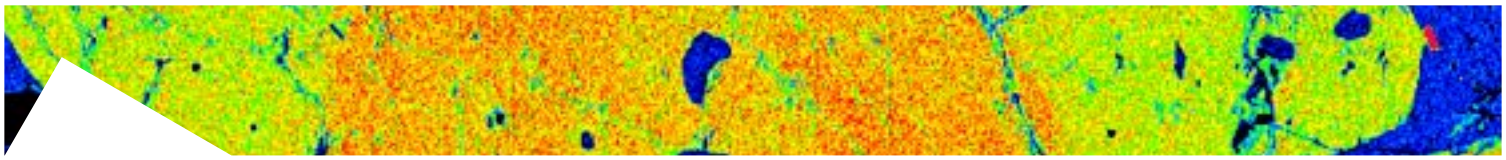

Microanalytical laboratory

FE-SEM and EMP performed 192 days of analysis in the frame of the following 22 research proposals.

Proposals

1. Lab-study on the frictional properties of basalts interacting with H_2O- and CO_2- rich fluids and implications for CO_2 storage
   P. Giacomel I Sapienza Università di Roma

2. Physical-chemical constraints of the magmatic feeding system of the 2014-2015 explosive eruptive activity at Mt. Etna
   P. P. Giacomoni I University of Ferrara

3. Experimental investigation of mechanisms generating phonolites in the Dunedin Volcano, New Zealand
   A. Pontesilli I University of Otago (New Zealand)

4 Inclusions of the Monte Amiata volcanic rocks
   G. Della Ventura I University of Roma Tre

5. Brains2South
   M. A. Di Vito I INGV OV

6. Analysis of Pre- and post-Experimental Clays and Rocks (APECAR) storage
   S. Aretusini I INGV Roma 1

7. Crystal-chemistry and texture of a 2015 Mt. Etna bomb storage
   G. Iezzi I University of Chieti

8. Textural and microchemical characterisation of Islamic pottery from Estakhr (Fars, Iran) rocks
   F. Bellatreccia I University of Roma Tre

9. The active plumbing system of La Fossa (Vulcano, Italy): clues to mafic-silicic magma interactions and the link with the magmatic-hydrothermal environment rocks
   S. Costa I University of Firenze

10. Dynamic crystallisation in magmas
    M. Nazzari I INGV Roma 1

11. Chemical and degassing dynamics of magma-sulfate ($CaSO_4$) and magma-shale interaction
    F. Deegan I University of Uppsala

12. Understanding clinopyroxene zoning as recorder of pre-eruptive magmatic processes
    T. Ubide I University of Queensland

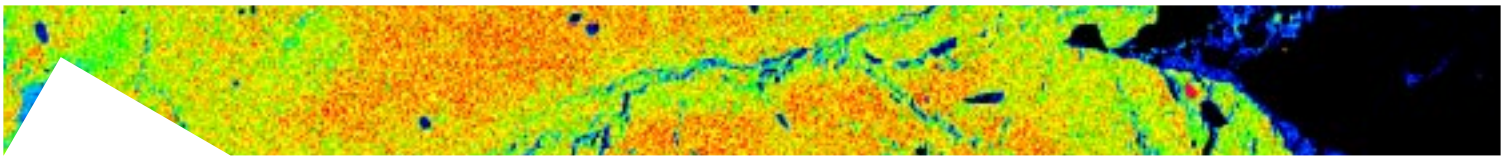

13. The origin of the K-Feldspar megacrysts hosted in the silica-rich products from Mt. Amiata (Southern Tuscany, Italy)
P. Landi I INGV PI

14. NOA (Naturally Occurring Amphibole fibres) in granitoid rocks, a case study from the Hercynian basement of Sardinia (Italy)
F. Lucci I University of Roma Tre

15. Biomonitoraggio magnetico di licheni campionati in aree esposte a incendi fraudolenti
A. Winkler I INGV Roma 2

16. Crystal-chemical variations induced by variable cooling rate in sub-alkaline silicate liquids
G. Iezzi I University of Chieti

17. Lo studio del processo di frammentazione magmatica in fusi acidi idrati
C. Romano I University of Roma Tre

18. Microstructural analyses of experimentally-derived fault rocks
C. Giorgetti I École polytechnique fédérale de Lausanne, Switzerland

19. Phase mineral equilibria at high pressure and temperature in a subducted carbonated oceanic crust with implications for the deep carbon cycle and diamond formation
V. Stagno I Sapienza University of Rome

20. Viscosity and melt structure of CO_2-bearing melts in the Earth's upper mantle: implications for the mobilization, ascent rate and emplacement of carbonatite rocks over time
V. Stagno I Sapienza University of Rome

21. Chemical and textural analyses of fault-rocks samples from the Monte Morrone Fault
V. Stagno I Sapienza University of Rome

22. High resolution tephrostratigraphy and radiocarbon chronology of the lacustrine sequence from the Fucino basin for future paleoseismological application in central Apennines (Italy)
P. Del Carlo I INGV PI

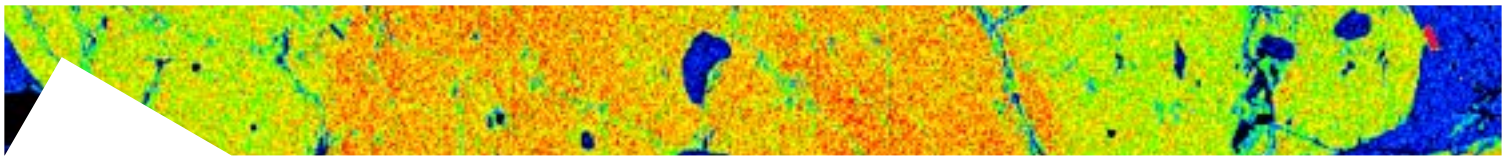

5| RESEARCH PROJECTS

1. **Sapienza Progetti di Ateneo |** Quantitative understanding of magma reservoirs feeding large-scale volcanic eruptions at Campi Flegrei **| P.I. Mollo S.**

2. **Sapienza Progetti di Ateneo |** Kinetic controls on the partitioning of chemical species between olivine, clinopyroxene and melt during solidification of terrestrial and extraterrestrial basaltic rocks: Implications for the understanding of the crystallization conditions of magmas **| P.I. Mollo S.**

3. **École polytechnique fédérale de Lausannel |** Frictional properties of Opalinus clay **| P.I. Violay M.**

4. **Marie Curie Individual Fellow FEAT (n° 656676) |** The role of Fluid pressure in EArthquake Triggering **| P.I. Scuderi M.**

5. **Sapienza Progetti di Ateneo |** The role of fluid pressure in the mechanics of slow earthquakes: insights from rock deformation experiments **| P.I. Collettini C.**

6. **ENI, contratto aperto n. 250003074 |** FAST - FAult Stability **| P.I. Tinti E.**

7. **European Research Project - ERC Consolidator Grant Project |** NOFEAR: New Outlook on seismic faults: From EARthquake nucleation to arrest **| P.I. Di Toro G.**

8. **European research project |** EPOS 'European Plate Observing System' Implementation Phase, WP 16 Multi-scale Laboratories **| P.I. Cocco M.**

9. **European Research Infrastructures Transnational Access EUROPLANET 2020 | Agreement n.:654208 (15-EPN-003) |** Approved proposal grant n. 10341: 'High-Speed Imaging Of Gas-Particle And Particle-Particle Interactions In Lab-Sized Volcanic Jets/plumes' **| P.I. Taddeucci J., Del Bello E.**

10. **MIUR Progetti Premiali 2015 |** Ash-RESILIENCE A research infrastructure for volcanic ash hazard assessment to aviation and communities living near Italian active volcanoes **| P.I. Costa A., Andronico D.**

11. **MIUR Progetto TOP-DOWN FISR 2016 Task 3 |** Magmatismo e vulcanismo dell'Italia Centrale, Attività C) Studio del sistema vulcanico dei Colli Albani (Task leader Scarlato P.) **| P.I. Galadini F.**

12. **European research project |** EUROVOLC 'European Network of Observatories and Research Infrastructures for Volcanology' **| P.I. VogFjiord K.**

13. **MIUR Progetto Ricerca Libera FISR 2016 |** Gas hazard in Central Italy: Experimental investigation on the Radon emissions from volcanic rocks **| P.I. Scarlato P.**

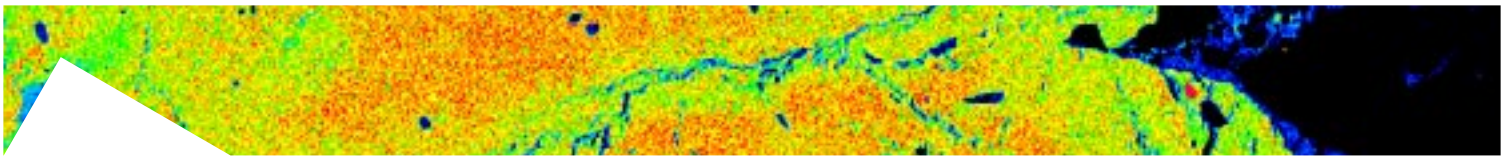

6| PARTNER LABORATORIES

1. **Planetary Environmental Facilities |** Aarhus University **| Denmark**
2. **Experimental & Physical Volcanology |** Ludwig Maximillians Universitat **| Germany**
3. **Institute of Geochemistry and Petrology |** ETH Zurich **| Switzerland**
4 **Università di Scienze Biologiche, Geologiche e Ambientali |** Università di Catania **| Italy**
5. **Dipartimento di Fisica e Scienze della Terra |** Università di Ferrara **| Italy**
6. **Petro- Volcanology Research Group (PVRG) Department of Physics and Geology |** University of Perugia **| Italy**
7. **School of Earth and Environmental Sciences |** University of Queensland **| Australia**
8. **Department of Geology |** University of Otago **| New Zealand**
9. **Dipartimento di Scienze |** Unversità di Roma Tre **| Italy**
10. **LEMR |** EPFL **| Lausanne, Switzerland**
11. **Geoscience Department |** Utrecht University **| Netherlands**
12. **Rock Mechanics Laboratory |** Durham University **| UK**
13. **Jackson School of Geosciences |** Texas University at Austin **| USA**
14. **Dipartimento di Geoscienze |** Università di Padova **| Italy**

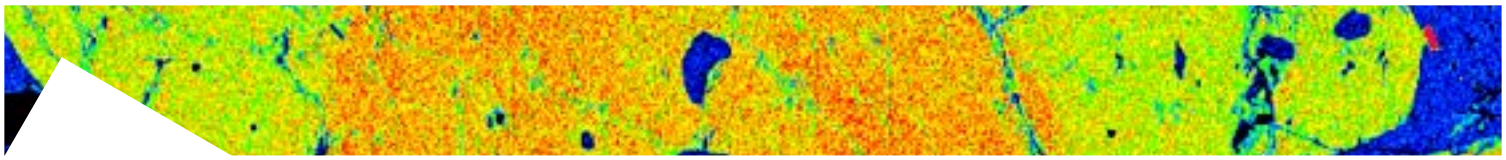

7| PARTNER INSTITUTIONS

1. Ludwig Maximillians Universitat Munchen **| Munich | Germany**
2. Royal Hollow University of London **| London |** UK
3. School of Earth and Environmental Sciences **| University of Queensland |** Australia
4. Department of Geology **| University of Otago |** New Zealand
5. Department of Geology and Geophysics, SOEST **| University of Hawaii |** USA
6. Department of Physics and Astronomy **| Aarhus University |** Denmark
7. HVO Hawaiian Volcano Observatory **| USGS | USA**

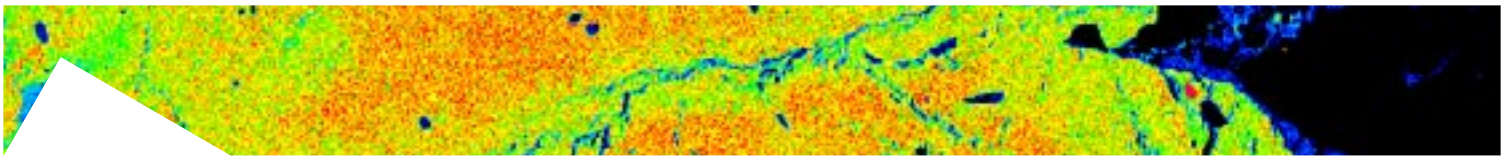

8.1 PETROLOGY, MINERALOGY, VOLCANOLOGY

The effect of decompression and water content on the degassing pattern of magmas

Kazarian A., Romano C., Scheu B., Misiti V.

The aim of the project is to investigate how the physical state of magma (anhydrous chemical composition, volatile content, bubble content and shape, as well as dP/dT conditions) can influence the degassing process of magma. Hydrous samples were synthesized at INGV Rome with the Piston Cylinder and with the Quick Press. The starting material is a dehydrated trachytic glass from the fallout deposit (member B1) of Agnano Monte Spina eruption.

Gold-Palladium and Platinum capsules of internal diameter 3 mm and 15 mm long were used. Those were filled with powder and different amount of water (between 0.5 and 2.5 wt% H_2O).We run a total of 8 synthesis experiments. The experiments were performed at 5 Kbar of pressure with the Piston Cylinder (3 kbar with the Quick Press) and 1200°C for 2 hours to allow dissolution and complete homogenization of water through the samples.

Hydrous glasses were then cut into pieces and prepared for the decompression experiments. The decompression experiments were conducted at the fragmentation lab at LMU (Munich University, Germany), using the following apparatus:

- Split-tube furnace, used for heating of the samples.
- Shock-tube apparatus, main experimental device used for the fragmentation experiments.

A total of 8 decompression experiments were performed at high temperature (850 °C). In every experiment the decompression profile was varied: i.e. in the first set of experiments the samples were decompressed to ambient pressure, in the second set of experiments the samples were decompressed to a P>Patm (oversaturated) and then quenched isobarically; finally, in the third set of experiments the samples were decompressed to ambient pressure in a stepwise fashion. Decompression rate was around 1 MPa/s for each experiment.

Decompressed samples were quenched at constant pressure and then recovered. For textural analysis BSE images were taken at INGV-Rome with Jeol JSM-6500F thermal Field SEM. Different degassing patterns were observed for each

sample, as well as different vesicle number densities and distribution, as a result of the varied decompression types and timescales. Indeed, a direct correlation between total decompression, water content and final porosity and BND is observed.

The results allow to preliminarily confirm the validity of a BND decompression rate-meter for trachytic melt, though providing further data with upcoming projects will help to give a more precise parameterization.

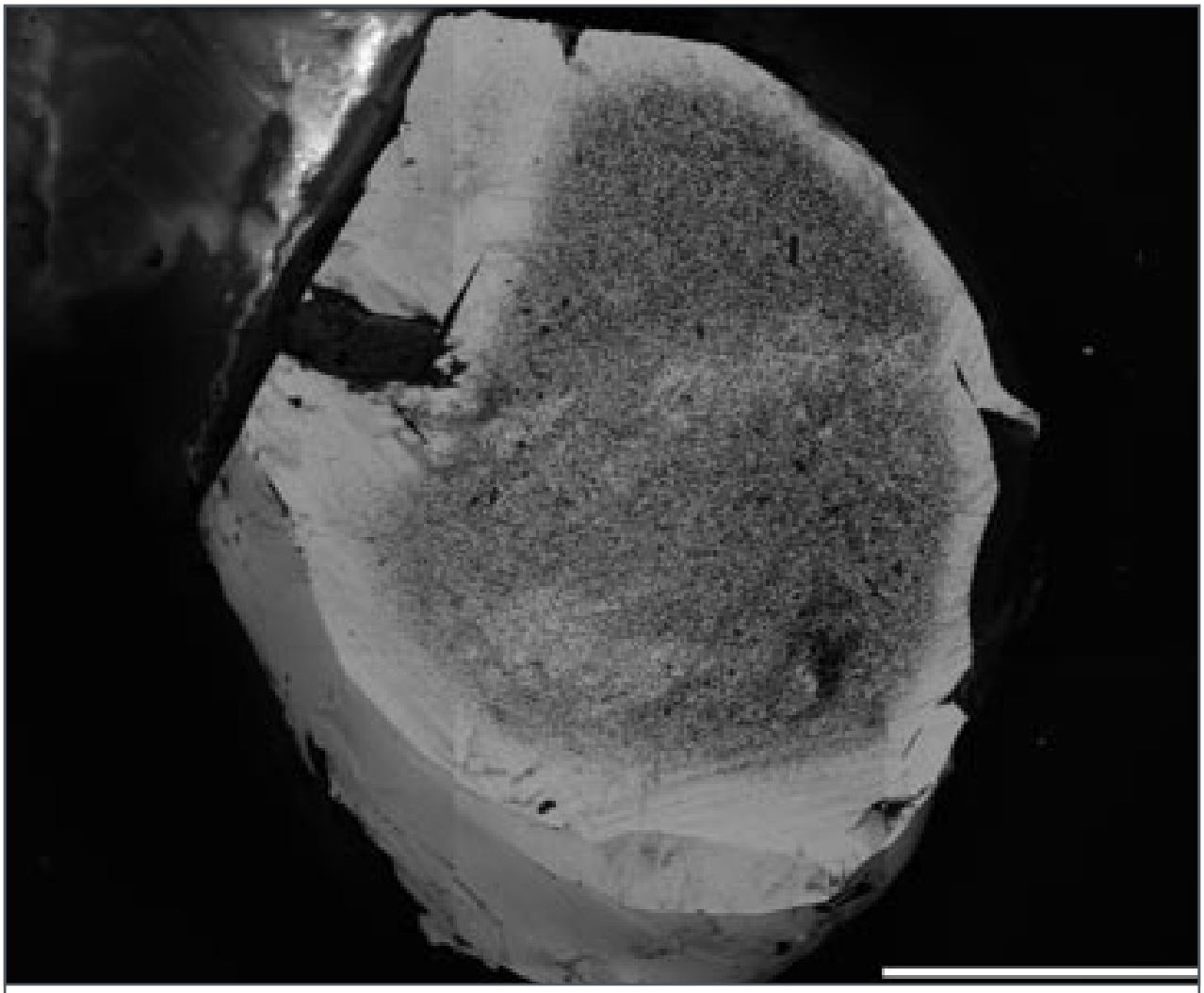

Fig. 1 I BSE image of a sample cut (AMS 1.7-4). The sample underwent a single drop of pressure and was quenched at over-saturated conditions after a long annealing time.

Magma dynamics at La Fossa cone (Vulcano Island, Italy): evidences from eruptive products and temperature gradient experiments

Costa S., Masotta M., Gioncada A., Pistolesi M., Scarlato P.

The eruptive sequence of Palizzi is a complex volcanic succession emplaced at La Fossa volcano (Vulcano, Aeolian islands) during the 13th century. The erupted products range in composition from latite to rhyolite, with a wide range of K_2O content in the trachytic field. Pumice clasts collected from the main trachytic sub-Plinian fallout exhibit the highest K_2O concentration among the eruptive products of Vulcano island, remarkably higher than any trachytic magmas with similar silica content erupted at La Fossa. In order to investigate the magmatic processes that produced this composition, we have experimentally simulated crystallization and differentiation in presence of a temperature

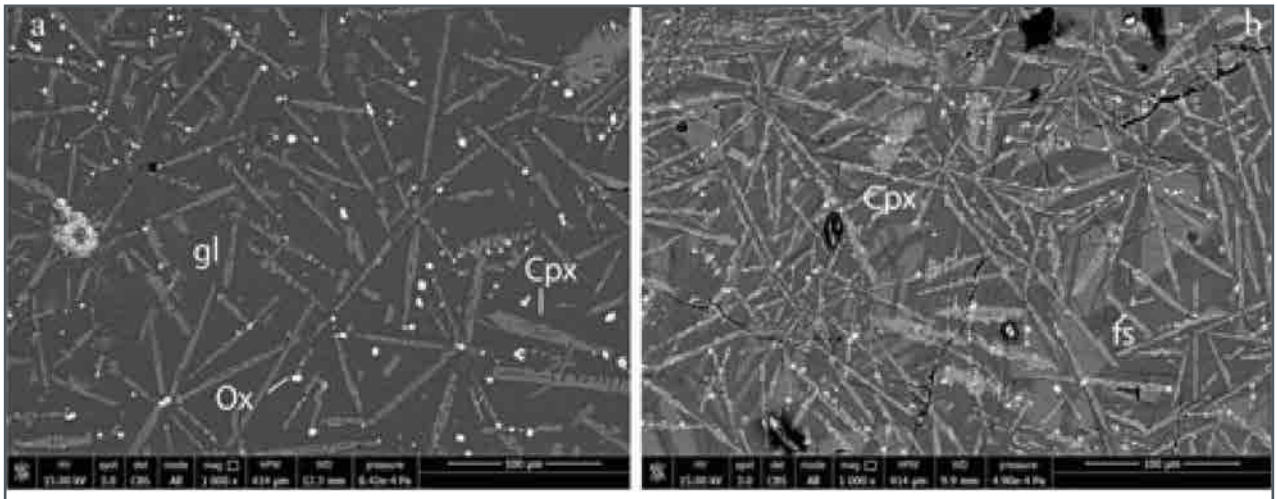

Fig. 1 I Backscattered electron (BSE) images of experimental products in the temperature range 1000-975 °C showing different phase assemblage and melt-glass proportions; 2 wt.%H_2O content (a) and anhydrous (b).

gradient, using a latitic starting composition (enclave of the 1739 AD Pietre Cotte lava flow). Experiments were performed at pressure of 150 MPa and temperature of 1050-900 °C (hot and cold zone, respectively), at both hydrous (H_2O=2wt.%) and anhydrous conditions, to reproduce a compositionally and thermally zoned shallow magma reservoir. Mineral phases include clinopyroxene (first liquidus phase), oxides, alkali feldspar (more abundant at anhydrous condition) and biotite (at hydrous condition only). At anhydrous conditions, glass composition along the crystallization gradient enriches in alkali (Na_2O+K_2O ranging from 10.7 to 11.7 wt.%) with a nearly constant SiO_2 (59±0.5 wt.%),

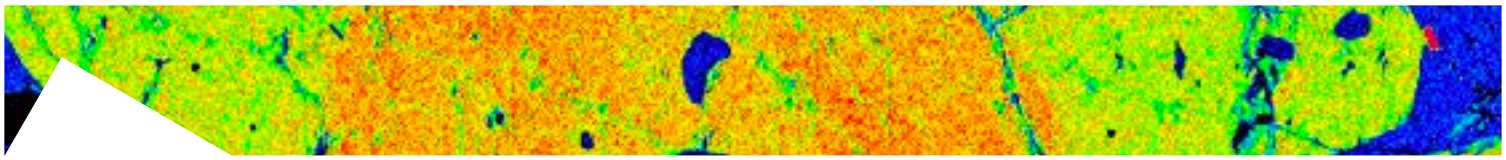

heading towards the matrix glass compositions of the trachytic natural pumice. In contrast, at hydrous conditions, the SiO_2 content increases from 58.5 to 62.2 wt.%, with an initial increase in alkali composition (Na_2O+K_2O ranging from 10.2 to10.9wt.%) before stabilizing at a constant value of ~11.2 wt.%, approaching the trachytic differentiation trend shown by La Fossa products. Experimental results suggest that the H_2O content in the melt exerts a primary control on phase stability in the pressure range of La Fossa magmas, thus determining the differentiation trends of the erupted magmas.

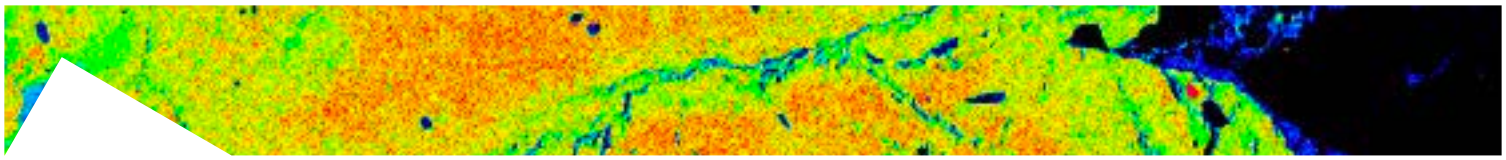

Chemical and degassing dynamics of magma-sediment interaction at Large Igneous Provinces (LIPs)

Deegan F.M., Troll V.R., Geiger H., Misiti V., Freda C., Bedard J.

The Franklin, High Arctic and Siberian Large Igneous Provinces (LIPs) all comprise networks of dykes and sills that intruded volatile-rich sedimentary rocks, including sulphur-bearing shales and evaporites. These settings thus offer enormous potential to learn how volatile-rich sedimentary rocks respond to magmatic heating events during LIP emplacement. Indeed, there is growing evidence that emplacement of large igneous provinces (LIPs) is linked to catastrophic climate change and mass extinctions. A fundamental control on the severity of the environmental impact of LIPs, in turn, seems to be the type of sedimentary rock that was intruded. Volatile-rich sediments including limestones, shales, sandstones, and sulphate evaporites have the potential to de-gas in contact with magma, liberating greenhouse and toxic gases such as CO_2, CH_4, SO_2, and halocarbons. Our objective is to define the processes and time-scales of magma-sediment interaction and associated volatile release by utilising high-pressure high-temperature (HPHT) experimental petrology to simulate magma-sediment processes at upper crustal conditions.

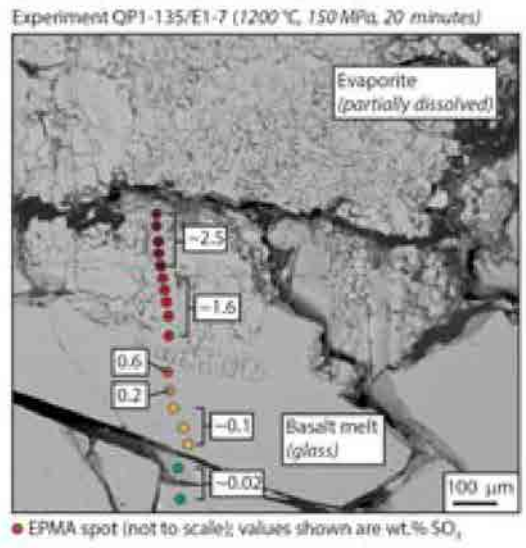

Fig. 1 | Magma-sulphate (evaporite) experiment utilising starting materials from the Franklin LIP, Northern Canada. The experiment conditions were T = 1200 °C, P = 150 MPa and t = 20 minutes. The glass (former melt) at the contact between evaporite and basalt was analysed by electron microprobe for its SO_3 content. A clear diffusive gradient can be seen whereby the glass closest to the evaporite contains around 2.5 wt.% SO_3 on average, which steadily declines to ca. 0.02 wt.% SO_3 in the glass distal to the evaporite. The size of the EPMA spots in the figure are exaggerated slightly for visibility.

We performed eleven successful experiments in 2018 and we expect that further analysis of our experiments will generate insights into i) large-scale crustal degassing during emplacement of LIPs with implications for paleo-climate changes and ii) processes during magma-sediment interaction that can lead to economic concentrations of sulphides as a consequence of $CaSO_4$ recycling.Our experiments have already begun to document, e.g., assimilation of sulphate and concurrent sulphur dif-

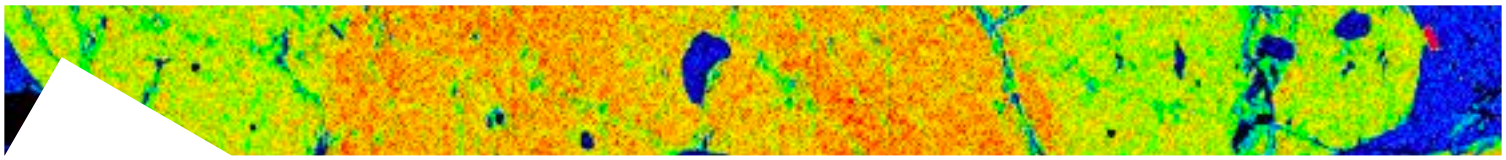

fusion into the surrounding basaltic melt (Figure 1). Further magma-sediment experiments were carried out in early 2019 and will be analysed for their chemistry by electron microprobe later this year.

Experimental simulations of volcanic ash resuspension by wind under the effects of atmospheric humidity: comparing bulk vs sieved samples

Del Bello E., Taddeucci J., Merrison J.P., Alois S., Iversen J.J., Scarlato P.

The joint INGV Roma - Aarhus University (DK) research collaboration, started in 2016 in the framework of the EU-funded Europlanet TNA call, is still ongoing, aiming at the accurate modelling of the threshold friction velocity of the volcanic particles (*Uth**), which is the key parameter controlling volcanic ash detachment by wind and its subsequent resuspension into the atmosphere. In 2018, the environmental wind tunnel experiments provided new experimental data on particle resuspension of natural volcanic ash from Campi Flegrei (Italy) and Eyjafjallajökull (Iceland), Sakurajima (Japan). For each of these samples, the detachment threshold of the bulk sample was systematically parameterised as a function of atmospheric relative humidity, from <10% to >90% (and related ash moisture content). Furthermore, in the first two cases, the detachment behaviour of the bulk sample was compared against that of the same sample, sieved into the 0-63, 63-125, and 125-250 classes µm.

In the case of the Campi Flegrei bulk ash, the trend of remobilization for increasing *Uth** is similar to the trend of remobilization showed by the same sample

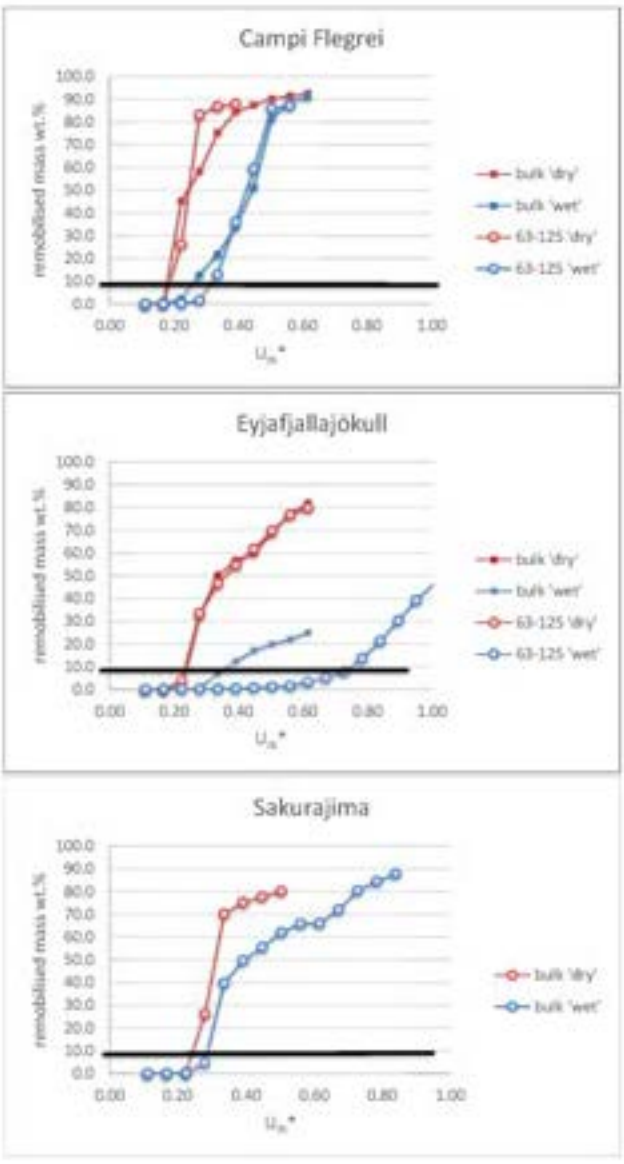

Fig. 1 | Percentage of remobilised ash as a function of the wind tunnel friction velocity. From top to bottom, results for Campi Flegrei-Pomici Principali, Eyjafjallajokull, and Sakurajima samples, in dry (red) and wet (blue) conditions, respectively. The threshold friction velocity value u_{th}* is set when the remobilised mass reaches 10% (balck line). uth* depends on the sample grain size distribution, density and particle shape, and moisture.

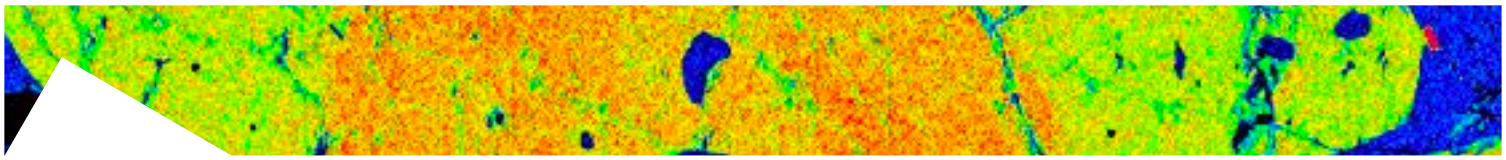

sieved in the intermediate (63-125 µm) grain size class. This matching behaviour occurs both in dry and in wet conditions, with particles reaching the 'threshold' remobilised mass (10% wt.) at *Uth** values of ca. 0.18 and 0.3 m/s for the dry and wet case, respectively. Using the Eyjafjallajökull bulk ash the trend is observed to match that of intermediate sieved particles only in dry conditions, In this case, the 'threshold' remobilised mass corresponds to *Uth** values of 0.2 m/s, irrespective of particle grain size distribution. In wet conditions, the bulk and the sieved samples display a different behaviour, with the former reaching the 10% wt. threshold condition at significantly lower *Uth** (0.34) values than the latter (0.76).

Reasonable agreement with force balance resuspension models was seen, which implied an increase in interparticle adhesion force of up to a factor of six due to high humidity. Our results imply that, contrary to dry conditions, one single modelling scheme may not satisfy the resuspension of volcanic ash from different eruptions under wet conditions.

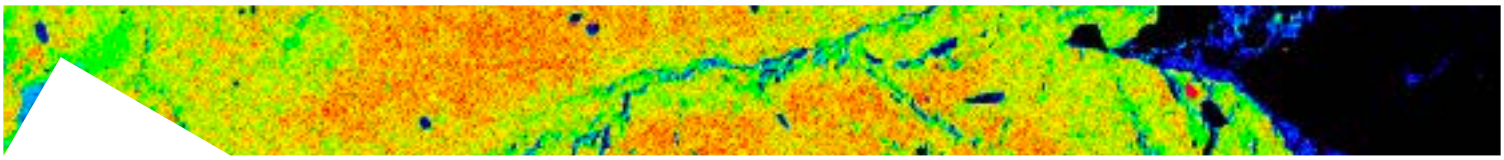

Sedimentation of particles from volcanic ash plumes: a new laboratory equipment

Del Bello E., Taddeucci J., Scarlato P., Pennacchia F.

The quantification of volcanic hazard in relation to the generation, dispersion and sedimentation of volcanic ash, requires the capability to model ash temporal and spatial evolution in an appropriate and rapid manner. It is of fundamental importance, for the construction of such models, to integrate the knowledge of the physical parameters of the eruptions not only with field data on distribution and volume of tephra, but also with realistic experimental observations of the phenomena that influence the dispersion of ash, like aggregation, and the mass fall rate of particles. With this target, in 2018 we started to design and build an ejection/sedimentation tube dedicated to experimental volcanology, particularly for the study of sedimentation behaviour and fall velocity of ash particles in atmospheric conditions.

The INGV-Rome group has already developed experimental models able to describe the effects of aggregation of fine ash and of the mass drop of particles, driven by the need to define the parameters to be included in the dispersion models. These experiments have successfully enabled the quantification of basic parameters and the observation of the phenomena, but did not systematically investigate the effects of particle shape on settling conditions and plume shape. The project involves the construction of a particle ejection/settling system, the Ash-Burster, where it is possible to control the flow, and volume of the pressurised air, so that it is suitable for the simulation of processes into a still atmosphere ranging from upward particle injection to gravitational sedimentation. The Ash-Burster is designed to allow the study of particle aerodynamics in a large spatial domain; therefore the test section is 5 m in height with an areal section of 1.5 x 1.5 m.

The infrastructure is expected to be equipped with basic instrumentation, some already existing in the lab, such as high-speed and high-definition cameras, and laser lighting systems, and sensors dedicated to specific types of experiments: accelerometers, pressure transducers, anemometers, turbulence generators, visualization and lighting systems, LDA (Laser Doppler Anemometry).

Through the acquisition of images combined by multiple cameras and the processing of these with particle image ve-

Fig. 1 I Schematic representation of the Ash-Burster, designed to study volcanic particle aerodynamics in a large spatial domain.

locimetry and tracking techniques it will be possible to reconstruct the observed dynamics in 3D. The modular conception of the apparatus is also envisaged so that subsequent implementations are possible.

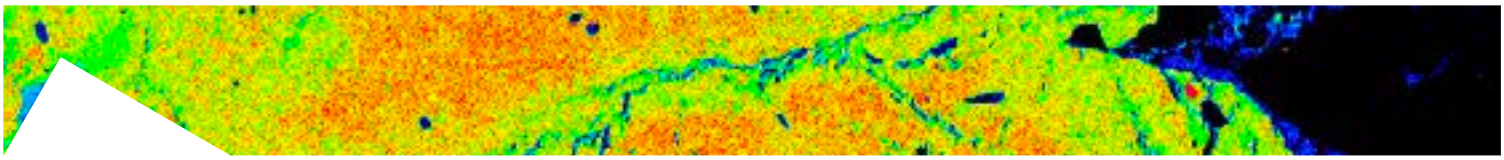

Comparing natural and synthetic infrasonic signals of strombolian explosions: insights into slug-plug conduit processes

Capponi A., Del Bello E., Taddeucci J., Scarlato P.

The interpretation of geophysical measurements at active volcanoes is fundamental for understanding the mechanisms behind explosive volcanic eruptions. For Strombolian activity, the ascent, expansion and burst of gas slugs within a low-viscosity magma column have often been considered the main source mechanisms for infrasonic signals, providing a relatively straightforward relationships between geophysical signals and conduit flow processes. However, recent field observations and experimental studies have indicated the importance of rheological stratification within the conduit in controlling flow processes and modulating the associated geophysical signals. Using scaled analogue laboratory experiments for slug ascending and bursting through a rheologically-stratified conduit, we investigated how the presence of a viscous layer affects pressure changes at burst, producing experimental infrasonic signals to compare with infrasonic waveforms acquired from different vents at Stromboli. By considering the presence

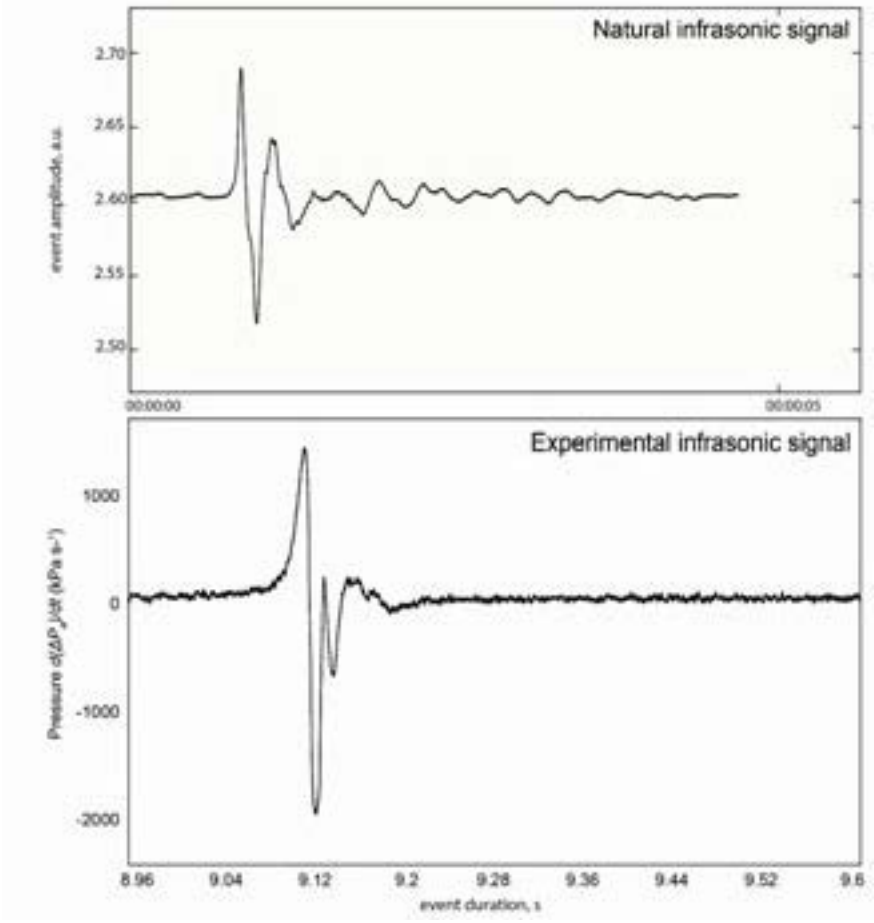

Fig. 1 I Comparison between a natural infrasonic signals from Stromboli (top panel) and an experimental infrasonic signal (expressed as the time derivative d(ΔPa)/dt of pressure variations DPa within the experimental tube, for a reduced experimental ambient pressure of 1 kPa) for an experimental slug (initial injection volume of 24 ml) ascending through low-viscosity liquid overlain by a higher viscosity plug.

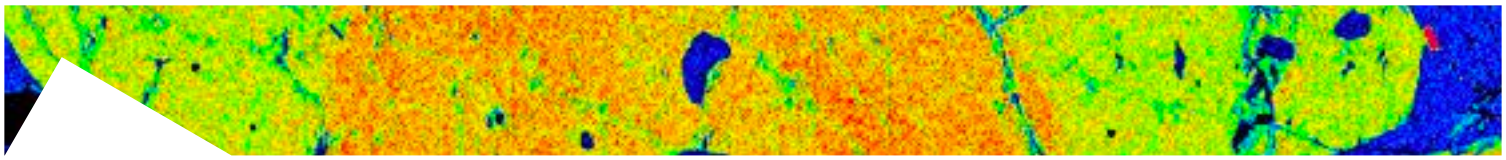

of a viscous layer atop the magma column, the direct relationships between slug ascent within a singles low-viscosity magma and the resulting infrasonic signals breaks down. The similarity between experimental and measured waveforms at Stromboli demonstrate how infrasonic signals can be interpreted in terms of gas slugs expanding and bursting through a viscous layer. This suggests that – for a more accurate interpretation of infrasonic signals – we need a better characterization of magma rheology in the shallower part of the conduit and deeper understanding of flow processes.

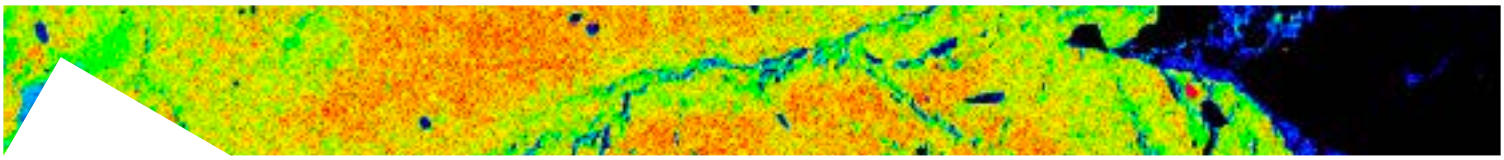

Point defect equilibria in hydrous forsterite synthesized up to 4 GPa

Del Vecchio A., Poe B.T., Misiti V., Cestelli Guidi M.

Water distribution in the deep Earth represents one of the most important topics in the field of geodynamics due to its large impact on the physical and chemical properties of the Earth's mantle, such as electrical conductivity, seismic anisotropy, diffusion and rheology. In this study we synthesized hydrous forsterite at 1100 C° and up to 4 GPa with either a piston cylinder or multianvil apparatus. As a starting material, we used synthetic forsterite, unbuffered by SiO_2, obtained by thermo-mechanical activation of talc and magnesium carbonate hydroxide. Hydration was carried out using liquid H_2O as hydrogen source. Samples were polycrystalline in an effort to distribute H_2O throughout the sample both rapidly and homogeneously.

FTIR micro-imaging and point-by-point analyses allowed us to observe the spatial distribution of H_2O in each sample. Using the Paterson calibration, we observed total water content concentrations ranging between 100 and 700 ppm wt H_2O. Multiple absorption bands are found in the frequency range between 3400 and 3700 cm^{-1}, identifying at least 9 peaks in all samples. The major bands are located at 3566, 3578 and 3612 cm^{-1}, while minor bands are centered at 3476, 3536, 3550, 3605, 3693 and 3698 cm^{-1}, in good agreement with experimental studies conducted on both hydrous forsterite and single crystals of olivine. The stronger OH stretching peaks can be attributable to vibrational modes associated with the hydrogarnet defect 4HSix in which four protons occupy a vacant tetrahedral site. None of the OH bands observed are found at frequencies associated with hydrogen occupying vacant octahedral sites. Differences in the total H_2O concentrations of our samples allow us to distinguish the different chemical species responsible for peaks observed in the OH stretching region. As water fugacity increases, it is likely that vibrational modes of minor H-bearing chemical species other than $4HSi^x$ become increasingly more important. The dissociation reaction of the hydrogarnet species to form the associate defect $3HSi' + Hi^{\bullet}$, for example could explain the presence and growth of the band at 3476 cm^{-1} as forsterite becomes richer in H_2O.

Textures and phase composition in a 2015 Etnean bomb: reconstructing its solidification history

Giuliani L., Casetta F., Lanzafame G., Nazzari M., Iezzi G., Ferlito C., Coltorti M., Scarlato P.

A 15 x 10 cm rugby-ball like bomb erupted in 2015 at Mount Etna has been cut, polished and imaged with a high-resolution scanner (HRS), to investigate the largest elliptical and smallest circular sections (Fig. 1). They show about 1/3 area% of bubble-rich portions with rounded- to rolling-like 2D shapes immersed in bubble-poor/free areas. Two thin sections have been extracted coaxially to these mesoscopic planes, such to contain either bubble-free and -rich patches. The thin sections have been also imaged by HRS and then analyzed by BS-SEM and EPMA-WDS (Fig. 1) at the HPHT-INGV lab. The textural features investigated by SEM have been acquired by sequential micro-photographs

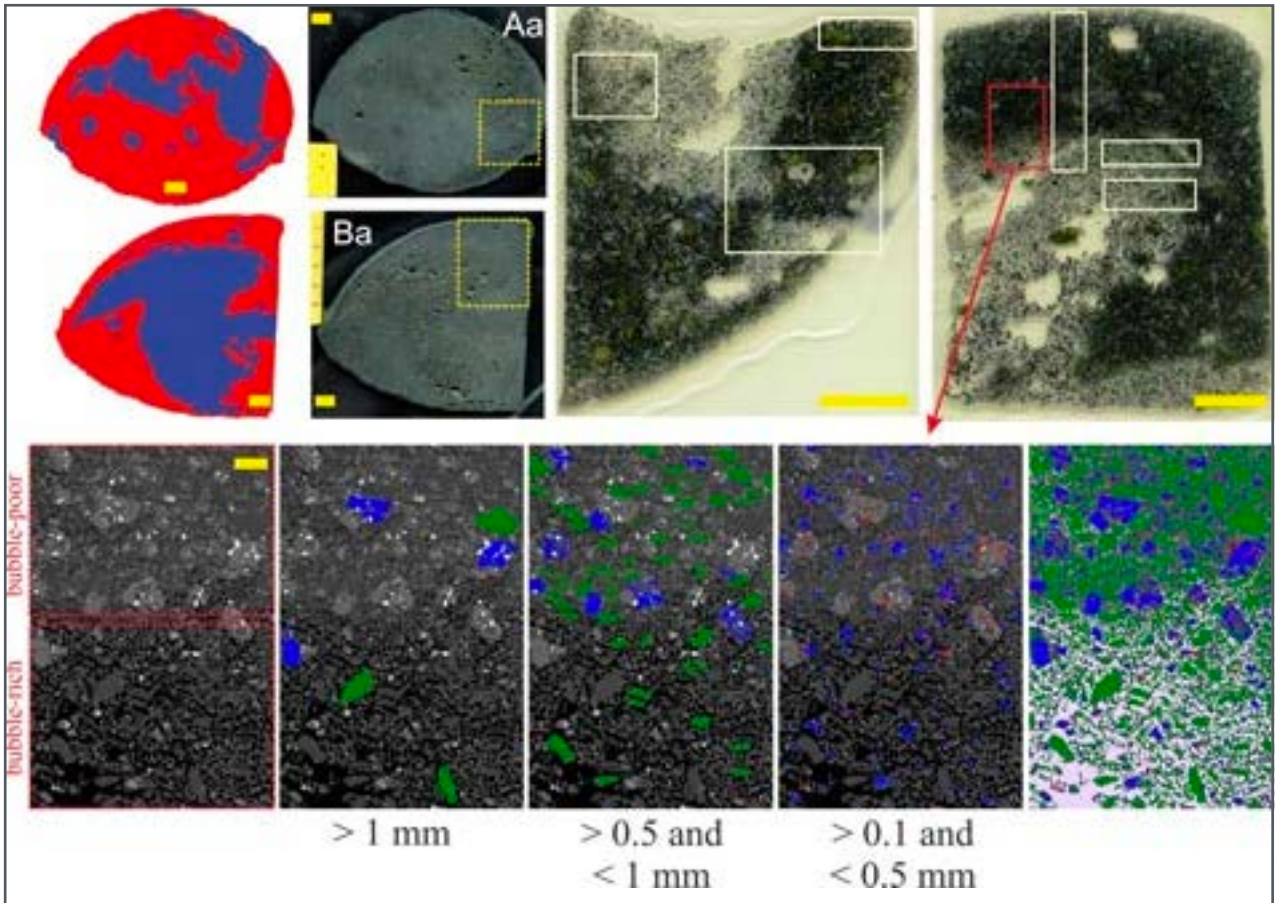

Fig. 1 I Polished-HRS images of mesoscopic sample and thin sections of the bomb from Mt. Etna. The mesoscopic sample has been cut both in the transversal (Aa) and longitudinal (Ba) sense. Yellow and white box indicate the areas of thin sections and BS-SEM puzzles, respectively; yellow bars are 1 cm. The false color blue and red on the mesoscopic sample individuate bubble-rich and bubble-poor patches, respectively. Plagioclases (green), clinopyroxenes (blue) and spinel (red) have been classified as a function of their 2D lengths.

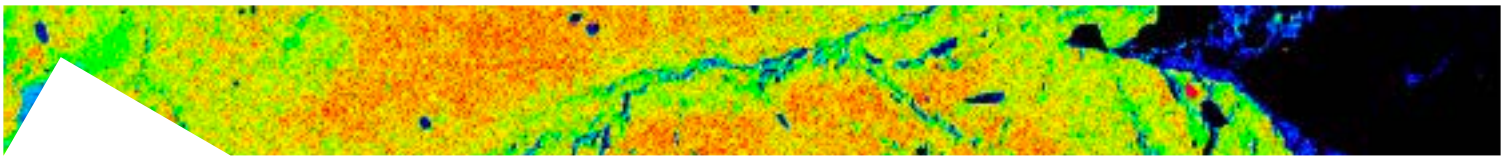

to image surfaces with size of tens of mm^2. They allowed to measure the size of either large and tiny phases, such bubbles, plagioclase (plg), clinopyroxene (cpx), spinel (sp) and olivine (ol) (Fig. 1).

On the whole, vesicle-rich patches are enriched in plg and slightly depleted in cpx, while vesicle-poor/free portions display the opposite features. The number per area of cpx and sp with 2D size between 0.5 – 1 mm and > 1 mm are both higher in bubble-poor patches than in bubble-rich ones. In parallel, the CSDs of cpx and sp display a similar trend. Thereby, 2D largest cpx and sp are more abundant in bubble-poor zones with respect to bubble-rich areas.

The compositions of plg and cpx cores measured by EPMA on bubble-rich and -poor patches overlap, whereas those of sp and ol are different. The olivine in bubble-poor zones are richer in Fe and depleted in Mg, whereas those in bubble-rich patches are more magnesian. The sp in poorly vesiculated patches are enriched in Ti and depleted in Fe with respect to those in vesicle-rich areas.

The shape and distribution of bubble-rich and -poor patches indicate that the bomb was poorly viscous just before or immediately after emission. The two different patches could result from a sort of self-mingling between bubble-rich and bubble-poor portions. The former can correspond to magma close to conduit walls, where strain rates is high, the latter to magma far away from conduit walls (Fig. 1). This reappraisal hints that magma ascent in conduit was not laminar.

The similarity in composition of plg and cpx cores indicate that their crystallization occurred prior to localized degassing (bubble-rich patches), whereas the bimodal composition of sp and ol suggest a growth (at least partially) occurred after degassing. The different area% of plg and cpx in bubble-rich and -poor/free patches suggest that their outer portions grew during magma ascent in conduit, in response to localized degassing conditions driven by different amounts of strain. These latter were probably high in proximity of the conduit walls, whereas moderate to absent in its central portions.

Crystal-chemical evolution of sp, px and plg crystallizing from a MORB as a function of cooling rate

Giuliani L., Iezzi G., Vetere F., Nazzari M., Cavallo A., Mollo S., Misiti V., Ventura G., Beherens H., Scarlato P.

Spinel (sp), clinopyroxene (cpx) and plagioclase (plg) are the main crystalline phases growing during the solidification of basaltic melts. However, the dependence of their crystal-chemical attributes on kinetic effects is still puzzling. Thereby, a MORB melt are cooled from 1300 ($T_{superliquidus}$) to 800 °C (T_{quench}) at 9000, 1800, 180, 60, 7 and 1 °C/h, under P_{atm} and air fO_2. The run products are analysed by FE-SEM-EDS and EMPA-WDS to characterize their chemical compositions. Sp and cpx nucleate invariably from 1 to 9000 °C/h, while plg grows only for cooling rates (ΔT/Δt) from 60

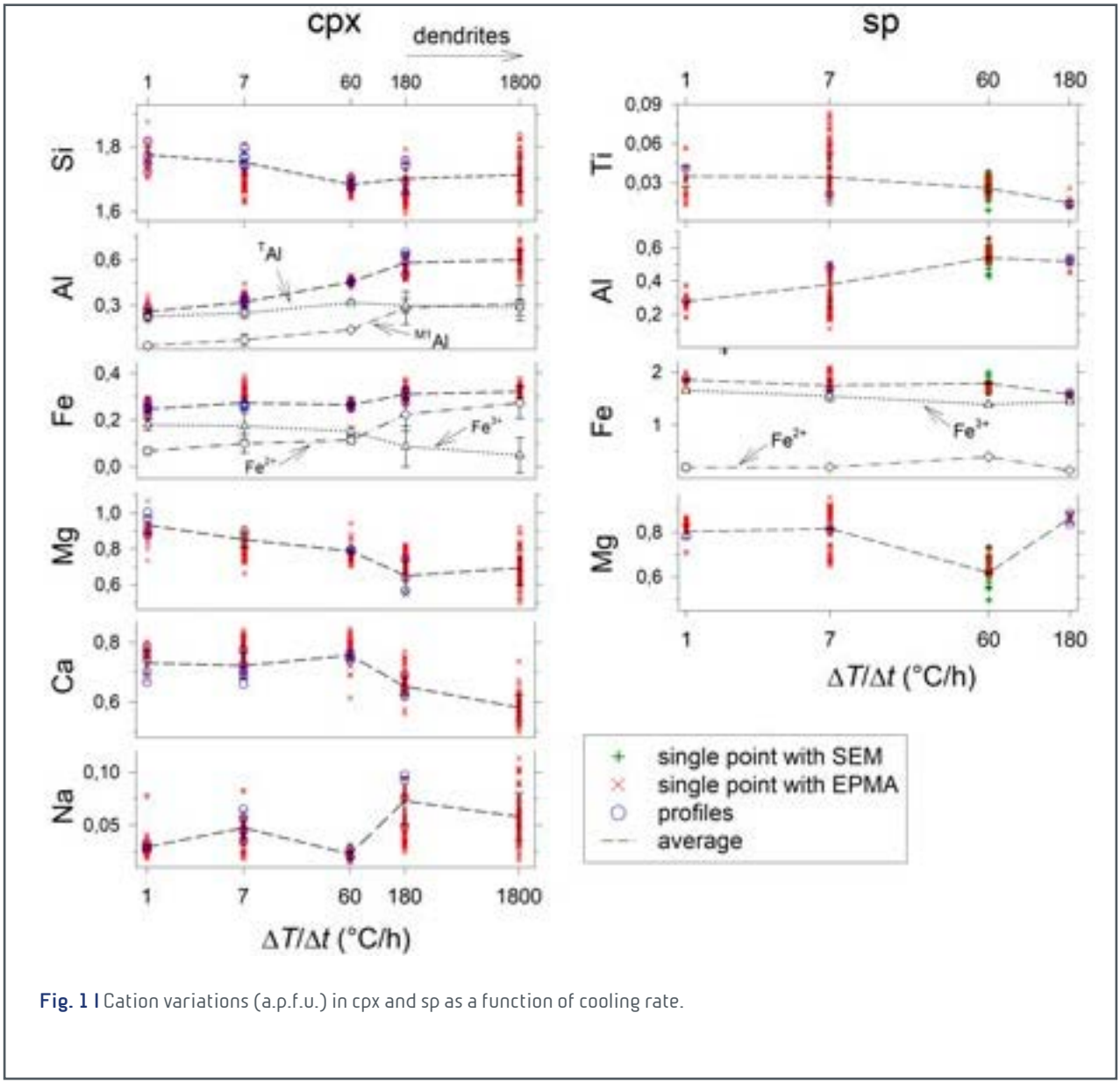

Fig. 1 I Cation variations (a.p.f.u.) in cpx and sp as a function of cooling rate.

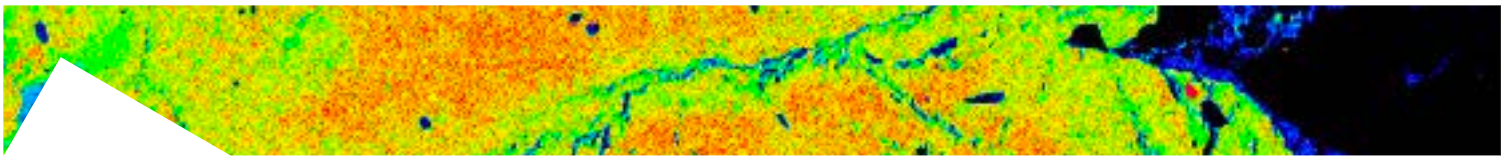

to 180 °C/h. As ΔT/Δt increases, sp is depleted in TiO_2 and significantly enriched in Al_2O_3; cpx also incorporates significant amounts of Al_2O_3. Plg displays a slight decrement in Al_2O_3 and minor increments of Fe_2O_3 and MgO. As the kinetics increases, the chemical compositions of all crystalline phases tend to approach that of the starting liquid. All the chemical trends change between 60/180 °C/h, when plg does not nucleate and dendritic shapes occur. According to charge balance and general crystallochemical constraints, at fast ΔT/Δt Al in cpx increases, whereas Mg, Fe and Ca decrease. Also, sp becomes progressively enriched in Al, at the expense of the sluggish diffusion of Ti in the melt phase (Fig. 1). In the holocrystalline run products, Si, Al, Ca and Na in plg remain almost constant. Therefore, cpx and sp solidifying from an almost degassed MORB are strongly affected by kinetic effects. Al results to be a key element to track the kinetics conditions and calibrate efficient geospeedometers, either using cpx and sp. Effects of cooling rates on crystal-chemistry of cpx and sp can be also valuable to obtain synthetic materials with desired chemical and textural characteristics.

Textural evolution of crystals from a MORB liquid cooled at variable rates

Giuliani L., Iezzi G., Vetere F., Nazzari M., Cauti F., Mollo S., Misiti V., Ventura G., Cavallo A., Behrens H., Scarlato P.

To analyze the effect of cooling kinetics on the crystal texture, a MORB liquid from Iceland is cooled from 1300 °C ($T_{superliquidus}$) to 800 °C (T_{quench}) withcooling rates ($\Delta T/\Delta t$) of 1, 7, 60, 180, 1800 and 9000 °C/h. Each experiment has been conducted at P_{atm} and fO_2 of air; the runs at 180 and 1800 °C/h have been duplicated. The possible "superheat-

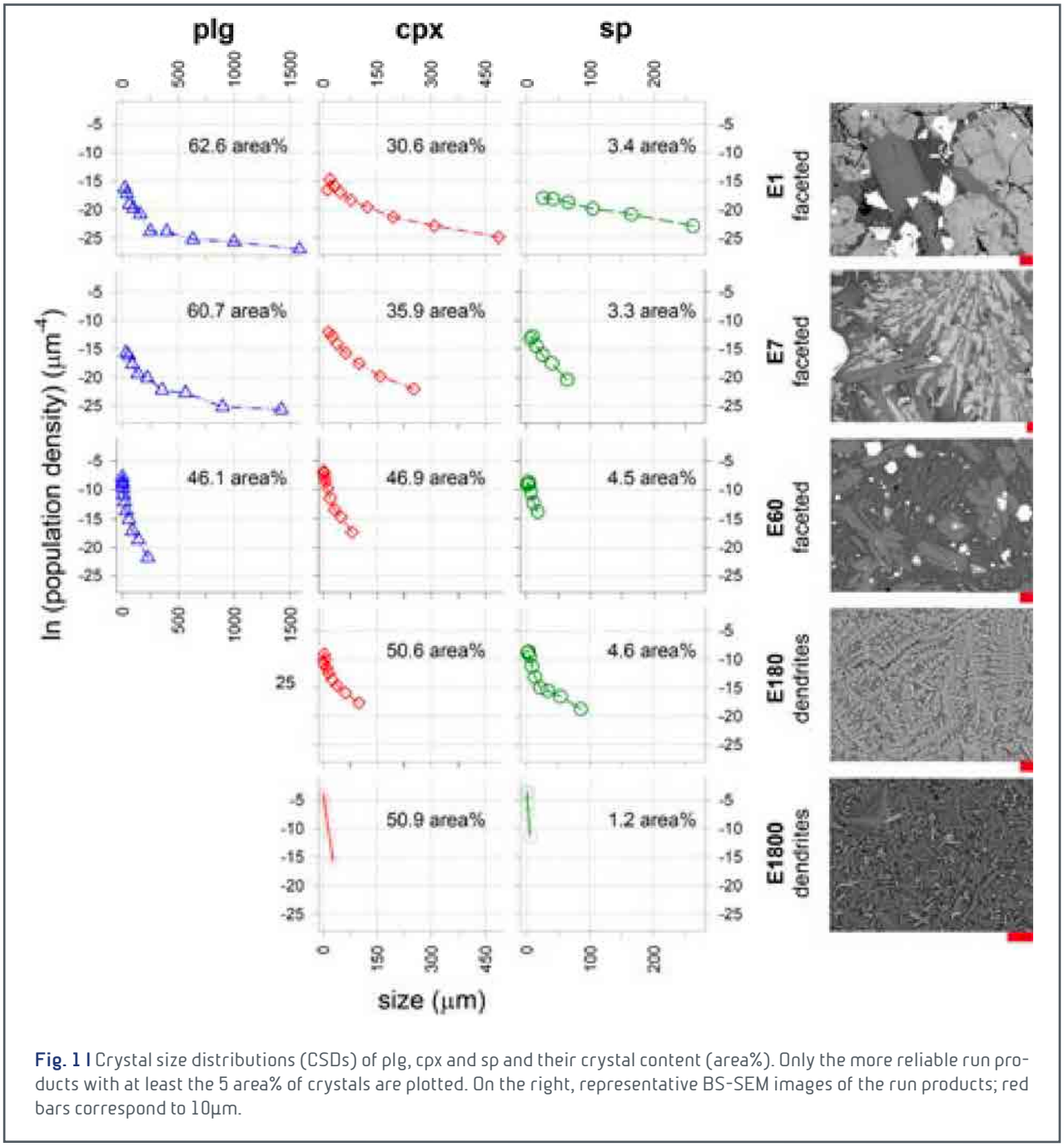

Fig. 1 I Crystal size distributions (CSDs) of plg, cpx and sp and their crystal content (area%). Only the more reliable run products with at least the 5 area% of crystals are plotted. On the right, representative BS-SEM images of the run products; red bars correspond to 10μm.

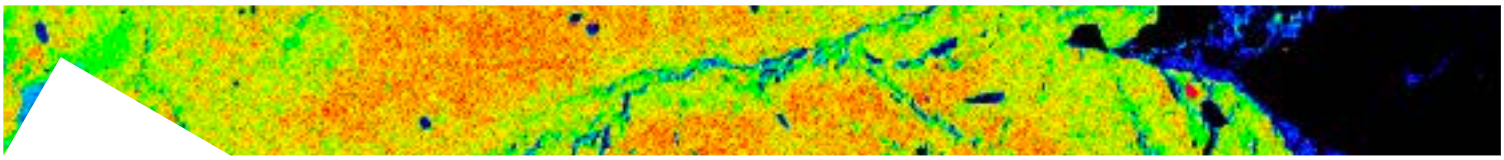

ing-effect" is investigated for the run at 180 °C/h by eating the sample up to 1400 °C and using a dwell time of 40 h. FE-SEM has been used to collect ~ 90 BSE images at magnifications from 150 to 10000 X. Textures are quantified on more than 50 microphotographs (Fig.1) by image analysis. Spinel (sp), clinopyroxene (cpx), plagioclase (plg) and glass are the main phases. Crystals are measured by their equal-area ellipse to determine 1) size (μm), 2) aspect ratio, 3) orientation of the major axis (°) and 4) #crystals/area (1/mm2). These data are used to calculate the crystal size distributions (CSDs, Fig.1) and the growth rates (Gmax and Gmean). From 1 to 60 °C/h, all the run products are holocrystalline, while the crystal content decreases as the cooling rate increases up to 9000 °C/h. Plg disappears at $\Delta T/\Delta t > 60$ °C/h, while cpx and sp are ubiquitous in all the run products. Sp crystals are always < 5 area%, while the cpx area% follows an antisymmetric gaussian trend, displaying a long tail at the more sluggish rates. Crystal shapes switch from faceted to dendritic from 60 to 180 °C/h. The aspect ratio of plg and sp increases as a function of $\Delta T/\Delta t$, while that of cpx does not show significant trends. Rapid cooling rates cause the increasing of #crystals/area, i.e. a great number of tiny crystals. The variation of $\Delta T/\Delta t$ on texture is well detected in the CSD-curves (Fig.1) for plg, cpx and sp. High $\Delta T/\Delta t$ condition results in CSD with: i) a restricted ΔL close to tiny sizes, a linear vertical trend and an upward shifting. Low $\Delta T/\Delta t$ conditions favor CSD with: i) a broad ΔL range, a curvilinear trend and a downward shifting. Maximum crystal lengths and CSD slopes allow us to determine the maximum (Gmax) and average (Gmean) growth rate. Both these parameters increase from 1 to 1800 °C/h for all the crystalline phase. Plg has the slowest growth rate, although it grows up to mm sizes, while cpx has a faster growth rate. The two growth rates are related by the function:

$$G_{max} = k\ Gmean\ (k = 2 \div 13).$$

Textures of MORB are strongly affected by cooling kinetics. Moreover, mm-sized plg and cpx and/or sp with size of several hundreds of μm can form in the post-eruptive stage.

Stratigraphy in an Etnean lava flow: post-emplacement differentiation

Giuliani L., Lanzafame G., Iezzi G., Nazzari M., Ferlito C., Mollo S., Casarin A., Piattelli V., Trabucco F., Colò M., Scarlato P.

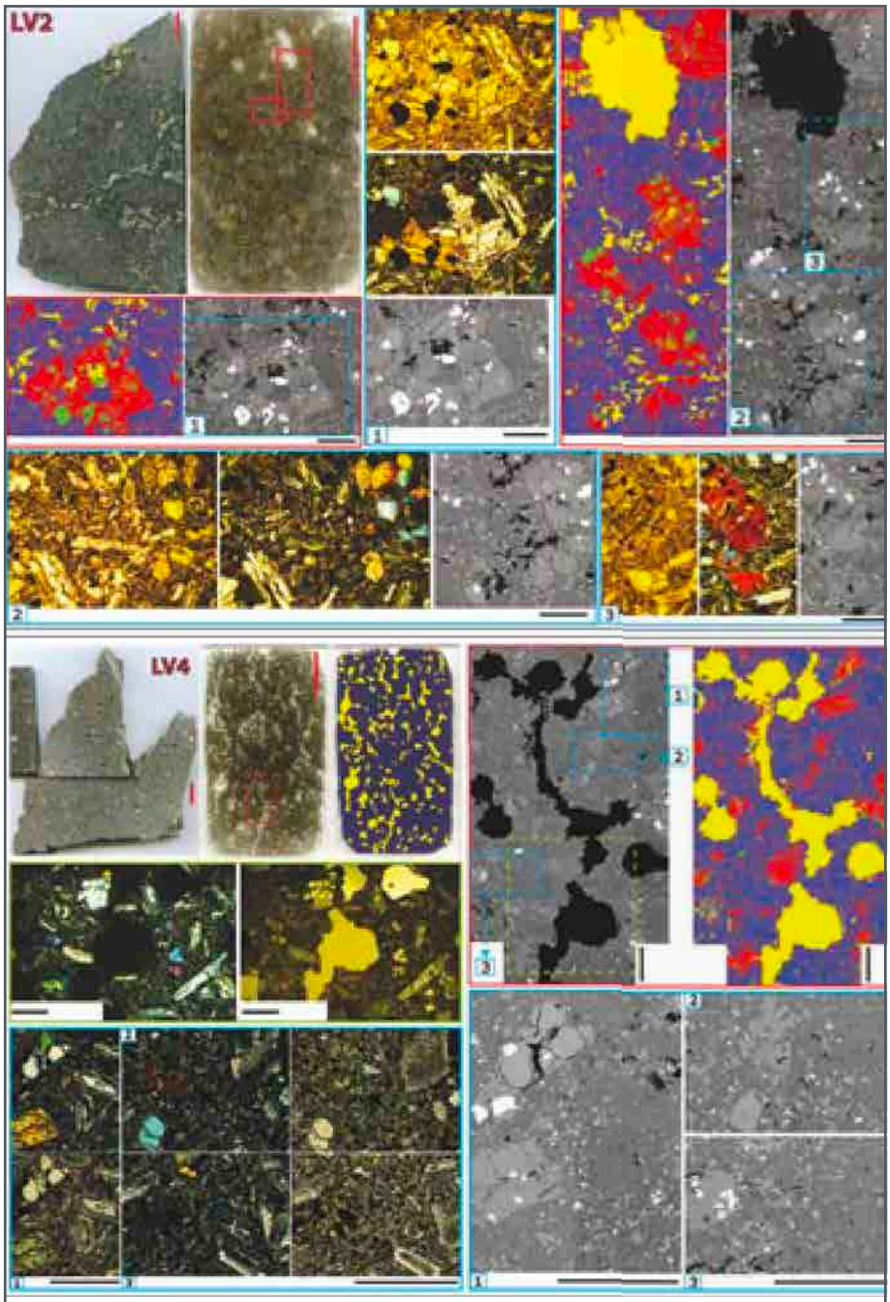

Fig. 1 I Representative textural features of two of the collected samples: LV4 (top) and LV2 (bottom). False colors indicate bubbles (yellow), cpx (red), plg + matrix (blue) and sp (green). Black and red bars correspond to 1 mm and 1 cm, respectively. Contours of boxes indicate the areas analyzed by SEM (red on thin section and blue on SEM-puzzles) and by TOM (green on SEM-puzzles).

A distal portion of a lava flow cropping in the Valle del Bove at Mount Etna volcano, emitted during the 1991-1993 eruptive activity has been investigated. The cropping section has height >2 m and is located at ~3 km far from the vents. We collected nine oriented samples with an approximate volume of 1 dm^3, moving from the carapace (LV9) to the lava bottom (LV1) at a sampling distance of ~20 cm. Their vertical sections coaxial to the flow direction and thickness have been polished and also used to prepare oriented thin sections. The dm-sized polished rock planes and thin sections have been imaged with a high-resolution scanner (HRS), to

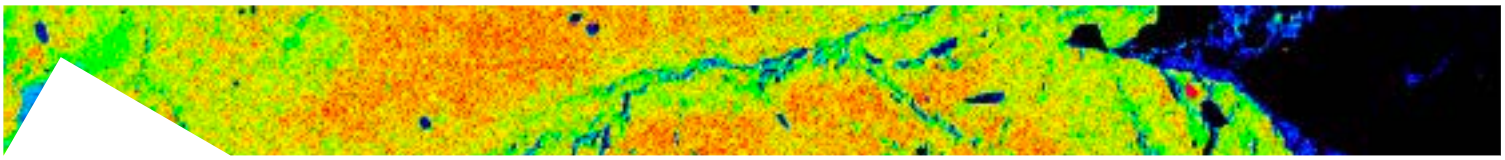

analyze and quantify the textural features of large phases. The thin sections have been also analyzed by transmission optical microscopy (TOM) and scanning electron microscopy (BS-SEM) at the HPHT Lab. The textural features collected by SEM have been acquired either by sequential and single microphotographs, to quantify both relatively large and tiny crystal phases (Fig. 1). Moving from the bottom to the top, the first three samples (LV1/LV3) are almost bubble-free, then tube-like bubbles appear (LV4) and the amount (area%) and size of vesicles increase (Fig.1). In parallel bubble number per area (#/area) generally decreases, envisaging a progressive coalescence with minor secondary events of nucleation. The other phases are plagioclase (plg), clinopyroxene (cpx), spinel (sp), olivine (ol) and glass. Plg and cpx have size up to a few mm, while sp and ol attain maximum lengths of some hundreds of µm. These data highlight that significant degassing keep occurring for kilometers during the flowing, inducing further nucleation or favoring additional growth of plg, cpx and sp. In turn, a significant part of crystalline phases has been developed after eruption. The textural and crystal-chemical data carried out from this lava section constrain the solidification of phases or portion of them occurred before and after flowing on Earth.

The origin of the K-Feldspar megacrysts hosted in the silica-rich products from Mt. Amiata (Southern Tuscany, Italy)

Landi P., La Felice S., Petrelli M., Vezzoli L.M., Principe C. M., Scarlato P.

The study was carried out in collaboration with colleagues of the IGG-CNR of Pisa and was partially financially supported by the Tuscan regional authority (Regione Toscana) in the framework of the LAMMA-CNR Project "Monografia vulcanologica del Monte Amiata" (Claudia Principe responsible).

The Mt. Amiata is a Quaternary volcanic complex, covering an area of about 90 km^2 and dominated by trachydacitic lava flows and lava domes. The rocks forming the younger lava domes and coulées are highly porphyritic and characterized by a peculiar abundance of K-feldspars megacrysts up to 5-6 cm in length, coupled with abundant mafic enclaves. Textural and chemical analyses of the K-feldspar megacrysts were performed in order to understand their origin and

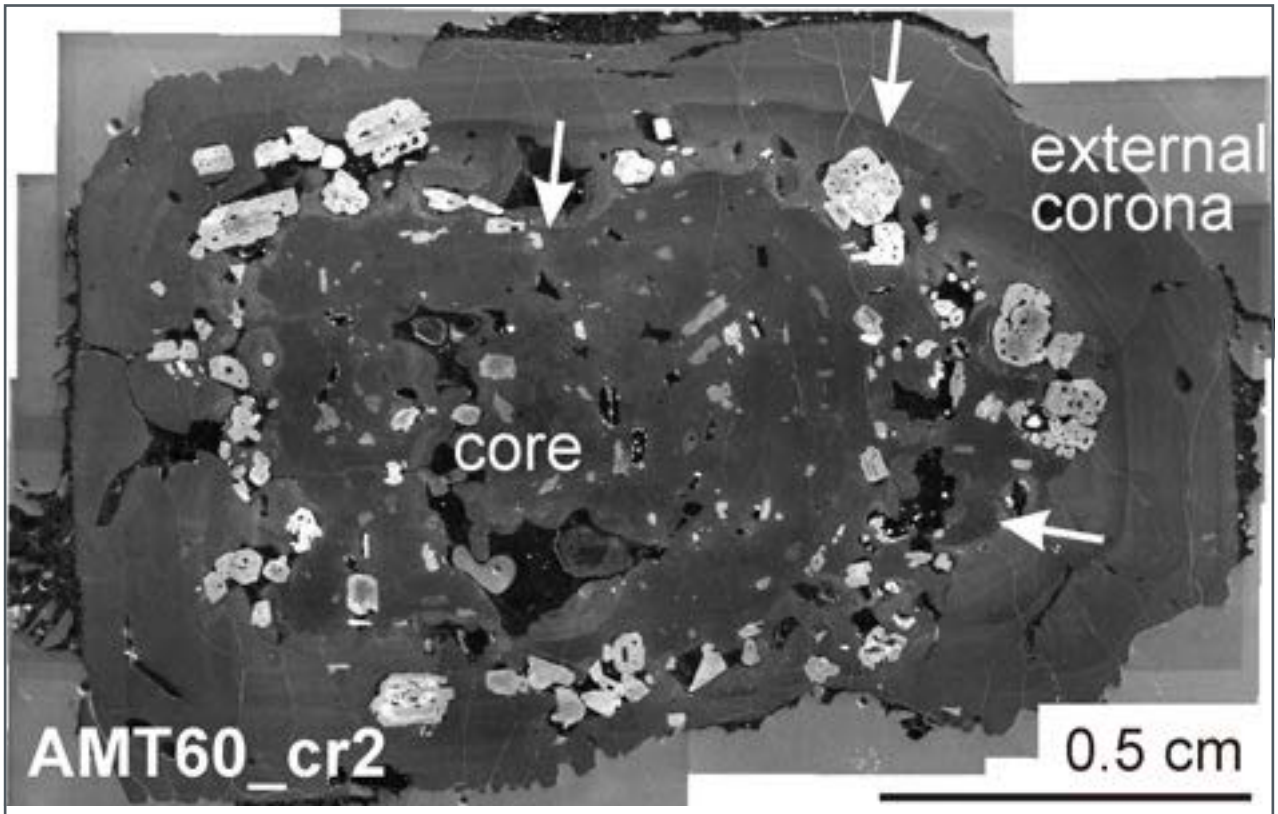

Fig. 1 I Mosaic of CL images of a K-feldspar megacrysts (Mt Amiata) showing the typical dusty internal portions formed by a large patchy zoned core which is surrounded by several zoned layers with rounded to resorbed boundaries and concentric alignments of mineral grains. Arrows indicate resorption surfaces.

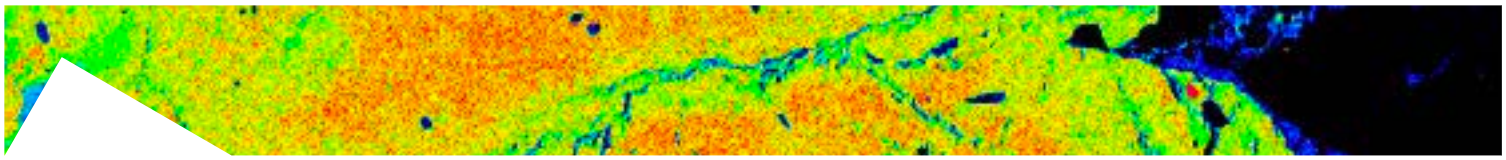

give insights into the crystallization processes and chemical evolution of the Mt. Amiata silica-rich magma.

The K-feldspar megacrystsare sanidine with composition between Or_{76} and Or_{83} (An_{1-4}, Ab_{16-21}) and large trace element variability (Ba 1100-8800 ppm; Sr 650-2350; Eu 2.5-7.3; Rb 350-450). Core to rim compositional transects reveal chemical oscillatory zoning patterns that are coupled with textural discontinuities observed in BSE and CL images. These zoning patterns originated by dissolution and regrowth episodes (disequilibrium and re-equilibration phases) related to the repetitive influx of mafic magmas and convection in the trachydacitic magma reservoir.The variable chemical composition of the K-feldspars is related to a different extent of hybridization during magma-mixing.

The study highlight that the abnormal dimension of the studied K-feldspars originates by the interplay between petrological and kinetic processes involving:

(i) extensive dissolution;

(ii) heterogeneous nucleation;

(iii) alternation of spasmodic growth events in disequilibrium and near-equilibrium crystallization.

Metamorphic xenoliths from Mt. Amiata volcanic complex

Lucci F., Della Ventura G., Conte A., Nazzari M., Rossetti F.

The focus of this ongoing project is at describing the petrology of metamorphic xenoliths included within the volcanic products erupted from Mt. Amiata volcanic complex, located in southern Tuscany.

After the built up of the Northern Appennines, late Miocene to Recent post-collisional magmatism evolved in extensional tectonic regime, in an area extending from southern Tuscany to the northern Thyrrenian Sea. The products of this magmatism are traditionally grouped in the so-called Tuscan Magmatic Province (TMP). Both magmatism and exten-

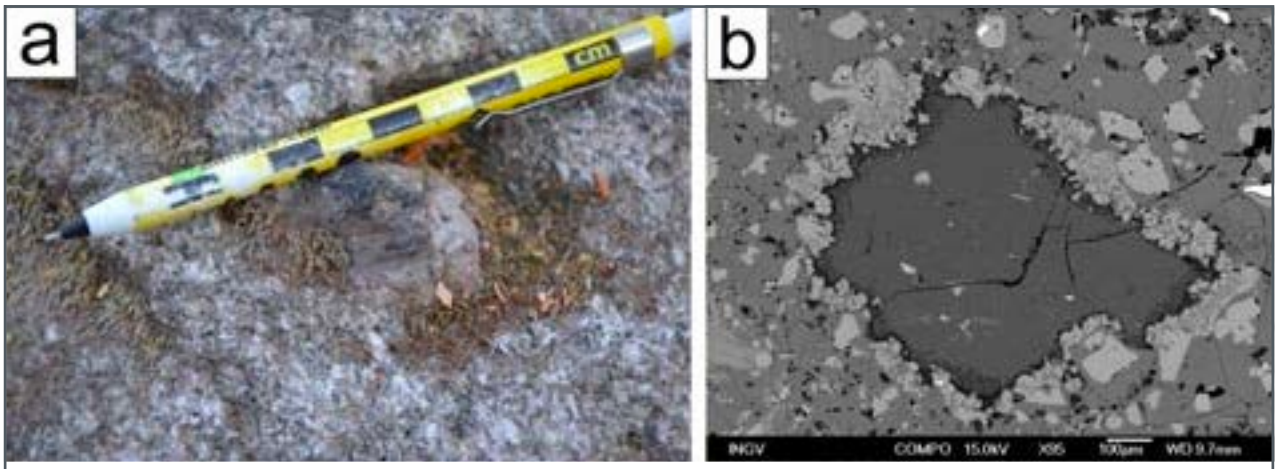

Fig. 1 I a) example of a metamorphic xenoliths enclosed within the Mt. Amiata lava; b) BSE images showing a typicalthermo-metamorphic corona texture showing the growth of dark mica + Fe-Mg spinels around andalusite.

sional tectonics migrated from west to east following the eastward migration of the Appennines collisional front.

The Mt. Amiata complex is characterized by felsic (SiO_2: 62-67 wt%) lavas and domes with an age of 0.3-0.2 Ma (Pleistocene), and represents one of the youngest magmatic evidences of the TMP. The Mt. Amiata (1738 m.a.s.l.) occupies an area of ca. 85 km^2 and consists of up to 1000 m thick volcanic products with a total estimated emitted volume of ca. 25-30 Km^3, covering a substratum made of shales, limestones and sandstones belonging to the Cretaceaous-Eocene allochtonous "Alberese-Pietraforte" Group.

According to the few existing works, all dating back to the 1980s, the abundant metamorphic lithics in Mt. Amiata products derived by a thermo-metamorphic event, due to the intrusion and emplacement of Mt. Amiata magmatic

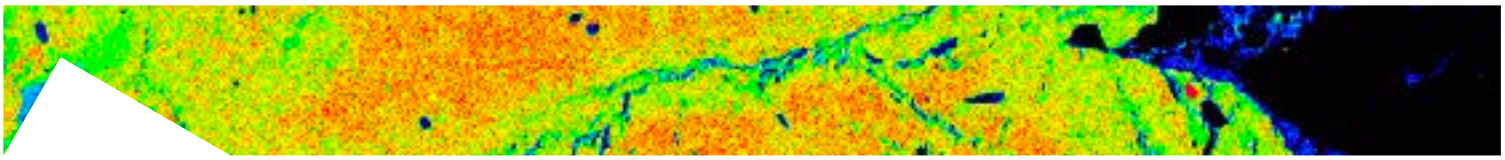

chamber(s), and superimposed on the previous regionally metamorphosed Paleozoic crystalline basement. However, few data are available on the pressure-temperature conditions of this thermo-metamorphic event, thus there is a limited knowledge on the anatomy of the plumbing system of the Mt. Amiata volcano.

Interestingly, rare Th, U and REE-bearing silicates were also reported from these metamorphic rocks, although a detailed description of these phases has never been provided.

The aim of this project is thus at addressing in details the mineralogy and geochemistry of the Mt. Amiata xenoliths, with the aim of understand the driving processes leading to the genesis and emplacement of a magmatic plumbing system in metamorphic basement.

Naturally Occurring Asbestos (NOA) in Sardinian Granitoid Rocks

Lucci F., Della Ventura G., Conte A., Nazzari M., Scarlato P.

The occurrence in nature of fibrous amphiboles (anthophyllite, actinolite, tremolite, crocidolite and amosite), and chrysotile, i.e., the six silicate minerals defined by the existing regulation as "asbestos", is increasingly attracting attention in environmental hazard evaluation. In natural environments, the NOA (natural occurring asbestos) hazard arises when physical/mechanical processes produce airborne fibres that, due to their low density and small size, can be widely dispersed and, therefore, contaminate the atmosphere and water supplies.

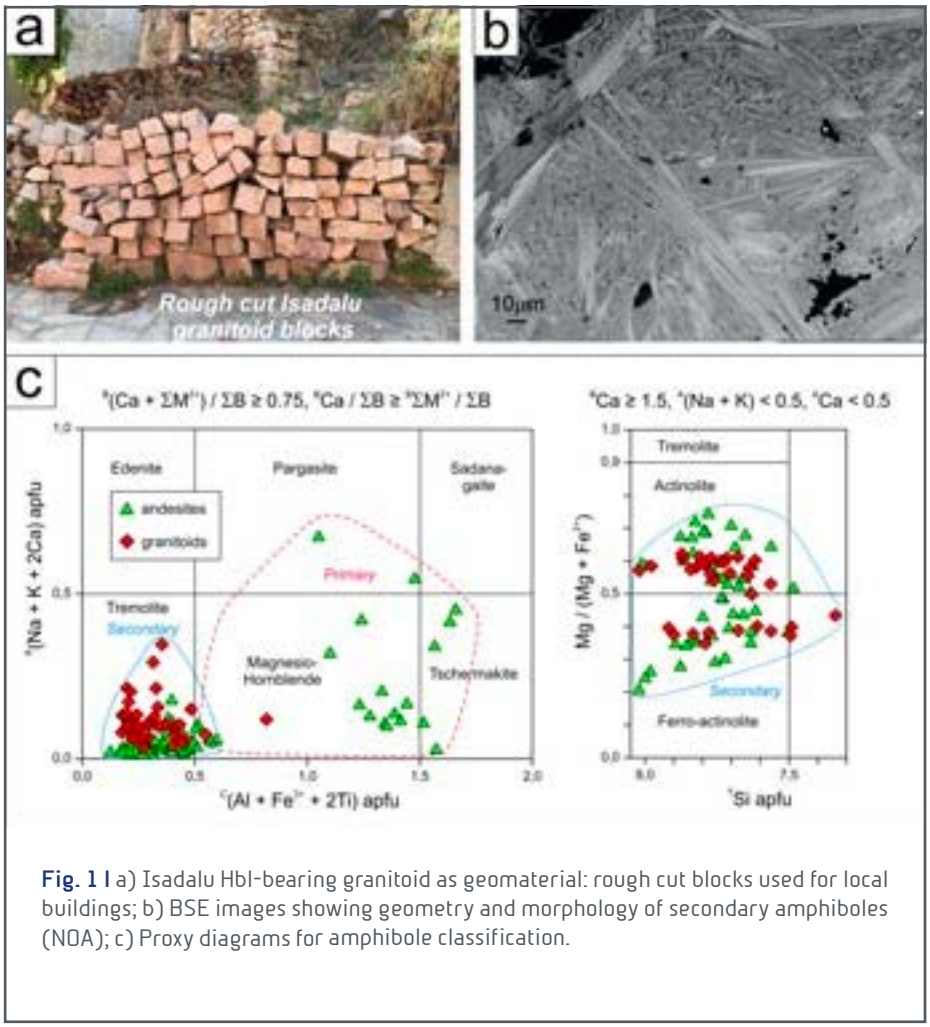

Fig. 1 I a) Isadalu Hbl-bearing granitoid as geomaterial: rough cut blocks used for local buildings; b) BSE images showing geometry and morphology of secondary amphiboles (NOA); c) Proxy diagrams for amphibole classification.

Natural processes (erosion and transport) as well as anthropic activities (mining, crushing, grinding and milling), thus represent an important source of asbestos. Both processes may induce a strong environmental hazard that can be quantified as a function of the concentration of dispersed fibres in air and in soil/water.

It is recognized that asbestos minerals are typical of mafic and ultramafic rock sequences. In these rocks, a wide range of geological processes, such as shear deformation and fluid-rock interaction, may produce a strong rock alteration and serpentinization, associated with a widespread growth of asbestiform amphiboles. However, despite the relevance of these occurrences and related geological phe-

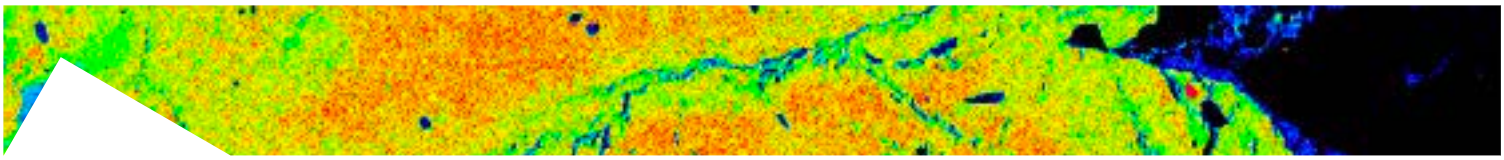

nomena, we still have a very limited knowledge of the distribution of fibrous amphibole in acid rocks and, specifically, in metaluminous granitoids rich in Ca-inosilicates, that may undergo hydrothermal alteration.

In this work, we address an intriguing example of NOA in granitoid rocks from the Isadalu Permian hypabyssal felsic massif outcropping in northern Ogliastra (Central Sardinia, Italy). The Isadalu complex has been selected as a case study for a multidisciplinary approach (based on a field-survey combined with textural, mineralogical and petrological investigation) aimed at evaluating the asbestos hazard. In the studied area, fibrous amphibole-bearing granitoids have been used for centuries for house-building (a typical case of non-occupational exposure), and strategic infrastructures (pipes and penstocks of the hydroelectric plants and local roads) have been developed, maintained and modernized, since the 1948 (occupational exposure) using these geomaterials.

One mafic and two felsic samples representative of main NOA-bearing magmatic lithologies from the area of Isadalu complex were selected for petrographic investigations and mineral chemistry on polished thin sections. Fabric observations allow recognizing a scenario of a secondary NOA-bearing paragenesis superimposed over a pristine primary magmatic assemblage. Furthermore, the invariably isotropic fabric of this secondary paragenesis, together with its widespread diffusion in the studied rocks clearly indicates a deformation-free (isotropic fabrics) and fluid-rich (chlorite-epidote veins) processes for the actinolite-tremolite formation.

To understand the thermobaric environment associated with crystallization of the secondary Act/Tr-bearing paragenesis in Isadalu granitoids, we applied conventional thermobarometric models based on major element mineral chemistry, and estimated T = 470 ± 30 °C at P = 1.0 ± 0.5 kbar.

These results indicate that Act-bearing paragenesis formed in greenschist facies conditions at a very superficial crustal depth (3-4 km).

Transient to stationary radon emissions from highly crystalline rocks exposed to subvolcanic temperatures in laboratory

Mollo S., Tuccimei P., Soligo M., Galli G., Iezzi G., Scarlato P.

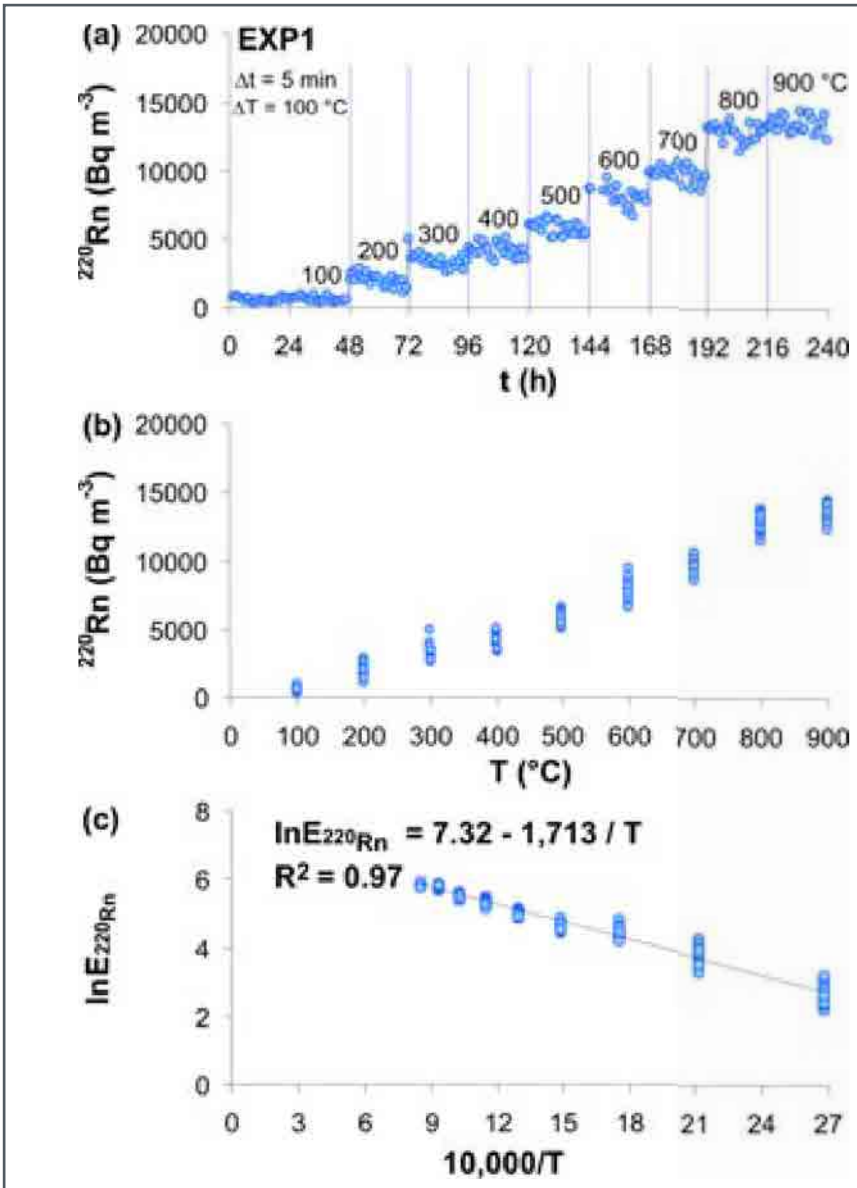

Fig. 1 I Results from EXP1 plotted in 220Rn vs. t (a), 220Rn vs. T (b) and E220Rn vs. 10,000/T (c) diagrams. The rock sample was first kept at 100 °C for 48 h. Then, through a heating ramp (dt) of 5 min, the temperature (dT) was increased by 100 °C and maintained constant for 22 h. This incremental step was replicated eight times (5 min dt and 100 °C dT) up to the maximum experimental temperature of 900 °C.

Rock substrates beneath active volcanoes are frequently subjected to temperature changes caused by the input of new magma from depth and/or the intrusion of thin-to-thick magma bodies within the subvolcanic lithological formations. The primary effect of the influx of hot magma is the heating of the surrounding host rocks with the consequent modification of their physicochemical features. In this respect, we have performed radon thermal experiments on a phonolitic rock exposed to temperatures in the range of 100-900 °C, with the aim to reproduce the most common subvolcanic thermal regimes. Results from these experiments indicate that transient radon signals are not unequivocally related to substrate deformation caused by tectonic stresses, but rather to a temperature-dependent diffusion of radionuclides through

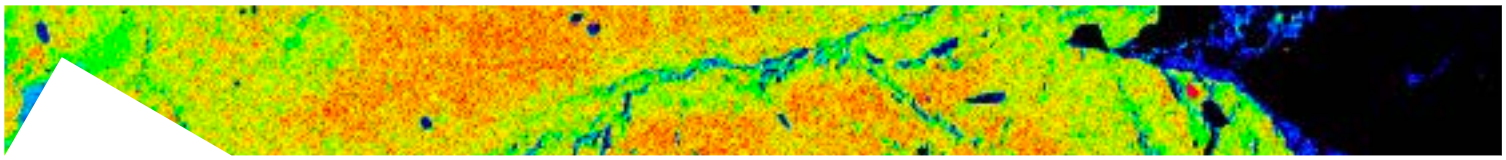

the structural discontinuities of the rocks which serve as preferential pathways for gas release. However, it has been also observed that intense heating/cooling cycles are accompanied by rapid expansion and contraction of minerals. This strong thermal shock condition produces both inter- and intra-crystal microfracturing, as well as the formation of macroscopic faults. The increased number of diffusion paths intensifies dramatically the radon atom migration, giving reason for a stationary background level that is invariably much higher than the temperature-dependent transient changes.

Advancements in understanding the radon signal in volcanic areas: A laboratory approach based on rock physico-chemical changes

Mollo S., Tuccimei P., Soligo M., Galli G., Scarlato P.

Radon monitoring represents an important investigation tool for environmental changes assessment and geochemical hazard surveillance. Despite anomalous radon emissions are commonly observed prior to earthquakes or volcanic eruptions, radon monitoring alone is not yet successful in correctly predicting these catastrophic events because contrasting radon signals are unexpectedly measured by lithologically distinct areas. This contribution aims to summarize and integrate natural and laboratory studies pertaining to the transport behavior of radon in different rock types experiencing variable stress and thermal regimes at subvolcanic conditions. The final purpose is to ignite novel and pioneer experimental researches exploring the causes and consequences of radon anomalous emissions, in order to elucidate in full the relationship between the physico-chemical changes of substrate rocks and the radon signal.

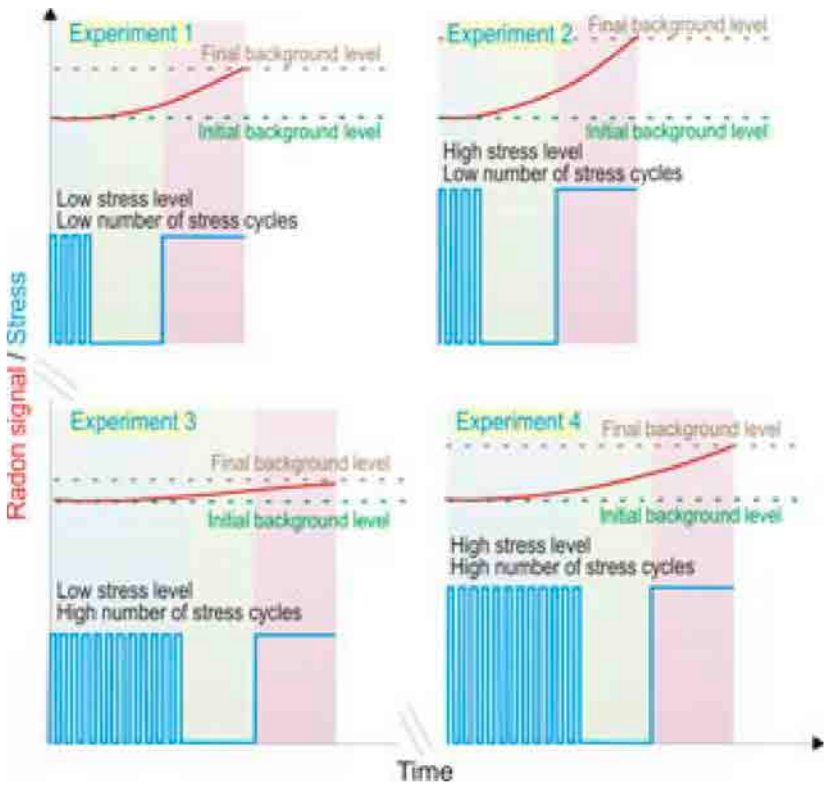

Fig. 1 I Simplified sketch illustrating changes in stress condition and radon signal as a function of time. Four different uniaxial deformation experiments are presented. Experiment 1 and Experiment 2 consist of a low number of stress cycles where the specimen is loaded and unloaded over time. At the end of the cycles, the stress condition is released for several days, and then increased to low stress for Experiment 1 and to high stress for Experiment 2. Experiment 3 and Experiment 4 are performed by adopting the same conditions of Experiment 1 and Experiment 2, but the specimen is subjected to a high number of stress cycles. The experiments are conducted on a loosely consolidated, vesicular tuff.

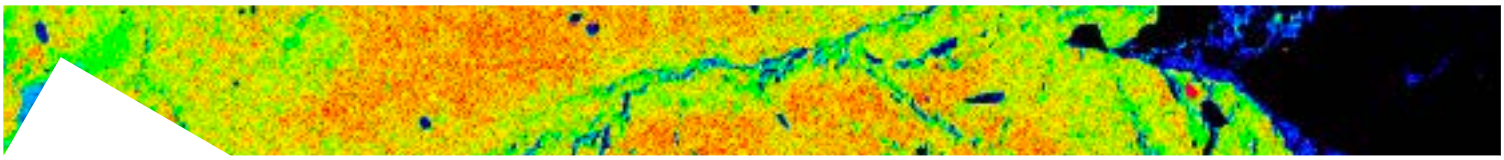

An integrated P-T-H_2O-lattice strain model to quantify the role of clinopyroxene fractionation on REE+Y and HFSE patterns of mafic alkaline magmas: Application to eruptions at Mt. Etna

Mollo S., Blundy J., Scarlato P., De Cristofaro S.P., Tecchiato V., Di Stefano F., Vetere F., Holtz F., Bachmann O.

A correct description and quantification of the geochemical behaviour of REE+Y (rare earth elements and Y) and HFSE (high field strength elements) is a key requirement for modeling petrological and volcanological aspects of magma dynamics. In this context, mafic alkaline magmas (MAM) are characterized by the ubiquitous stability of clinopyroxene from mantle depths to shallow crustal levels. On one hand, clinopyroxene incorporates REE+Y and HFSE at concentration levels that are much higher than those measured for olivine, plagioclase, and magnetite. On the other hand, the composition of clinopyroxene is highly sensitive to variations in pressure, temperature, and melt-water content, according to exchange-equilibria between jadeite and melt, and between jadeite/Ca-Tschermak and diopside-hedenbergite. As a consequence, the dependence of the partition coefficient on the physicochemical state of the system results in a variety of DREE+Y and DHFSE values that are sensitive to the magmatic conditions at which clinopyroxenes nucleate and grow. In order to better explore magma dynamics using clinopyroxene chemical changes, an integrated P-T-H_2O-lattice strain model specific to MAM compositions has been developed. The model combines a set of refined clinopyroxene-based barometric, thermometric and hygrometric equations with thermodynamically-derived expressions for the lattice strain parameters, i.e., the strain-free partition coefficient (D_0), the site radius (r_0), and the effective elastic modulus (E). Through this approach, it is found that the incorporation of REE+Y and HFSE into M2 and M1 octahedral sites of clinopyroxene is determined by a variety of physicochemical variables that may or may not change simultaneously during magma differentiation. The applicability of the P-T-H_2O-lattice strain model to natural environments has been verified using clinopyroxene-melt pairs from a great number of volcanic eruptions at Mt. Etna volcano (Sicily, Italy). DREE+Y and DHFSE values recovered by the model have been used as input data to quantify fractional crystallization processes in natural MAM compositions. Results from calculation illustrate that the

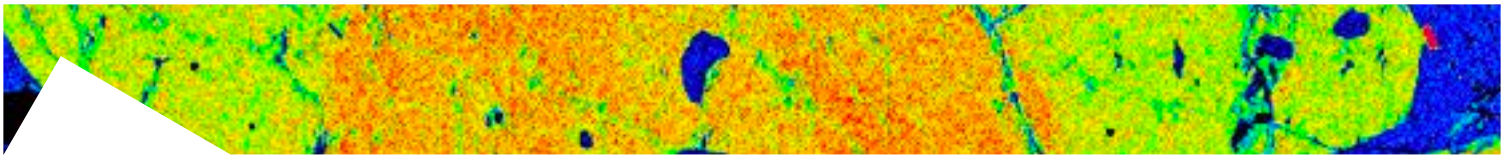

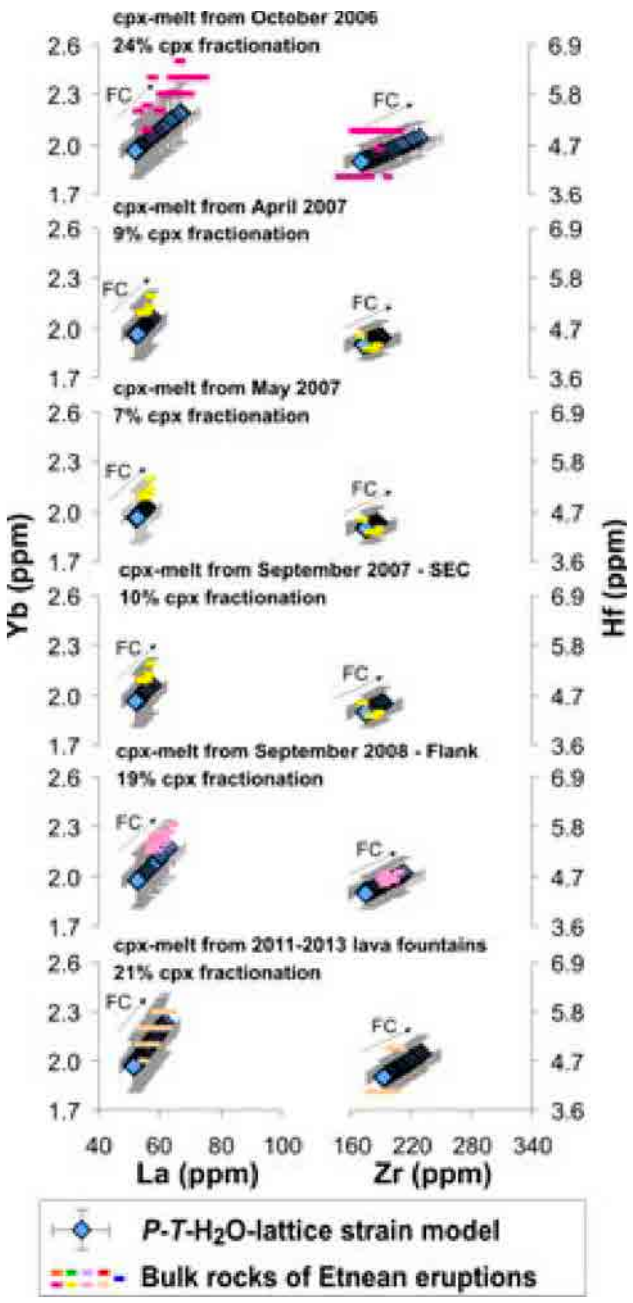

Fig. 1 I Clinopyroxene fractional crystallization modeling. DREE+Y and DHFSE change continuously for the trace element of interest, in concert with the variable physicochemical conditions of the system (i.e., P, T, H_2O, and crystal/melt compositions). This is possible by stepwise calculations performed by using different clinopyroxene-melt pairs at each step of fractionation. For all the calculations, the Monte Maletto composition was assumed as the primitive magma (La = 50.7, Yb = 1.96, Zr = 191, and Hf = 4.3).

concentration of REE+Y and HFSE in the magma is primary controlled by the geochemical evolution of clinopyroxene in terms of major cation exchange-equilibria and trace cation lattice strain properties.

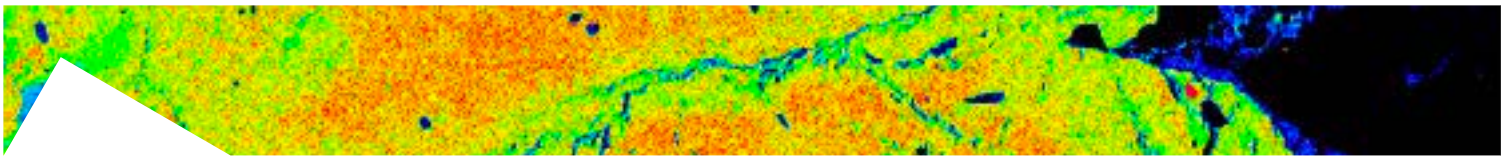

Impulsive supply of volatile-rich magmas in the shallow plumbing system of Mt. Etna volcano

Perinelli C., Mollo S., Gaeta M., De Cristofaro S.P., Palladino D.M., Scarlato P.

Magma dynamics at Mt. Etna volcano are frequently recognised as the result of complex crystallization regimes that, at shallow crustal levels, unexpectedly change from H_2O-undersaturated to H_2O-saturated conditions due to impulsive and irregular arrival of volatile-rich magmas from mantle depths. On this basis, we have performed hydrous crystallization experiments for a quantitative understanding of the role of H_2O in the differentiation of deep-seated trachybasaltic magmas at the key pressure of the Moho transition zone. For H_2O = 2.1-3.2 wt.%, the original trachybasaltic com-position shifts towards phonotephritic magmas never erupted during the entire volcanic activity of Mt. Etna. Conversely, for H_2O = 3.8-8.2 wt.%, the obtained trachybasalts and basaltic trachyandesites reproduce most of the pre-historic and historic eruptions. The comparison with previous low pressure experimental data and natural compositions from Mt. Etna provides explanation for (1) the abundant release of H_2O throughout the plumbing system of the volcano during impulsive ascent of deep-seated magmas, (2) the upward acceleration of magmas feeding gas-dominated, sustained explosive eruptions, (3) the physicochemical changes of gas-fluxed magmas ponding at shallow crustal levels, and (4) the huge gas emissions measured at the summit craters and flank vents which result in a persistent volcanic gas plume.

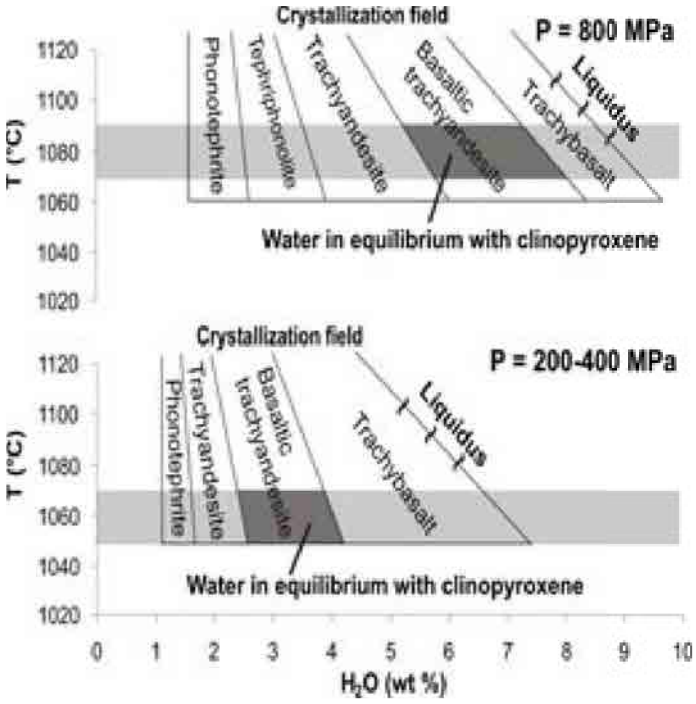

Fig. 1 | Temperature vs. H_2O diagram derived using data from hydrous crystallization experiments conducted at high (800 MPa from this study) and moderate (200-400 MPa from literature) pressures. Considering the natural P-T constrains of 2011-2013 lava fountains, it has been reconstructed the amount of H_2O in equilibrium with clinopyroxene phenocrysts. At 800 MPa and 1070-1090 °C, the basaltic trachyandesitic magma is saturated with clinopyroxene when the amount of H_2O is 5.2-8 wt.%. Conversely, at 200-400 MPa and 1050-1070 °C, the H_2O content decreases to 2.5-4 wt.%.

Olivine compositional changes in primitive magmatic skarn environments: A reassessment of divalent cation partitioning models to quantify the effect of carbonate assimilation

Di Stefano F., Mollo S., Scarlato P., Nazzari M., Bachmann O., Caruso M.

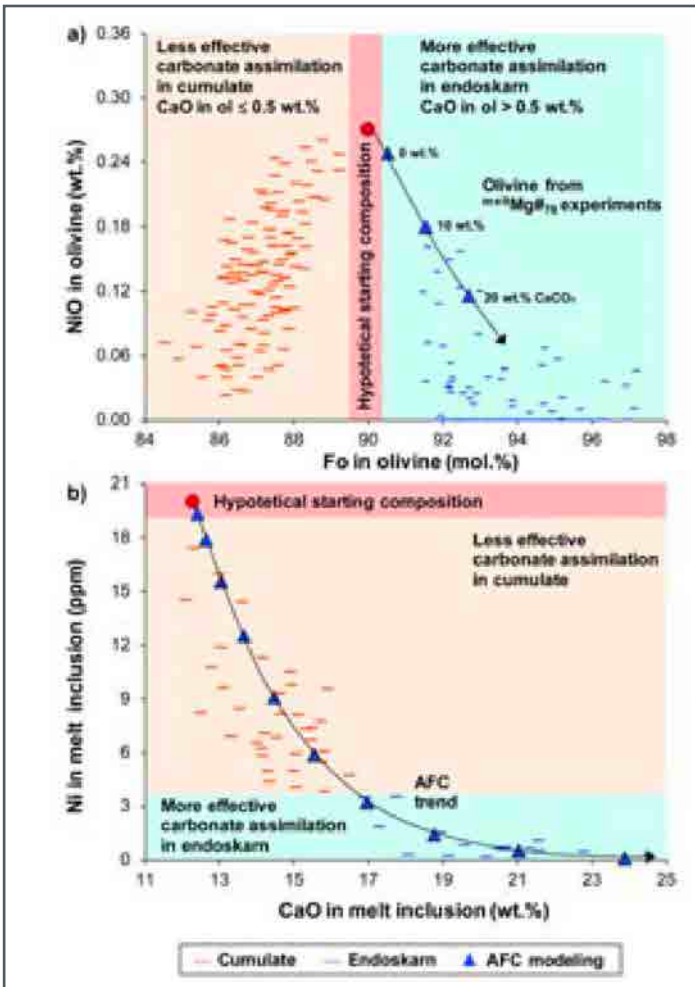

Fig. 1 I Natural products from the Colli Albani Volcanic District (CAVD) in Italy are compared with those from this study. The NiO vs. Fo diagram displays the chemical changes of olivine phenocrysts found in cumulates and endoskarns at CAVD (a). Results from $^{melt}Mg\#_{78}$ decarbonation experiments confirm that Ni is negatively correlated with Fo, as the amount of carbonate assimilated increases from 0 to 10 to 20 wt.%. The Ni vs. CaO diagram shows the contamination path of melt inclusions entrapped in the same olivine phenocrysts (b). The melt inclusion with the highest Ni and lowest CaO contents is used as starting composition to track the combined effects of assimilation and fractional crystallization (AFC). Olivine-melt partition coefficients of Ca (DCa = 0.15) and Ni (D_{Ni} = 11.22) are used. The CaO content of the assimilant is set to 45 wt.%. The amount of fractionated olivine is lower than 8% and the ratio of the assimilation rate to the crystallization rate changes from 0.01 to 0.2.

The geochemical evolution of olivine from primitive magmatic skarn environments has been studied by atmospheric pressure experiments carried out at 1250, 1200, and 1150 °C under QFM oxygen buffering conditions. The starting materials were three synthetic basalts (i.e., $^{melt}Mg\#_{78}$, $^{melt}Mg\#_{75}$, and $^{melt}Mg\#_{72}$) doped with variable amounts of $CaCO_3$, in order to reproduce the natural concentration levels of CaO-rich magmas interacting with the skarn rock shells. Results from decarbonation experiments evidence that the crystallization of Fo-CaO-rich, NiO-poor olivines is more favored at higher temperatures when primitive basaltic magmas assimilate increasing amounts of carbonate materials. The number of large size Ca cations entering olivine crystal lattice is proportional to the amount of Ca-O-Si bonds available in the melt. Due to differences between Fe^{2+} and Mg cation radii, the Ca-Fe^{2+} substitutions into M2

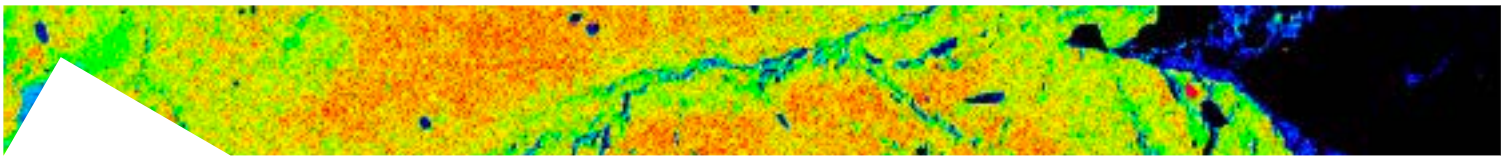

crystallographic site are more facilitated than Ca-Mg ones, thus enhancing the forsterite component in olivine. The partitioning behavior of Ni, Mg, Fe^{2+}, Mn, and Ca between olivine and melt has been also investigated to better understand cation redistribution mechanisms at the magma-carbonate reaction zone. In this context, some partitioning models from the literature have been refined to more accurately quantify the geochemical evolution of primitive skarn systems. Under the effect of $CaCO_3$ assimilation, the partitioning of divalent cations, can be parameterized as a function of temperature, bulk composition (mostly, CaO and MgO contents in both olivine and melt) and melt structure (expressed as the number of non-bridging oxygens per tetrahedrally coordinated cations). Conversely, the exchange partition coefficients between Fe^{2+}/Ca/Mn/Ni and Mg do not vary significantly as a function of temperature and $^{melt}Mg\#$, due to the limited influence of these parameters on the melt structure. In turn, cation exchange reactions are primarily controlled by the strong depolymerizing effect of $CaCO_3$ assimilation that increases the number of structural sites critically important to accommodating network-modifying cations in the melt phase. The comparison between cumulates and magmatic skarns from the Colli Albani Volcanic District (Italy) and experiments from this study provides quantitative constraints on the geochemical evolution of olivine phenocrysts and their melt inclusions as a function of carbonate assimilation.

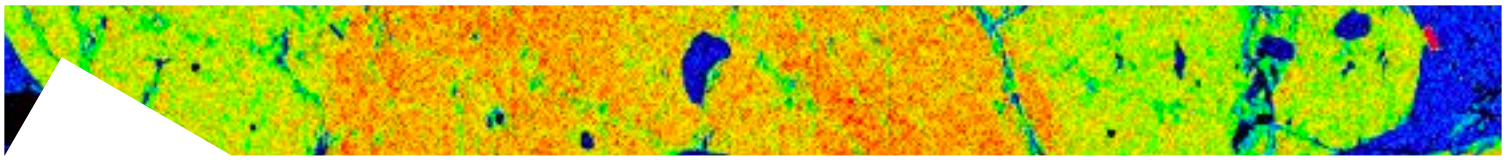

The effect of CaO on the partitioning behavior of REE, Y and Sc between olivine and melt: Implications for basalt-carbonate interaction processes

Di Stefano F., Mollo S., Blundy J., Scarlato P., Nazzari M., Bachmann O.

The partitioning of REE, Y and Sc (R^{3+}) between olivine and melt has been investigated experimentally during basalt-carbonate interaction. Three synthetic basalts ($^{melt}Mg\#_{72}$, $^{melt}Mg\#_{75}$ and $^{melt}Mg\#_{78}$) were doped with 0, 10 and 20 wt.% $CaCO_3$ and then equilibrated for 72 h at 1 atm, 1150, 1200 and 1250 °C, and the QFM oxygen buffer. The thermal decomposition of $CaCO_3$ produced CaO contents in the melt up to ~22 wt.%. Regular relationships are found between the ionic radius and the partition coefficient (D_{R3+}), showing typical near-parabolic patterns. D_{R3+} is weakly dependent on temperature, but decreases with increasing $CaCO_3$ in the starting material (e.g., D_{Sc} decreases from 0.20 to 0.13). From the point of view of the lattice strain theory, is described in terms of the radius of the crystal site (r_0), the Young Modulus (E) due to the elastic response of that site to lattice strain caused by cation insertion, and the strain-free partition coefficient (D_0). The value of r_0 decreases as Ca cations are accommodated into the more distorted M2 site of olivine via progressive Ca-Fe substitutions. This mechanism is accompanied by a higher proportion of Mg cations entering into the smaller M1 site, making the optimum ionic radius smaller and favoring the crystallization of more forsteritic olivines from decarbonated melts. The enrichment of Ca in the crystal lattice is also proportional to the number of Si and Ca cations available in the melt. This causes E to be anticorrelated either with Ca in olivine or the activity of Ca_0 in the melt. R^{3+} cations behave as network modifiers and, during basalt-carbonate interaction, the increasing abundance of non-bridging oxygens enhances the solubility of REE, Y and Sc in the melt. As a consequence, D_0 is negatively correlated with the degree of melt depolymerization. Additionally, the strain of the crystal lattice dominates the DR^{3+} parabolic patterns and D_0 is strongly controlled by forsterite and aluminium concentrations in olivine. The accommodation of REE, Y and Sc in the crystal lattice requires maintenance of local charge-balance by the generation of vacancies, in accord with a paired substitution of R^{3+} and a vacancy for Mg in octahedral sites.

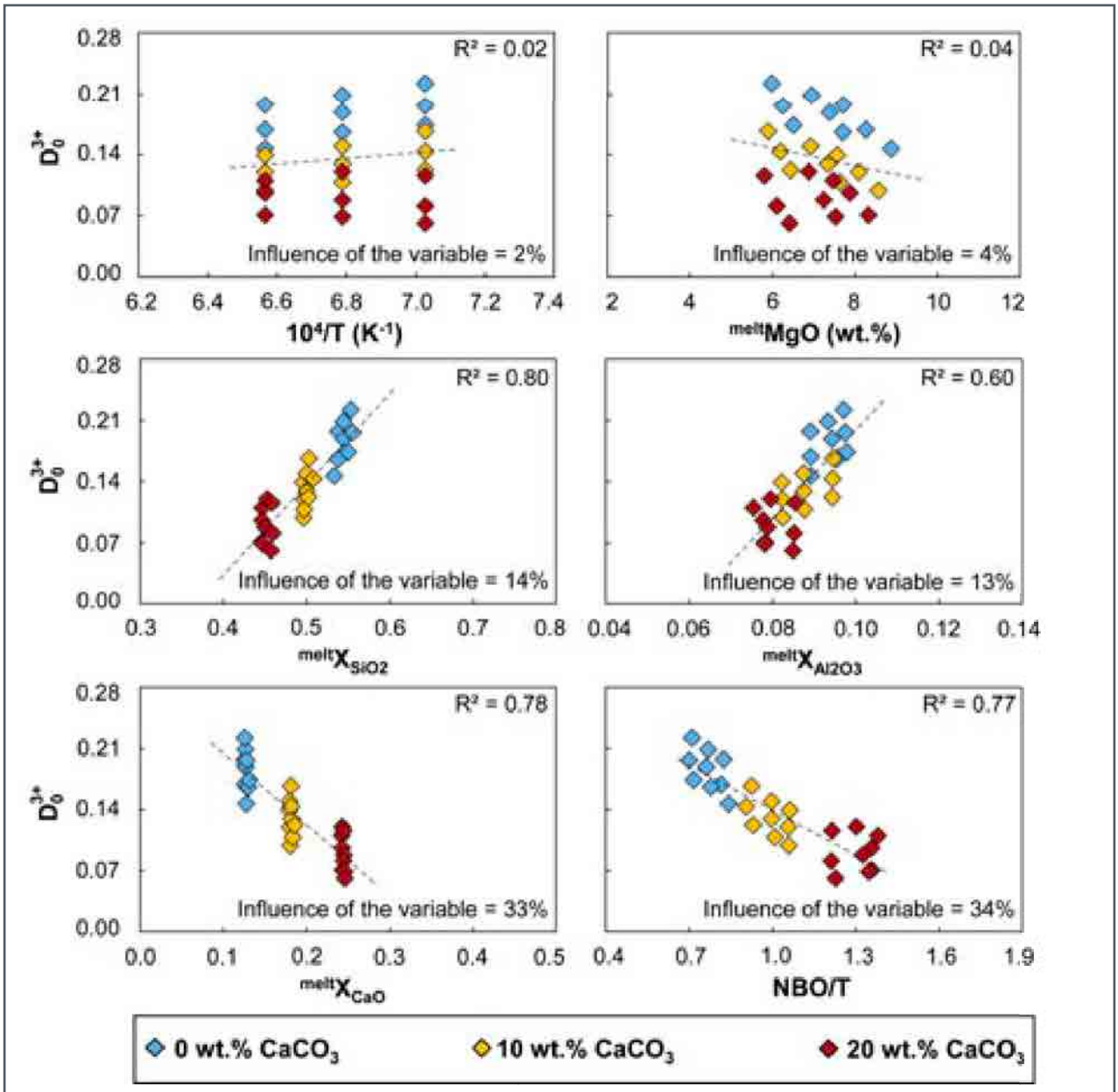

Fig. 1 | Relationship between the strain-free partition coefficient, temperature and melt components.

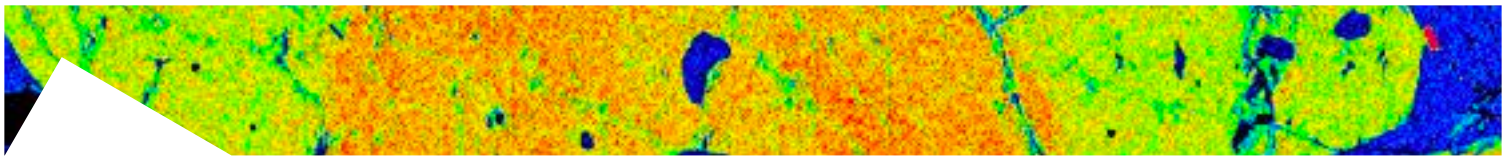

Phase Equilibria within a Carbonated Subducted Oceanic Crust at Transition Zone-Lower Mantle Conditions

Monaco L., Stagno V., Nazzari M., Scarlato P., Greaux S., Irifune T.

Sub-lithospheric diamonds, also known as super deep diamonds, form at depths greater than 200 km underneath cratons and oceanic crust. They represent a powerful tool to investigate the chemical composition and mineralogy of the Earth' s interior, in addition to the information generally obtained by combining the knowledge of seismic-waves velocity associated to natural earthquakes along with laboratory experiments that reproduce the mineral assemblage of inaccessible deep portions of the Earth. Super deep diamonds can host minerals formed in the transition zone and lower mantle corresponding to depths of 410-700 km representing, therefore, natural "rocky" samples (i.e. observations) of the Earth's interior. Among the inclusions hosted in diamonds, majoritic garnet is extremely important, since this phase can provide valuable information of the temperature, pressure and redox conditions at which sub-lithospheric diamonds likely crystallized. The main goal of this study was to experimentally investigate the chemical composition of common mineral silicates representative of the transition zone and lower mantle when coexisting with diamond and carbonate minerals or melts. We performed experiments in the pressure ranges of 14-28 GPa and temperatures between 800-1400 °C using the 2000t press available at the Geodynamics Research Center (Ehime University, Japan). Experiments were carried out using graphite capsules filled with a mixture of synthetic minerals, carbonates and oxide to simulate a synthetic diamond (as graphite turns to at high pressure) hosting mantle minerals. The recovered run products were embedded in epoxy resin, polished and then investigated with both field emission scanning electron microscope (FE-SEM), for textural observations and chemical analyses on synthetic minerals. Textural and chemical analyses showed the coexistence of Fe-bearing majorite along with diamonds and carbonates plus additional accessory phases like stishovite, rutile, ilmenite, and kyanite. The chemical composition of the synthetic majoritic garnet is compatible with the ones of natural inclusions in diamonds reported in literature. In addition, a majorite with stoichiometry resembling that of omphacitic clinopyroxene was recovered from our experiments. Results from this study can be used to link the chemistry and mineralogy of the deep interior of Earth with diamonds-forming processes.

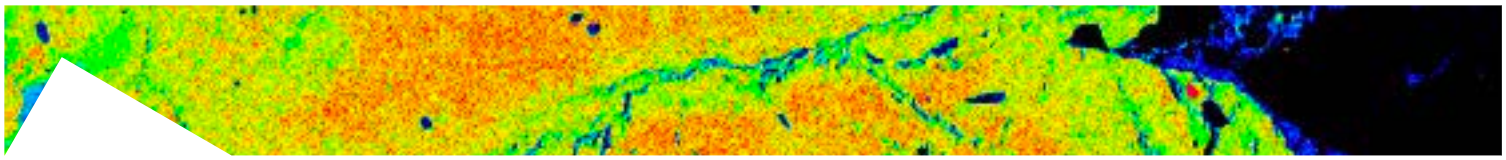

Integrated natural and experimental investigation of alkaline liquid lines of descent in the Dunedin Volcano, New Zealand

Pontesilli A., Brenna M., Mollo S., Masotta M. Nazzari M., Scarlato P.

Magma mixing and mingling processes in volcanic systems are crucial both for their role in the evolution and differentiation of magmas and for their potential as eruption triggers. In this context, the reconstruction of physico-chemical conditions relevant to magma differentiation processes at different levels in the crust requires constraint from detailed micro-chemical data on the heterogeneous crystal cargo brought by the magmas to the surface. Moreover, high-pressure high temperature phase equilibria experiment represents an invaluable source of information on the liquid line of descent followed by differentiating parental composition and on the compositions of equilibrium mineral phases fractionating along these evolutionary paths. The Dunedin Volcanic Complex (Otago region, southern New Zealand)represents the intraplate alkaline volcanic system in which the liquid line of descent leading to either trachyte or phonolite magma compositions were originally proposed. Compelling evidences for the occurrence of mixing processes in magmatic products are common in both primitive and more evolved rocks. Textural features of the commingled hybrid magmas include resorption and overgrowth of the phenocrysts, along with systematic variations in their mineral compositions in distinctive chemical zonings and crystal populations (fig.1). Thermobarometric estimates from clinopyroxene and amphibole crystals in the primitive to intermediate eruptive products suggest that fractionation and mixing occurred at lower to mid-crustal depths (5 – 10 kbar), while the shallower portions of this complex plumbing system extends to the uppermost parts of the crust, where the more evolved magmas are produced (2-3 kbar). Experimental investigations have been conducted on primitive (alkali basalt) and intermediate (basaltic trachyandesite) starting compositions, at a range of temperature (from 900 to 1100°C), water contents (from 1 to 7 wt.%) and pressures (5, 9 kbars). Preliminary results suggest that variations in phase assemblage crystallizing from alkaline magmas at different depths and water contents determine their evolution along distinctive liquid line of descents, characterized by either a mildly or stronger alkaline character, and ultimately leading to the production of magmas having respectively trachytic or phonolitic compositions. Results from this

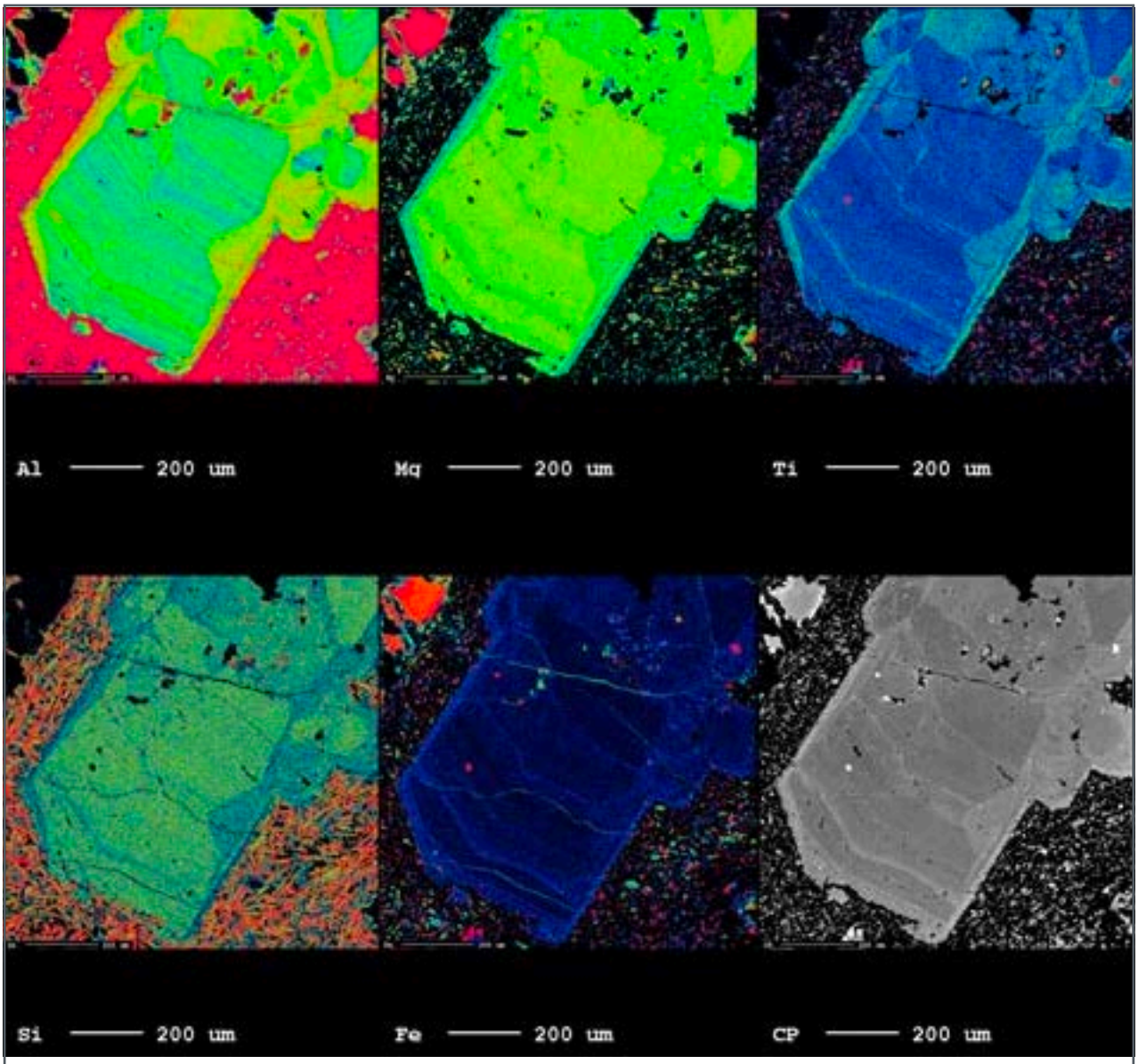

Fig. 1 I Major elements maps of a clinopyroxene (titanoaugite) phenocryst in an alkali basaltic lava from the Dunedin Volcano. Cold colors denote low concentrations, while higher concentrations are represented by warm colors. Repeated variations in mineral composition represented by the oscillatory zoning in major elements witness recurrent changes in former equilibrium melt composition, related to magma dynamics in the plumbing system, as for instance events of mafic recharge.

work highlights how complex magmatic processes in poly-baric environments can account for the great compositional variability observed in alkaline polygenic systems, without the involvement of variations in the parental melt compositions. Detailed micro-chemical and micro-textural data on the crystalline populations of the magmatic products are especially relevant in tracking back the compositions of the former equilibrium melt compositions, allowing for a more accurate comparison between the natural and the experimental data.

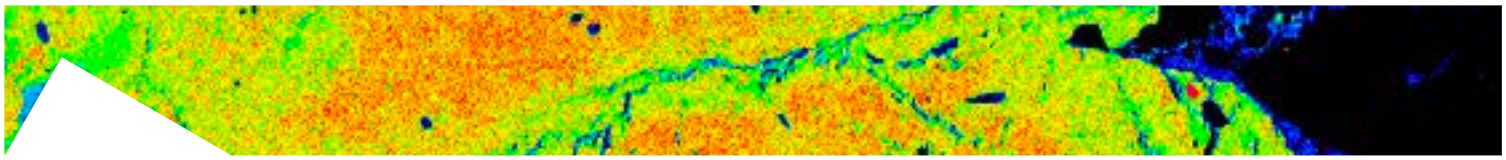

Rheology and melt structure of CO_2-bearing melts at Earth's upper mantle pressures and temperature conditions

Stopponi V., Stagno V., Kono Y., Nazzari M., Scarlato P.

CO_2-bearing melts represent the chief agents for the mobilization of carbon stored in the Earth's interior, therefore playing a leading role in the deep carbon cycle. Previous experimental studies showed that very low degrees of partial melting of carbonated mantle rocks will produce melts characterized by high dissolved CO_2 (~40 wt%) and low SiO_2 (1-10 wt%) and that the amount of such components will evolve in the opposite directions for higher degrees of partial melting. Noteworthy, this compositional variation is well represented in nature by a clan of SiO^{2-} undersaturated rocks which are carbonatites, kimberlites, lamprophyres and melilitites. Despite their geological relevance, their rheological properties and atomic structure at P-T conditions relevant for their formation remain almost unknown, hindering their migration through the upper mantle to be modeled.

In our study, the starting materials were both synthetic glasses and powdered rocks with variable CO_2 (38-3.5 wt%) and SiO_2 (0-36 wt%)contents, in order to have a complete spectrum of analogues representative of carbonatitic, kimberlitic and melilititic melts and be able to investigate the role of SiO_2 and CO_2 on the rheological properties of

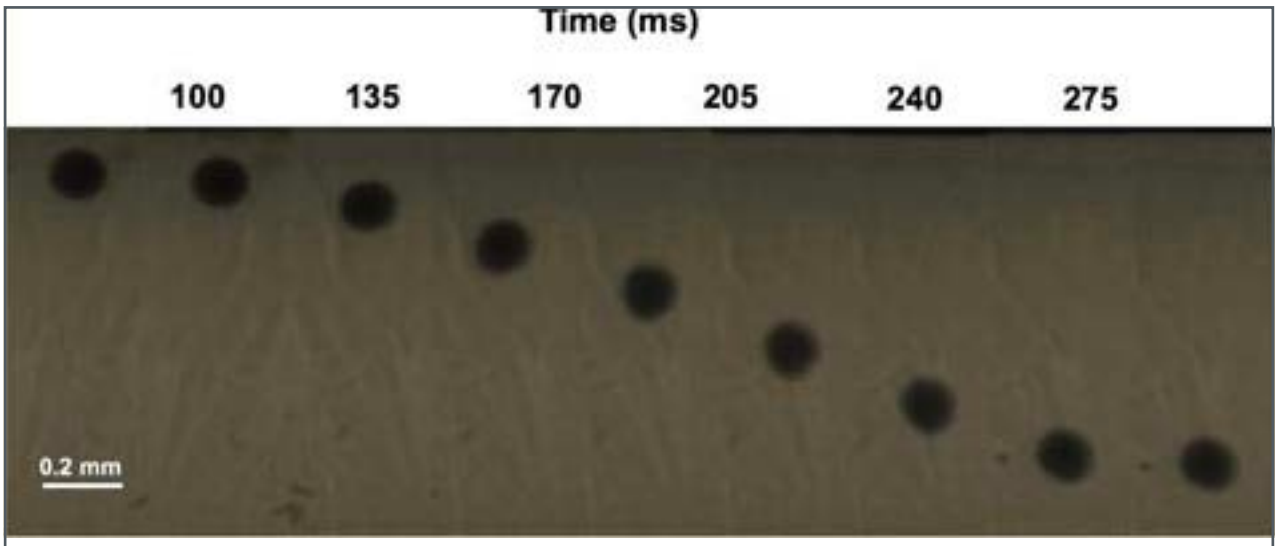

Fig. 1 I X-ray radiography images showing the descent of the Pt sphere in synthetic carbonate-silicate melt as function of time for a viscosity measurement performed at the Advanced Photon Source of the Argonne National Laboratory (Argonne, IL, USA).

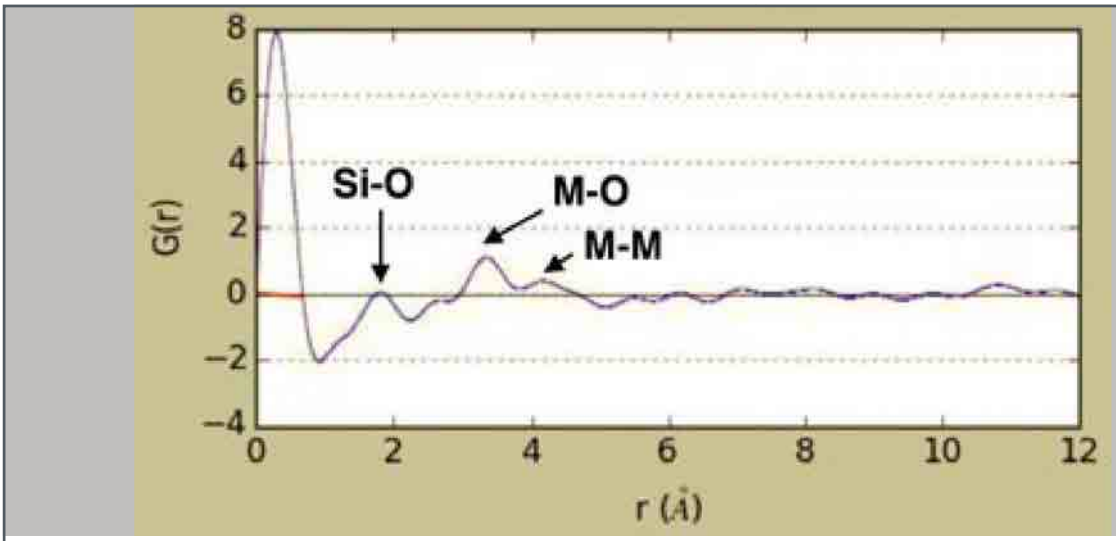

Fig.2 I Reduced pair distribution function G(r) of a carbonate-silicate melt investigated in our study using the multi-angle energy dispersive X-ray diffraction technique at 2.5GPa/1865°C.

magmas in nature. The viscosity and melt structure measurements were carried out at high pressure and temperature using the Paris-Edinburgh press available at the Advanced Photon Source in combination with in-situ X-ray synchrotron radiation (Argonne, IL, USA).A high-speed camera (500 frame per second, f.p.s.) allowed us to determine the viscosity though the Stokes' equation using the recorded velocity of the Pt falling sphere. Melt structure measurements were performed by multi-angle energy dispersive X-ray diffraction at HP-HT. This technique allows the interatomic distances to be measured as shown in Figure 2 where Si-O, M-O and M-M distances are reported (M = Ca, Mg, Fe).

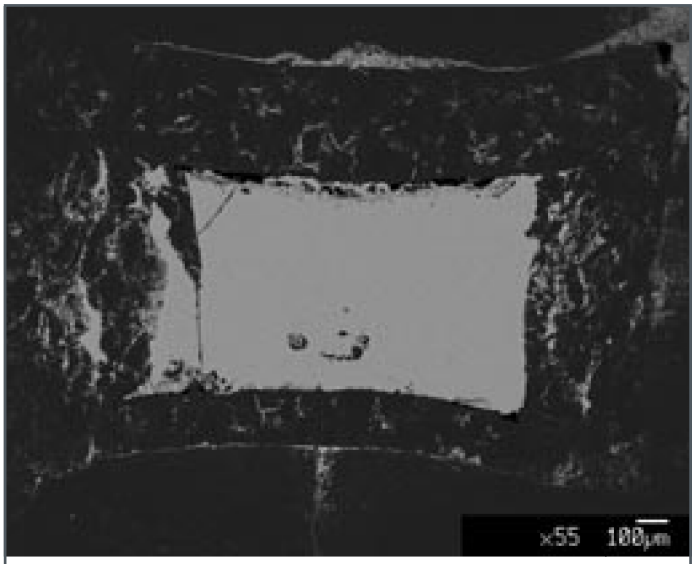

Fig. 3 I Back-scattered electron image of a homogeneous quenched carbonate-silicate glass investigated at 1.3GPa/1815°C recovered after viscosity and melt structure measurements.

The recovered quenched products from in-situ measurements were, then, analysed with the JEOL JXA-8200 electron microprobe (INGV) to investigate their texture, chemical composition and crystallized crystalline phases (Figure 3).

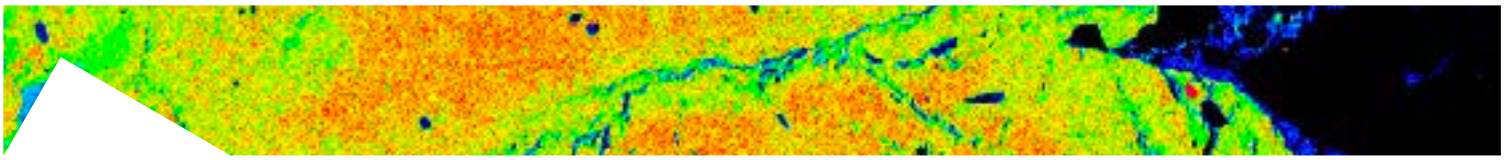

Our results show viscosity of less than 0.01 Pa·s for our SiO_2-free composition that increases up to two orders of magnitude as we add more SiO_2 up to~36 wt% as consequence of the its polymerizing effect. Our measured viscosities along with a modeled variation of density contrast (rocks density-melt density) in the upper mantle results in melt mobility ranging from ~150 $g \cdot cm^{-3} \cdot Pa^{-1} \cdot s^{-1}$ to ~1 $g \cdot cm^{-3} \cdot Pa^{-1} \cdot s^{-1}$ for the SiO_2-free and SiO_2-bearing melts respectively, calculated at a depth of 50-180 km.

Rates of Magmatic Processes recorded in Clinopyroxene Megacrysts at Stromboli

Ubide T., Mollo S., Caulfield J., Brandt C., Bussweiler Y., di Stefano F., Nazzari M., Scarlato P.

The magmatic architecture and physicochemical processes inside volcanoes influence the style and timescale of eruptions. An outstanding challenge in volcanology is to establish the rates and volumes of events that successfully trigger volcanic activity, in contrast with background processes that fail to tip the system to erupt. Magma feeder systems are remarkably crystal-rich, and

the growth stratigraphy of minerals sampled by erupted magmas can reveal a wealth of pre-eruptive processes. Here we combine detailed textural and chemical data on large (> 5mm), euhedral titanaugite megacrysts from the Roman era activity at Stromboli (Pizzo scoria cone, 2.4-1.8 ka) to investigate the volcano plumbing system prior to the onset of the current steady-state regime. Our dataset includes electron microprobe and laser ablation mass spectrometry maps, which visualise major and trace element zoning across entire megacryst sections. The clinopyroxene data are complemented with geochemical constraints on mineral and melt inclusions throughout the megacrysts, and on the glassy host tephra. Megacrysts include core, mantle and rim compositional regions. All regions are both sector and oscillatory zoned, yet their compositions suggest equilibrium crystallisation from relatively similar, shoshonite-buffered melts. Mild sector zoning (Fig. 1) documents dynamic crystallisation, but under conditions of low undercooling, implying slow magma ascent or convection. Refined thermobarometric models return deeper crystallisation depths than those described previously, suggesting deep clinopyroxene-dominated mushes (>10

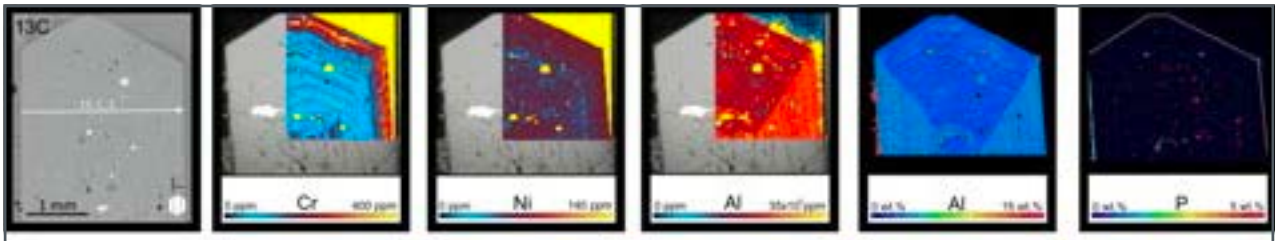

Fig.1 I Elongated section of a clinopyroxene megacryst from Stromboli, cut along the c-axis (section 13C). The section was imaged under reflected light (left panel; the white arrow indicates the location of an electron microprobe transect), and chemically using LA-ICP-MS (middle panels: Cr, Ni, Al) and electron microprobe at INGV-Rome (right panels: Al, P). Reflected light and electron microprobe images provide detailed information on inclusion populations and sector zoning, whereas LA-ICP-MS maps unveil chemical complexity along concentric zones at trace element levels.

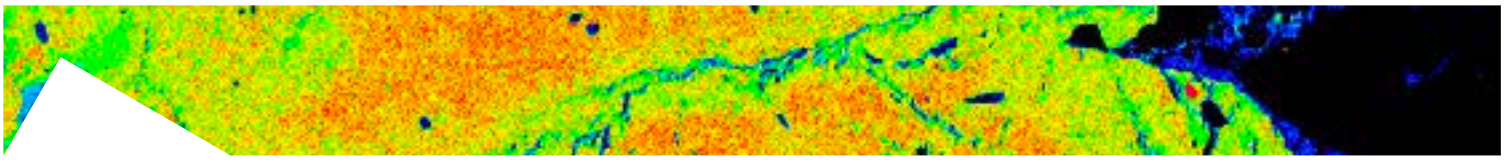

km), similar to other water-rich, alkaline mafic systems. Megacryst cores are overgrown by oscillatory zoned mantles that record continuous input of magma that did not lead to eruption. Conversely, the same crystals show a final rim characterised by a mild increase in compatible transition metals Cr and Ni (Fig. 1), and depletion in incompatible rare earth elements, suggesting pre-eruptive mafic replenishment and magma mixing. The volcanic system may have been characterised by long (centennial) periods of repose and crystal residence, punctuated by rapid (days-weeks) mush evacuation and eruption upon the arrival of new shoshonitic magma. Since the inception of the current steady-state activity, eruption-triggering melts have become significantly more mafic (Mg-rich), suggesting the intrusion of primitive magma may be a key driver of the current steady-state regime.

Paleomagnetism

Winkler A., Nazzari M., Caricchi C.

The INGV paleomagnetism laboratory has been involved for several years in the study of the magnetic properties of fine dust related to atmospheric pollution, accumulated in leaves, lichens or PM10 filters.

Recently, the magnetic characterizations have been combined with morphoscopic analyses carried out at the HP-HT laboratory, using the JEOL JSM-6500F FESEM (updated to series 7000), equipped with backscattering electron detector and EDS JEOL HYPERNINE, 133 eV for the chemical microanalysis.

The magnetic analyses were carried out by Aldo Winkler and Chiara Caricchi, assisted, for electron microscopy, by Manuela Nazzari.

The analyzed samples were lichens taken from Via di Salone, Rome, in an area heavily involved by multiple sources of air pollution. In particular, the lichens were supplied by ARPA Lazio for biomonitoring the pollutants linked to the activity of fraudulent fires for recovering metals from waste electrical and electronic equipment.

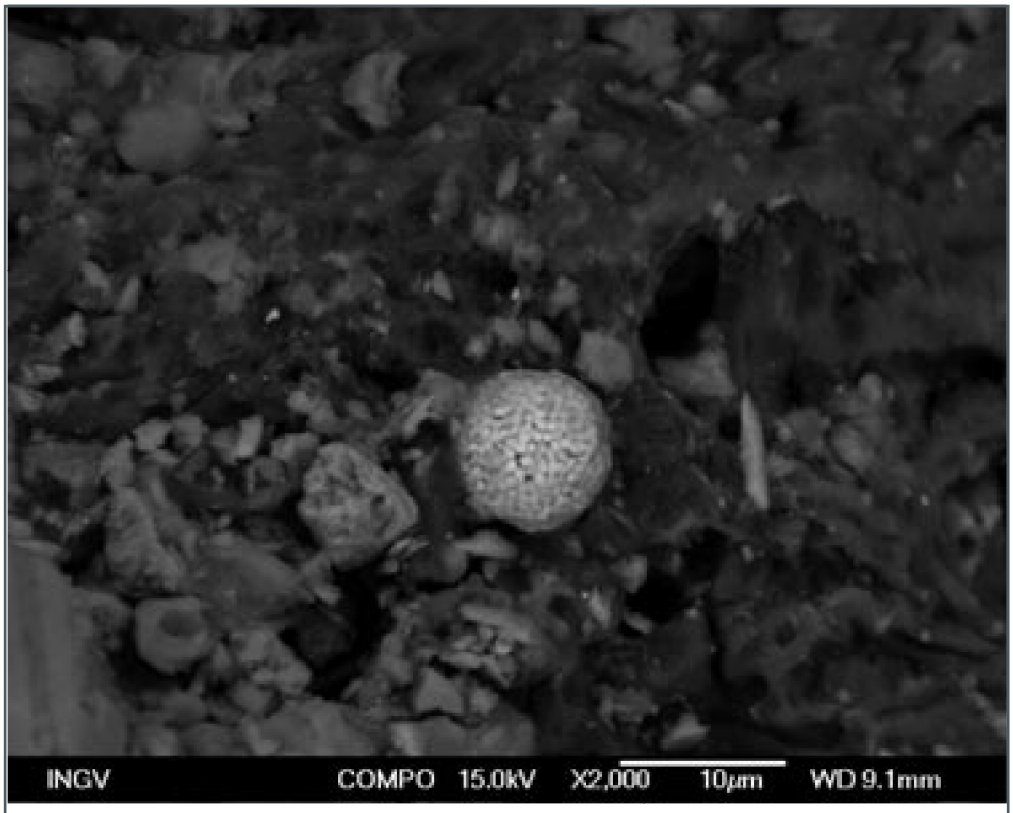

Fig.1 I Spectacular image of a spheroidal grain of magnetite, apparently framboidal, smaller than 10 µm, incorporated in the lichen matrix.

Morphoscopic and magnetic properties agreed, highlighting the widespread presence of metal particulates embedded in the lichen structures and presumably, due

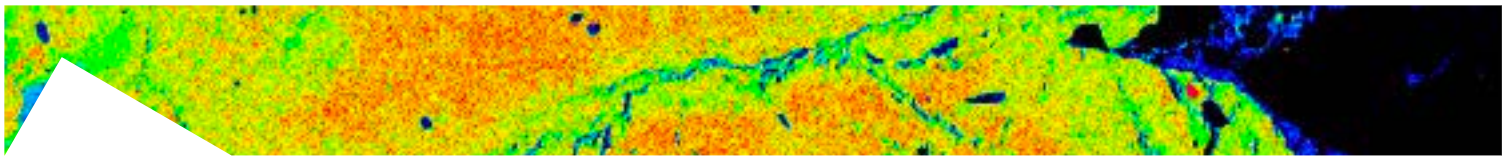

to their shape and composition, arising from anthropogenic combustions and abrasion processes; traffic, industrial and arson activities are probably the joint sources of these particles.

The preliminary results of these activities were presented at two congresses:

A paper will follow, to be included in the scientific results of the FISR 2016 project “New insights on the biomagnetic monitoring of air pollution: applications to selected environmental contexts in Central Italy“

Geochemical characterization of tephra produced during volcanic eruptions from the Neapolitan Area

Di Vito M.A., Arienzo I., Nazzari M.

In the framework of the Avellino project, major elements and Cl contents of glass shards from several cores from the South Lazio area, have been analyzed by electron microprobe (EMP) at the Istituto Nazionale di Geofisica e Vulcanologia (INGV), in Rome (Fig. 1).

This study is aimed at better defining the dispersion of the products extruded during volcanic eruptions occurred at Campi Flegrei caldera and Vesuvius volcanoes in the last 4ka, and their possible effects on the environment. Based on the sedimentological features of the deposits, and on the occurrence, in several localities, of two superposed, separated tephra layers, the deposits were correlated to the Avellino and AP eruptions (Mt. Somma-Vesuvius). However, elaboration of EMPA results allowed us to realize that the glasses composition is variable from phonotephrite to phonolite

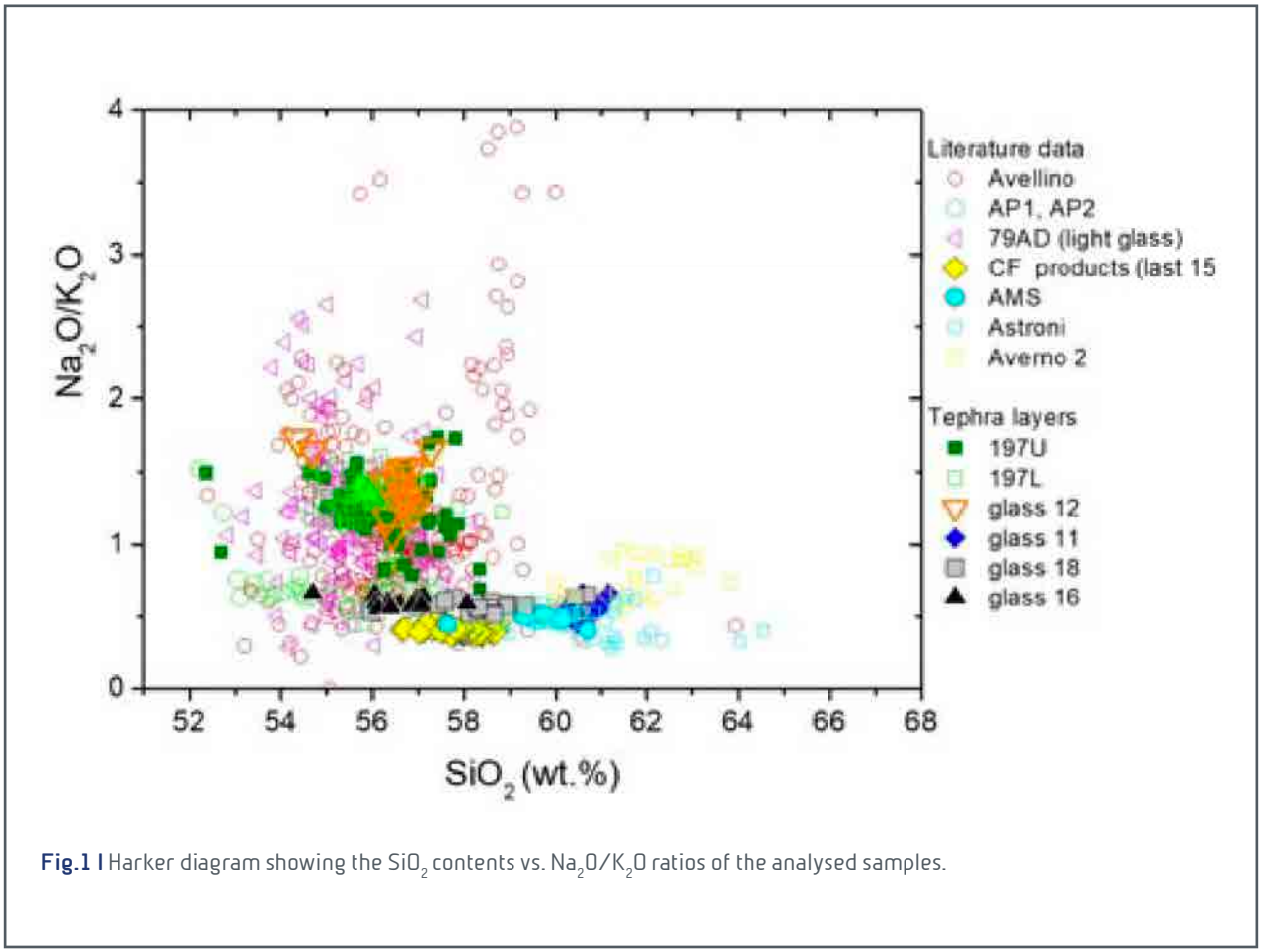

Fig.1 I Harker diagram showing the SiO_2 contents vs. Na_2O/K_2O ratios of the analysed samples.

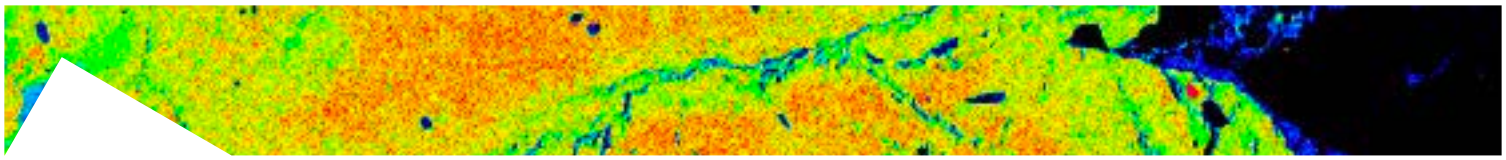

and trachyte, and that major and minor oxide contents, including Cl, point to the occurrence of three tephra layers in the investigated area. The oldest tephra is attributed to the Agnano Monte Spina Plinian (AMS) eruption (Campi Flegrei). This tephra lies below the Avellino tephra in some of the cored sequences. In other cores, the Avellino tephra underlies tephra from the AP1-AP2 eruptions.

Radiocarbon dating, together with the comparison among the obtained chemical compositions and literature data on volcanics from the Neapolitan volcanoes, will allow to better constrain the origin of the investigated products.

8.2 ROCK PHYSICS AND EARTHQUAKES

Chemical and textural analyses of fault-rock samples from the extensional Monte Morrone Fault, central Apennines

Coppola M., Billi A., Nazzari M., Stagno V.

The Mt. Morrone Fault is a potentially-seismic normal fault of central Apennines bordering, to the east, the Sulmona Plain. The study has focused on an exposed fault segment of about 25 m near the Roccacasale village. The Mt. Morrone Fault is exposed along a NW-SE striking and SW-dipping (50°-55°) carbonate-hosted fault surface, which juxtaposes the Quaternary continental gravelly-sandy sediments filling the Sulmona Basin at the hangingwall on the Meso-Cenozoic carbonate platform-to-basin dolomitic limestones and dolostones at the footwall. Eight circular thin sections were obtained from the hand specimens collected on the fault surface of the Mt. Morrone Fault during the structural geological field survey. Microstructural observations performed through optical microscopy showed that the Mt. Morrone Fault is characterized by a proximal fault and a distal fault core with respect to the principal fault surface. The proximal fault core

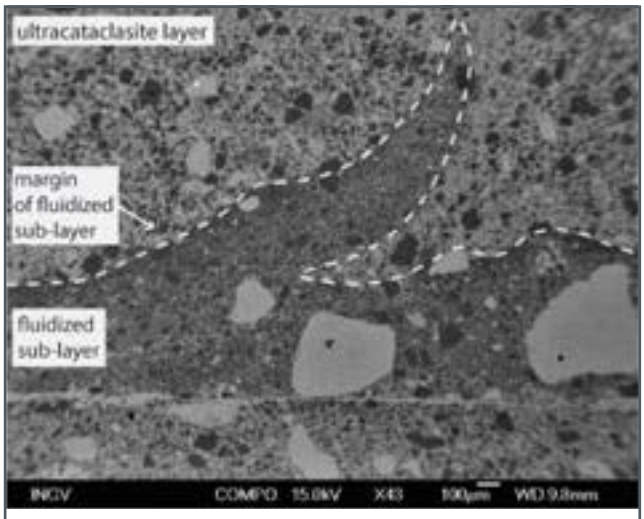

Fig. 1 I The fluidized sub-layer extends along a ultracataclasite layer intruding into it with a cusped shape.

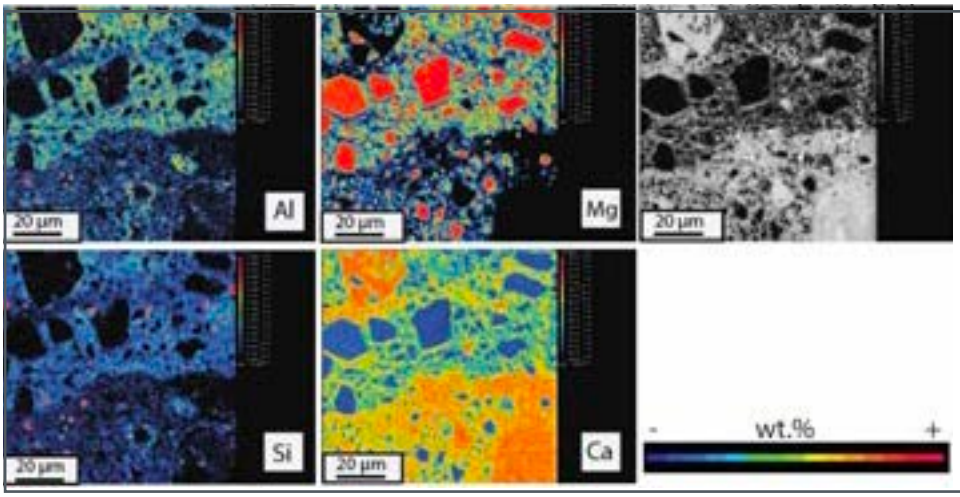

Fig. 2 I Contact between the fluidized sub-layer and a underlying ultracataclasite layer. The fluidized sub-layer contains clasts with a high content of MgO (in red), a matrix with a high CaO content (in yellow) and a low content of Al_2O_3 (in green) and SiO_2 (in blue) in the matrix.

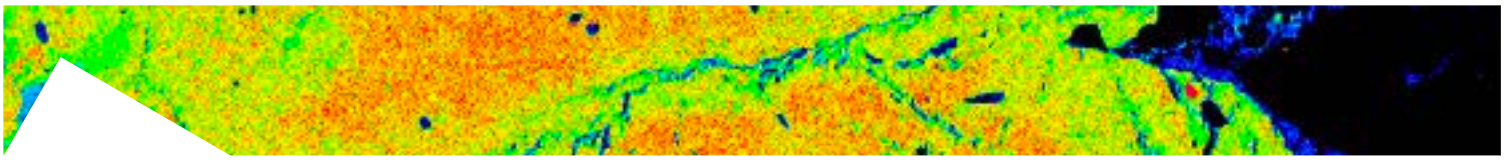

is composed by ultracataclasite layers whereas the distal fault core consists of red and white bands of fluid-plastic cataclasite. To better constrain the micro- and nano-structures and the chemical composition of the fault core of the Mt. Morrone Fault, fault rocks were investigated using laboratory instruments. High-resolution imaging and micro- and nano-structural observations were carried out through the JEOL JSM-6500F Field Emission Scanning (FE-SEM), while quantitative chemical analyses were performed with the Jeol JXA 8200 SuperProbe Electron Probe MicroAnalyzer (EPMA). Both devices are available at the HPHT Laboratory of INGV in Rome.

The textural analyses of the fault rocks as observed through the FE-SEM reveal that the ultracataclasite layers (proximal fault core) are composed by an ultra-fine-grained matrix containing dolomite and calcite clasts (c. 10-100 µm size). A red fluidized sub-layer extends along an ultracataclasite layer spreading into it with flame-like structures (Fig. 1). In the distal fault core, white cataclasite bands consist of a uniform ultrafine-grained calcite matrix, with the red bands showing a granular matrix composed by calcite spheres with a diameter of ~2-5 µm.

The quantitative chemical analyses performed by the EPMA assisted by elemental mapping allow a better understanding of the chemical composition of the ultrafine-grained matrix of the fluidized sub-layer (proximal fault core) and of the red granular bands (distal fault core). The matrix contains high MgO content (~20 wt.%) in the clasts, high CaO content (~57 wt.%) in the matrix and SiO2 and Al2O3 (1-2 wt.%) in the fluidized matrix (Fig. 2). The chemical analyses of the matrix of the granular bands (distal fault core) reveal a high content of CaO (ranging between 25 wt.% and 57 wt.%) and an alumo-silicate content (~5-22 wt.%), which is higher with respect to the fluidized sub-layer alumo-silicate matrix of the proximal fault core.

Results from this study will shed light on the role of major and trace elements as tracers of reactivation of faults in presence of circulating fluids.

Linking THMC processes to the earthquake energy budget: experimental deformation of smectite-rich gouges

Aretusini S., Spagnuolo E., Di Toro G.

Ca-montmorillonite is a common clay mineral (smectite) composing fault cores of shallow megathrusts faults (e.g., Japan Trench) and plate boundary mature faults (e.g., San Andreas). The shear strength evolution of smectites at seismic slip rates controls the propagation of seismic slip, the total coseismic displacement and therefore the magnitude of the earthquake.

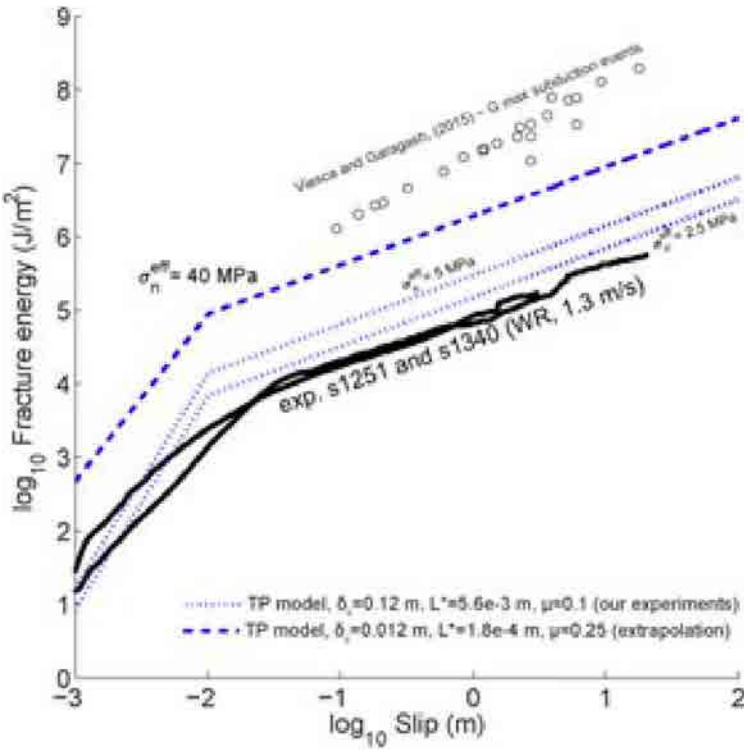

Fig. 1 I Scaling of experimental shear fracture energy *Gf* vs. slip and of seismologic breakdown work G' vs. average seismic slip(R=10), with overlaid *Gf* predicted by thermal pressurization in experiments (R=0.047, dotted line) and extrapolated to 10 km depth (R=0.0093 dashed line).

To investigate the deformation processes controlling fault shear strength, we performed experiments with a rotary machine on 2-mm-thick smectite-rich gouge layers (70/30 wt. % Ca-montmorillonite/opal), at 5 MPa normal stress and slip rates of 0.001, 0.01, 0.1, and 1.3 m/s for a total displacement of 3 m. The role of water content was assessed by testing: (1) oven-dried gouges at 150 and 100 °C under vacuum conditions ($<10^{-3}$ mbar) and (2) room-dry gouges under room humidity or water dampened conditions. Permeability ($2 - 4.3 \cdot 10^{-16}$ m^2) of the room-dry gouge layer was measured with the pore pressure oscillation method before the experiments.

Shear strength and transport properties were included in finite elements numerical models including Thermo-Hydro-Mechano-Chemical processes :thermal pressurization of pore water and thermochemical pressurization from dehydration

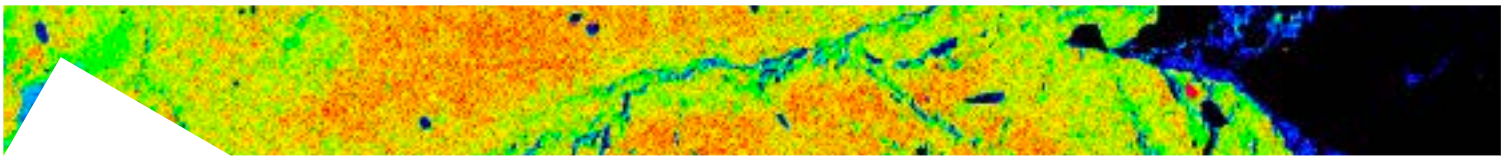

and dehydroxylation of smectite and opal-CT to quartz reaction.

Modelling results show that the combined effects of the frictional heating, the compressibility of pore water and the transport properties of the gouge layer promote a nearly adiabatic pressure-temperature-time path (i.e., without pressurization) in the water-depleted cases and pressure increase by thermal pressurization in the water-rich case. In the water-depleted case, extensive dehydration, thermal decomposition and melting are predicted; instead, under water-rich conditions, no breakdown reaction is predicted, in accordance with the microstructural observations.

In the experiments performed under water-rich conditions and at seismic slip rates, the scaling of frictional shear fracture energy *Gf* with total slip resembles the scaling of seismologic breakdown work G' with average slip for large megathrust earthquakes. This similarity suggests that dynamic weakening is controlled by thermal pressurization in both our experiments and natural large megathrust earthquakes, but with diverse characteristic distances ratio $R = L^*/\delta_c$ (Figure 1).

High resolution tephrostratigraphy and radiocarbon chronology of the lacustrine sequence from the Fucino Basin for future paleoseismological application in Central Apennines (Italy)

Del Carlo P., Smedile A., Di Roberto A.

We propose to use tephrochronology as a key tool to date and synchronize paleoseismological archives, using the mid- to distal-tephra layers from Italian volcanoes within a multi-disciplinary (sedimentology, stratigraphy, geochemistry of sediment, paleomagnetic investigations) high-resolution research project on the Fucino Basin sediment record. In particular, we propose: 1) to study the uppermost part of the record which spans the Late Glacial period (the last ca. 30-35 ka) containing visible and non-visible primary tephra, 2) to identify and characterize these tephra in detail for their texture, mineralogy and geochemistry and 3) to correlate them to a proximal dated volcanic source eruption and thus to transfer the age information to the studied sequence.

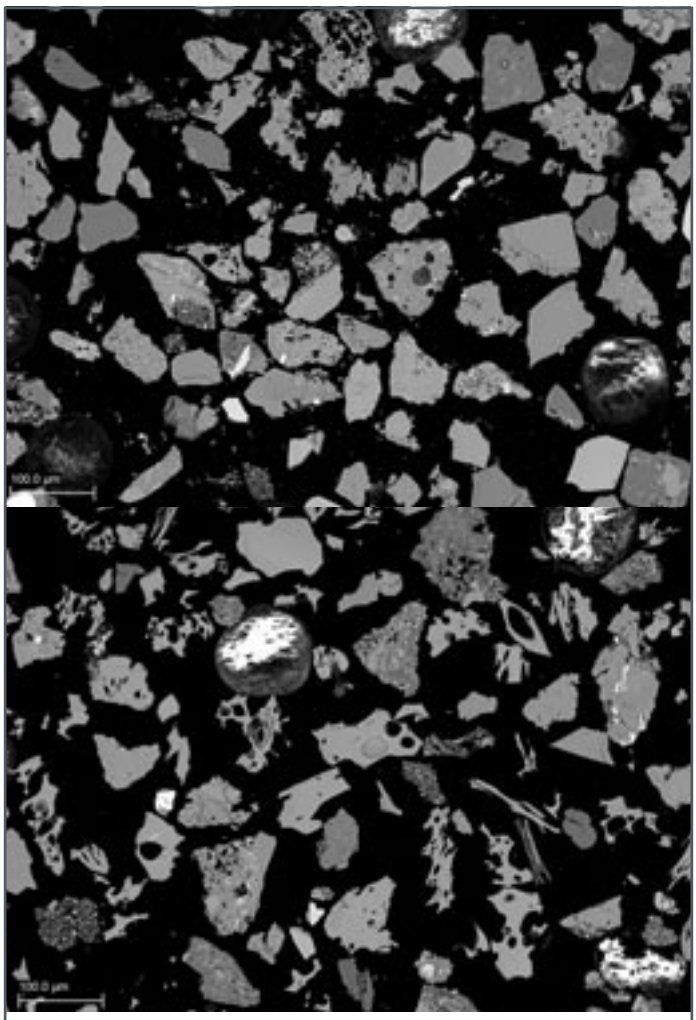

Fig. 1 I Back scattered electron (BSE) images showing some of the studied tephra sampled in FUC-S2 core (Fucino Plain).

This objective will be achieved through the study of core FUC-S2 consisting of a 5.20 m-long sediment sequence, recovered in the Fucino Plain. This sequence might contain several tephra and cryptotephra from the eruptions of peri-Tyrrhenian volcanoes which have been extremely active in Holocene-late Pleistocene. The results of this study will be of great importance also in view of the paleoseismological trenches that will be excavated in 2019 in the Castelluccio di

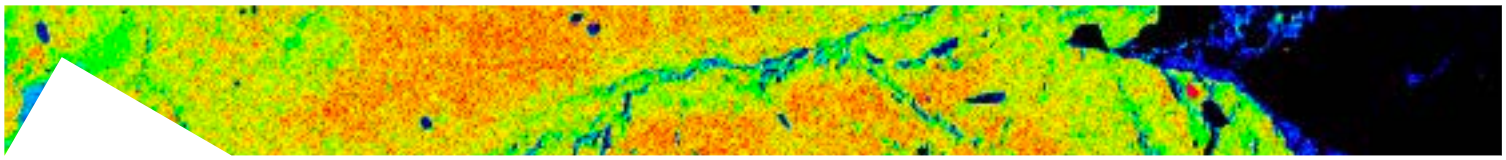

Norcia Plain by INGV researchers. In fact, if tephra layers were identified in the Castelluccio di Norcia sequences, then it would be an incredible opportunity to synchronize Fucino Basin and Castelluccio di Norcia Plain records and temporally constrain past surface faulting events in order to better characterize the seismogenic behaviour of Mt. Vettore-Mt. Bove and Norcia Fault Systems, recently involved in the 2016-2017 Amatrice-Norcia-Visso seismic sequence.

To this aim, we have started to analyze chemical composition of some tephra and cryptotephra layers recovered from the FUC-S2 core at microprobe facilities at HTHPLab INGV Rome. This work is still in progress and results will be available within this year.

Friction of Mineralogically Controlled Serpentinites and Implications for Fault Weakness

Tesei T., Harbord C.W.A., De Paola N., Collettini C., Viti C.

Serpentines are common minerals in several major tectonic faults in a variety of geodynamic settings and have variable frictional strength and complex deformation processes. Here we present friction experiments carried out on a suite of serpentine samples that include veins of antigorite, lizardite, and fibrous serpentine (chrysotile and polygonal serpentine) together with massive samples of retrograde (lizardite and chrysotile rich) and prograde (antigorite-rich) serpentinites. These samples were characterized from the hand specimen down to the nanoscale to precisely constrain their mineralogical composition and are interpreted to represent typical fault rocks and host rocks in serpentine-bearing shear zones, respectively. Experiments were performed at effective normal stress from 5 to 120 MPa, at temperatures of 25°C and

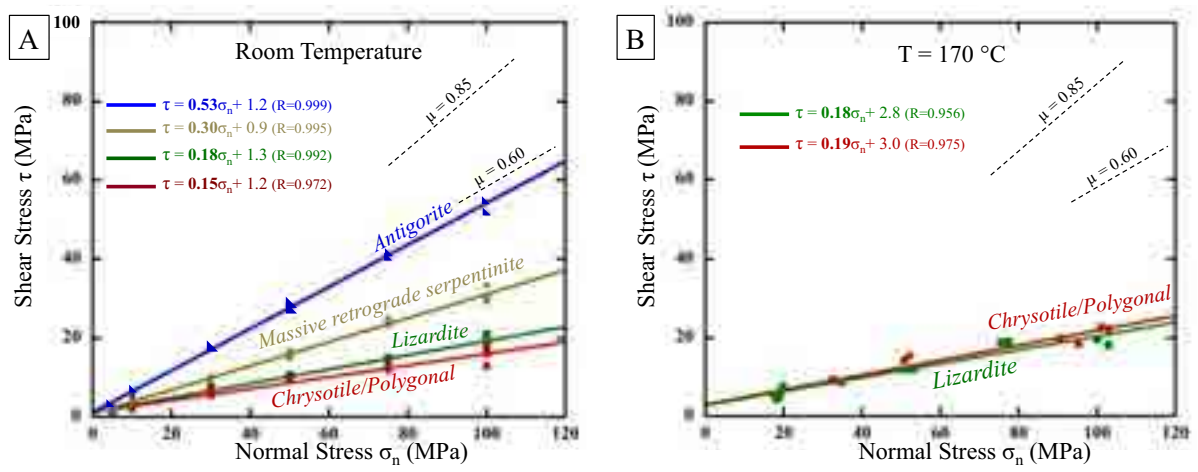

Fig. 1 I Coulomb failure envelopes of serpentine samples tested in this study. Shear stress was measured during steady state sliding phase within each friction experiment. The slope of the linear best fit represent the average coefficient of friction and the y intercept represents the cohesion. Typical friction of crustal rocks is shown for comparison (dashed lines). (a) Envelopes derived from room temperature experiments on antigorite (blue), massive retrograde serpentinite (brown), and fault-related veins lizardite (green) and chrysotile/polygonal serpentine (fibrous serpentines, red). The results of antigorite gouges represent both vein and massive samples together (see text for further explanation). (b) Envelopes for experiments carried out at T = 170°C on lizardite (green) and chrysotile/polygonal serpentine (fibrous serpentines, red) samples.

170°C and water-saturated, that is, under the faulting conditions of the brittle upper lithosphere. Friction of antigorite samples, either massive or vein, is relatively high μ = 0.53. Retrograde, massive serpentinites, constituted primarily of lizardite and fibrous serpentines, are frictionally weak, μ = 0.30. End-members lizardite and fibrous serpentines are even

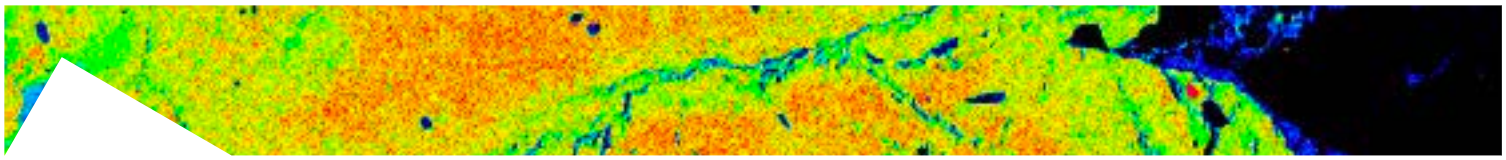

weaker, $0.15 < \mu < 0.19$, and this weakness is unchanged at high temperature. When combined with frictional reactivation analysis, our data provide mechanical evidence for fault weakness inferred from earthquake dip distributions at oceanic outer rises and low-angle normal faults beneath rifted continental margins and at slow/ultraslow spreading mid-ocean ridges.

The role of shear fabric in controlling slip velocity function and breakdown work during laboratory slow slip

Tinti. E., Scuderi M.M., Collettini C., Cocco M.

In this study, we analyze slow-slip events obtained during laboratory experiments at the stability boundary (k~kc) by matching the critical fault rheological stiffness (kc) with a decreased machine stiffness (k). To discern the role of shear localization during fault weakening we simulated fault gouges using quartz powders and a mixture of anhydrite and dolomite, which have a strong rheological contrast. For both lithologies, slow-slip events have typical friction drop of ~0.01 and duration between 6s and 12s. During each event we observe that peak slip velocity is attained before reaching the minimum shear stress, and most of the slip velocity evolution is associated with the dynamic weakening phase.

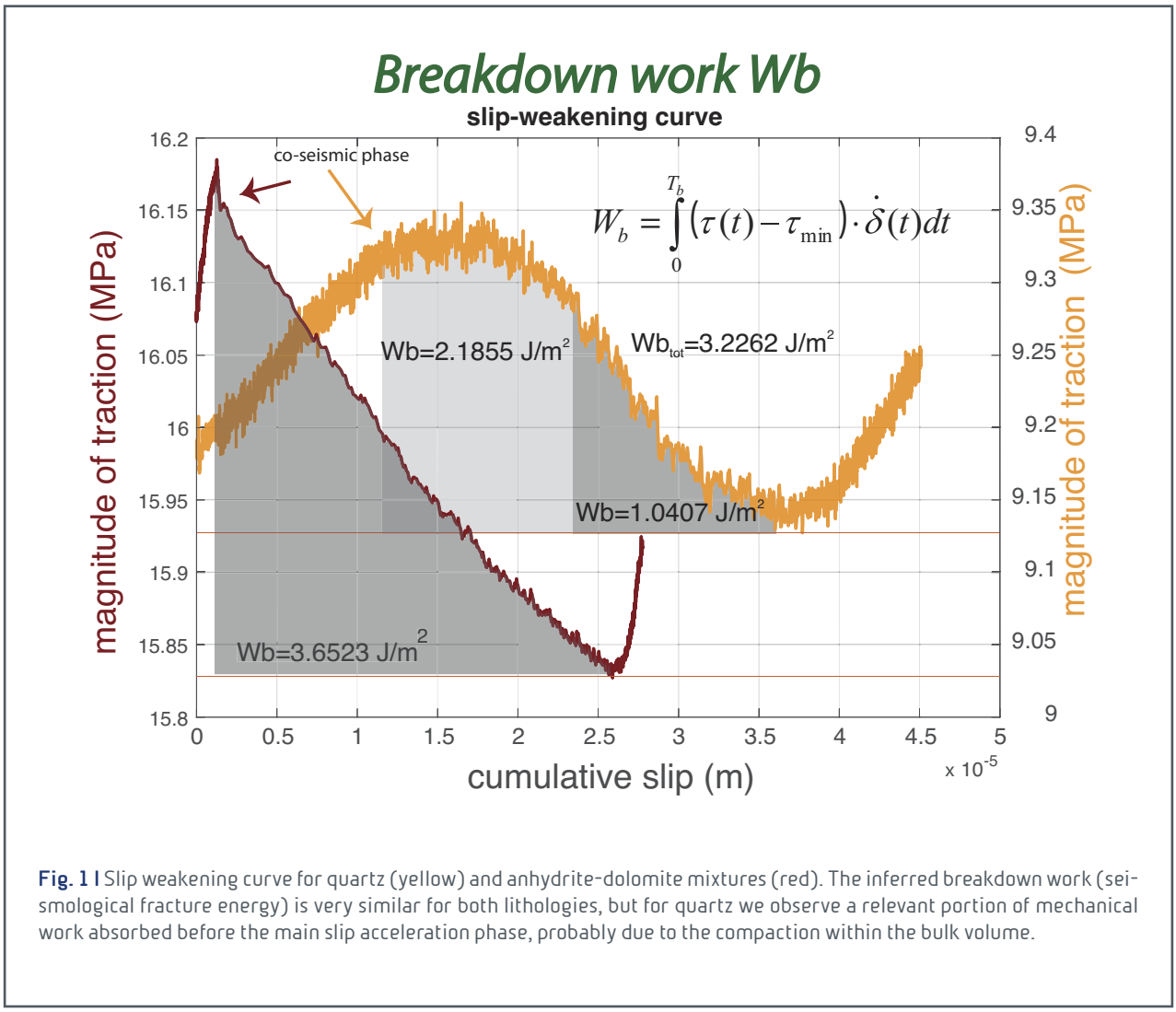

Fig. 1 I Slip weakening curve for quartz (yellow) and anhydrite-dolomite mixtures (red). The inferred breakdown work (seismological fracture energy) is very similar for both lithologies, but for quartz we observe a relevant portion of mechanical work absorbed before the main slip acceleration phase, probably due to the compaction within the bulk volume.

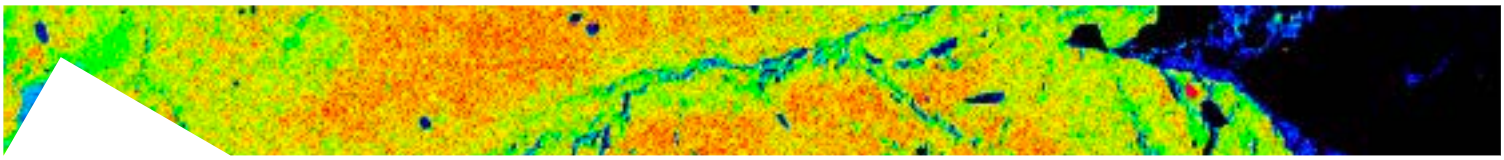

We document that the fault zone fabric controls the slip velocity function as well as the details of micro-mechanical deformation (i.e. dilation/compaction). For quartz gouge, shear deformation localizes along continuous and sharp (~1µm thick) shear planes resulting in a smooth slip velocity function (similar to a Gaussian) where a clear pre-seismic slip is easily detectable. In the anhydrite and dolomite mixture, shear localizes along thick boundary shear planes interconnected by a P-foliation, resulting in a more distributed deformation, showing a Yoffe slip velocity having a short acceleration phase (~1s) with no pre-seismic slip and a long deceleration.

The inferred breakdown work (seismological fracture energy) is very similar for both lithologies, but for quartz we observe a relevant portion of mechanical work absorbed before the main slip acceleration phase, probably due to the compaction within the bulk volume.

Our results confirm that the slip rate function contains the key dynamical information to characterize the evolution of dynamic traction. The retrieved differences in the slip velocity functions and mechanical work absorbed in dynamic weakening depend on the strain partitioning within the fault volume.

Frictional Properties of Opalinus Clay: Implicationsfor Nuclear Waste Storage

Orellana L.F., Scuderi M.M., Violay M.

The kaolinite-bearing Opalinus Clay (OPA) is the host rock proposed in Switzerland for disposal of radioactive waste. However, the presence of tectonic faults intersecting the OPA formation put the long-term safety performance of the underground repository into question due to the possibility of earthquakes triggered by fault instability. In this paper, we study the frictional properties of the OPA shale. To do that, we have carried out biaxial direct shear experiments under conditions typical of nuclear waste storage. We have performed velocity steps (1–300 µm/s) and slide-hold-slide tests (1–3,000 s) on simulated fault gouge at different normal stresses (4–30 MPa). To establish the deformation mechanisms, we have analyzed the microstructures of the sheared samples through scanning electron microscopy. Our results show that peak (µpeak) and steady state friction (µss) range from 0.21 to 0.52 and 0.14 to 0.39, respectively, thus suggesting that OPA fault gouges are weak. The velocity dependence of friction indicates a velocity strengthening regime, with the friction rate parameter (a - b) that decreases with normal stress. Finally, the zero healing values imply a lack of restrengthening during interseismic periods. Taken together, if OPA fault reactivates, our experimental evidence favors an aseismic slip behavior, making the nucleation of earthquakes difficult, and long-term weakness, resulting in stable fault creeping over geological times. Based on the results, our study confirms the seismic safety of the OPA formation for a nuclear waste repository.

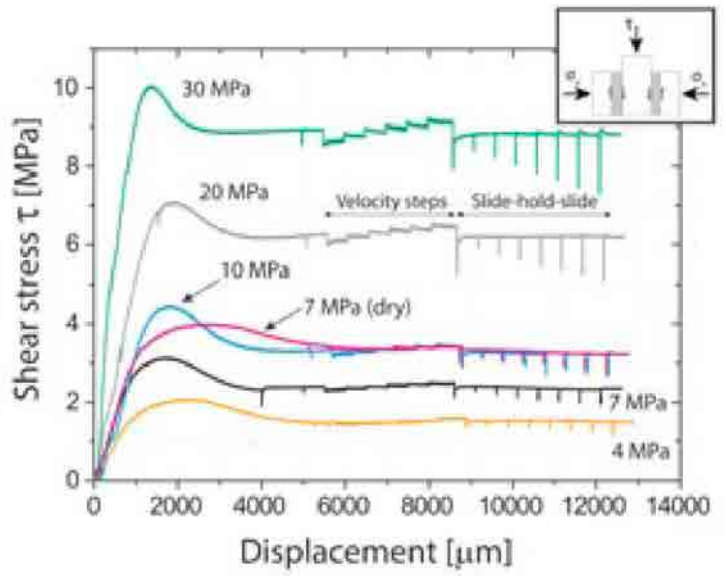

Fig. 1 I Friction experiments performed on simulated gouge samples of Opalinus Clay at different normal stress (from 4 MPa to 30 MPa). The curves show the evolution of the shear stress (τ) with slip. Experiments show a peak strength followed by a residual value. The curves indicate a low to moderate slip weakening. The weakening is higher at lower normal stress (4, 7, and 10 MPa). Velocity step and slide-hold-slide tests start after shear stress reach a steady value. Inset: Double direct shear configuration used in these experiments.

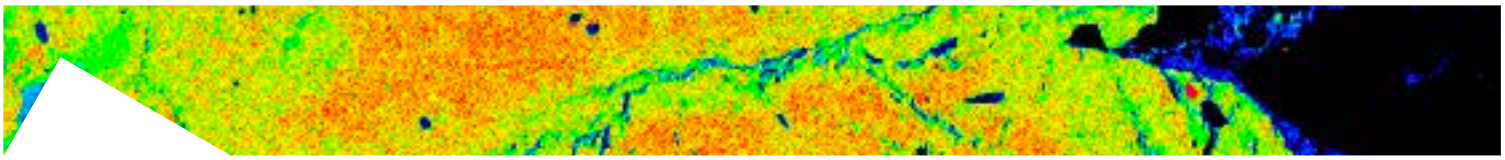

Fluid Injection and the Mechanics of Frictional Stabilityof Shale-Bearing Faults

Scuderi M.M., Collettini C.

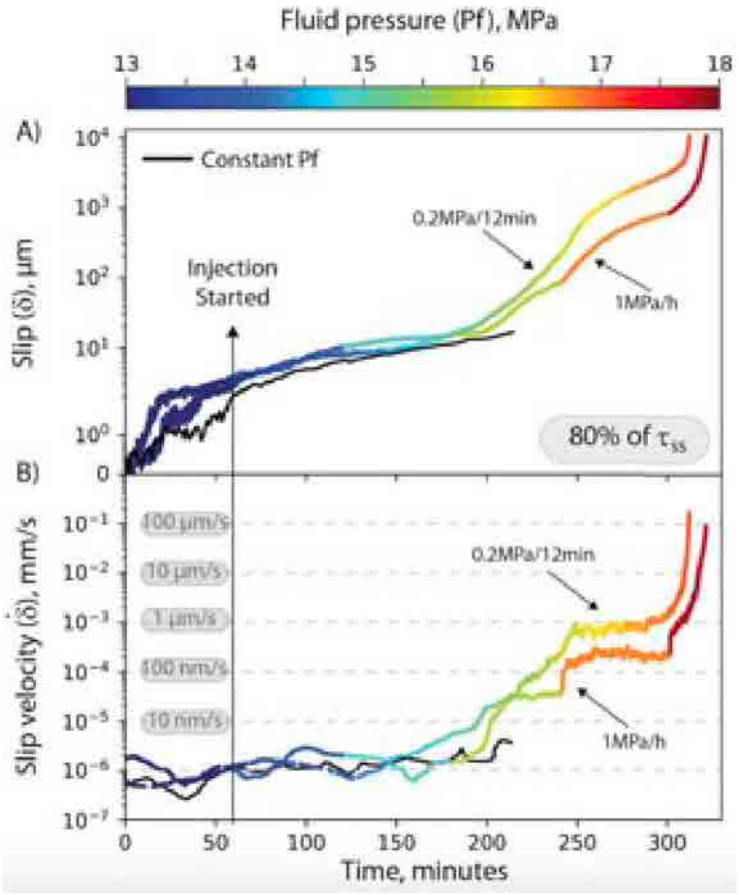

Fig. 1 | Raw data showing the time series of the evolution of fault slip (a) and slip velocity (b) for the experiments performed at 80% of steady state shear stress. The curves are color coded by the applied fluid pressure at the downstream intensifier (injection side). In black is reported the experiment performed at constant fluid pressure.

Fluid overpressure is one of the primary mechanisms for triggering tectonic fault slip and human-induced seismicity. However, upon fault reactivation models of earthquake nucleation suggest that increased fluid pressure should favor stable sliding rather than dynamic failure. Here we describe laboratory experiments on shale fault gouge, conducted in the double direct shear configuration in a true-triaxial machine. To characterize frictional stability and hydrological properties we performed three types of experiments: (1) stable sliding shear experiments to determine the material failure envelope and permeability, (2) velocity step experiments to determine the rate-and-state frictional properties, and (3) creep experiments to study fault slip evolution with increasing pore fluid pressure. The shale gouge shows low frictional strength, $\mu = 0.28$, and permeability, $k \sim 10\text{-}19\ m^2$ together with a velocity strengthening behavior indicative of aseismic slip. During fault pressurization, we document that upon failure slip velocity remains slow (i.e., $v \sim 200\ \mu m/s$), not approaching dynamic slip rates. We relate this fault slip behavior to the interplay between the fault weakening induced by fluid pressurization, the strong rate-strengthening behavior of shales, and the evolution of fault zone structure.

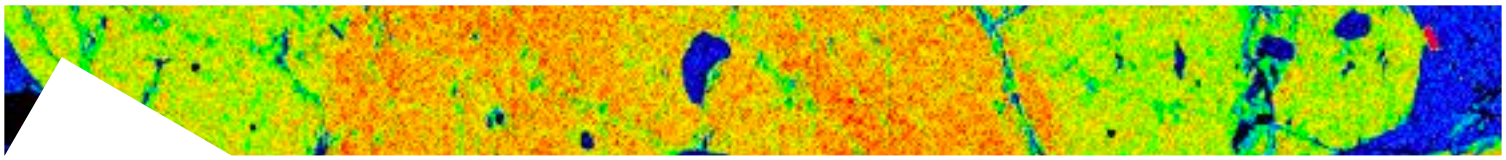

Frictional melting in fluid-rich faults (Bolfin Fault Zone, Chile)

Di Toro G., Fondriest M., Mitchell T., Gomila R., Jensen E., Sommacampagna C., Masoch S., Bistacchi A., Magnarini G., Faulkner D., Cembrano J., Mittempergher S.

Pseudotachylytes (solidified friction melts produced during seismic slip) are currently considered one of the very few geological markers of seismic faulting in exhumed faults (Rowe and Griffith, 2015). Pseudotachylytes are considered to be rare in the geological record because they are typical of particular seismogenic environments characterized by water-deficient cohesive rocks and possibly associated with particular earthquakes with exceptionally large static stress drops. However, experimental evidence suggests that frictional melting may easily occur in the presence of pressurized liquid water. This possibility is supported by (though rare) occurrence of vesiculated and amygdules-rich pseudotachylytes. But even if produced during seismic slip, the delicate pseudotachylyte matrix may alter when permeated by post-seismic fluids and the pseudotachylyte lost from the geological record.

Here we discuss the occurrence of poorly to strongly altered pseudotachylytes hosted in a fluid-rich exhumed fault strand of the Atacama Fault System (Chile, Fig. 1a). The Bolfin Fault Zone (BFZ) is > 30 km long and cuts amphibolites anddioritesof the Coastal Cordillera. The BFZ records a series of deformation and veining events lasting from the Jurassic (under granulitic facies) to the Pliocene (T < 150°C). The pseudotachylytes are associated with a dark green in color, foliated, ultracataclastic to mylonitic fault core~1 m thick which accommodated > 5 km of strike-slip displacement at 6-8 km depth and 280-350°C ambient temperature. The fault core is bounded by an up to 50 m thick damage zone characterized by intense hydrothermal sub-greenschist to greenschist facies alteration. The pseudotachylytes include black to brownish in color cm-thick fault and injection veins, with spectacular flow structures (Fig. 1b-c). The pseudotachylyte consists of suspended clasts of saussiritized feldspar, albite and minor quartz immersed (locally) in a poorly altered and homogenous (glassy-like) feldspathic in composition matrix with tabular microlites of feldspar (Fig. 1d) and (more often) in a strongly altered matrix made oftens of micrometer in size albite, chlorite, and epidote crystals (Fig. 1e). The matrix hosts rounded to ellipsoidal concentric features up to ~1 mm in size with an inner core of chlorite, epidote or calcite and an external rim of quartz (Fig. 1e). These latter

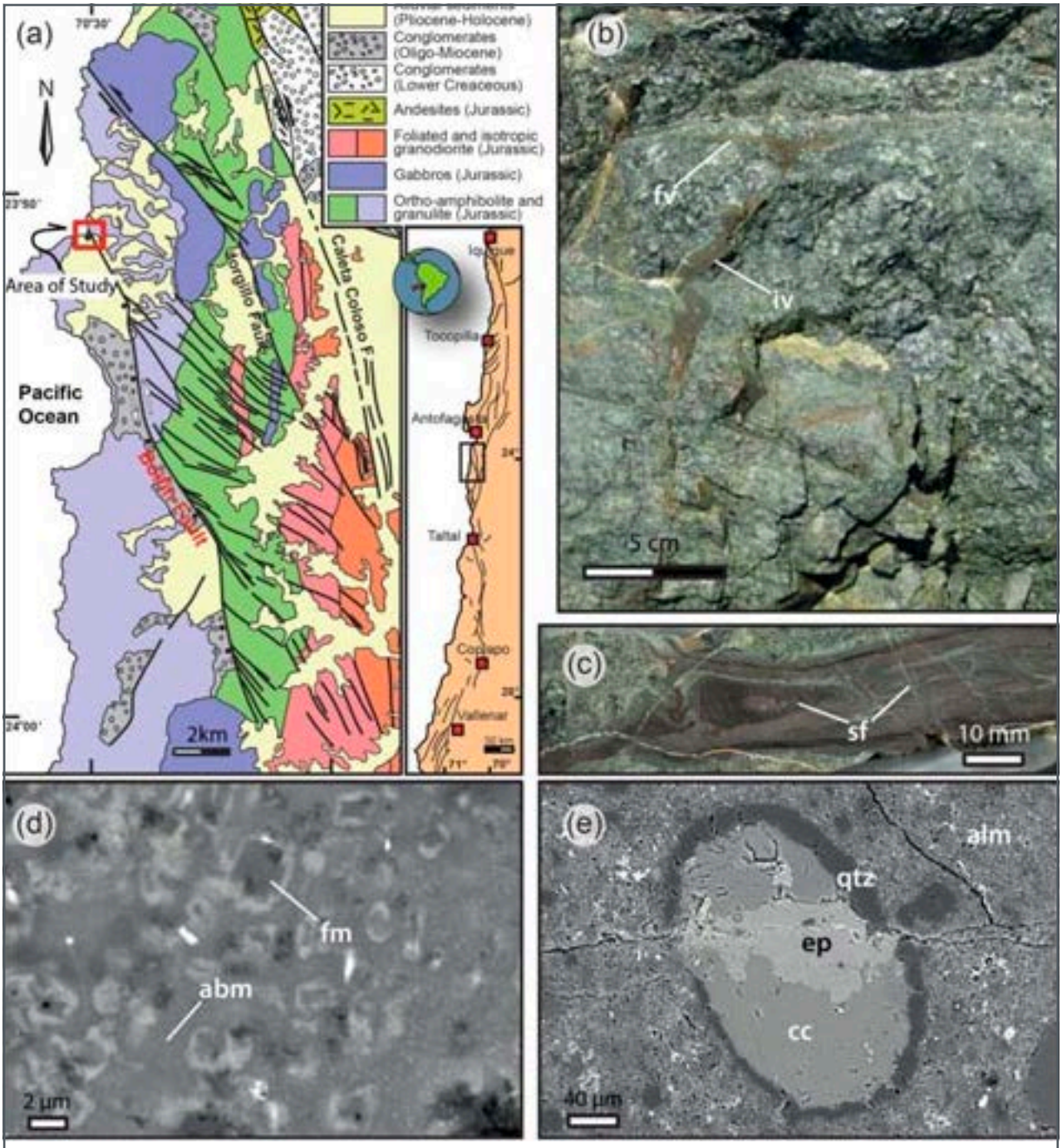

Fig. 1 | The pseudotachylytes of the Bolfin Fault Zone. (a) Geological setting (modified from Cembrano et al. 2005 and Mitchell and Faulkner, 2010). (b) Pseudotachylyte fault (fv) and injection (iv) vein (Playa Escondida locality). (c) Flow structures with sheath fold-like (sf) structures in the pseudotachylyte (polished sample). (d) Tabular feldspar microlites (fm) in the glassy-like altered albitic in composition matrix (abm). (e) Ellipsoidal amygdule with external rim of quartz (qtz) and core of calcite (cc) cut by an epidote-bearing vein (ep). The amygdule is hosted in the strongly hydrothermally altered pseudotachylyte matrix (alm) with a typical sub-greenschist facies assemblage (chlorite, epidote and albite). (d) and (e) are Back Scattered Scanning Electron Microscope images.

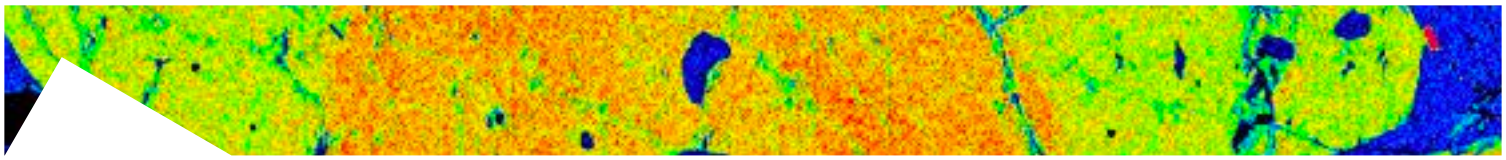

features are interpreted as vesicles filled by post-seismic sub-greenschist facies minerals precipitated from the percolating hydrothermal fluids (i.e., amygdules, Fig. 1e).

The identification of pseudotachylytes, the first so far to our knowledge in South America, and its association with intense pre- and post-seismic alteration challenges the common belief that these fault rocks are rare. Consistent with the experimental evidence, pseudotachylytes (1) could be a common coseismic fault product at intermediate crustal depths, (2) may easily be produced in fluid-rich hydrothermal environments as well as fluid absent conditions but, (3)are easily lost from the geological record because they are prone to alteration.

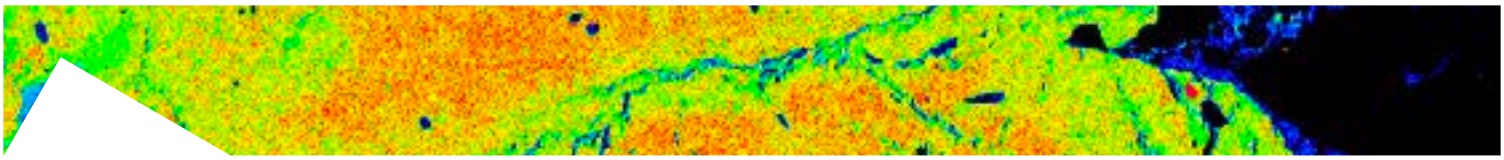

Frictional properties of basalts pressurized with H_2O- and CO_2 – rich fluids for in-situ CO_2 - storage purposes

Giacomel P., Spagnuolo E., Scuderi M., Di Toro G., Collettini C.

Underground injection of pressurized CO_2-charged water into basaltic reservoirs has been proposed as one of the most promising options among the CO_2-storage methods (CarbFix project), as it provides a strikingly fast, long lasting and thermodynamically stable in-situ carbon storage solution.

To move this method from a pilot project to a viable industrial scale that could be applied to subsurface voluminous basaltic occurrences widespread throughout the world, a thorough appraisal of the carbon sequestration potential is pivotal (CarbFix2 project, 2017-2021). Nonetheless, the assessment of this is inseparable from a preliminary rock and fault mechanics characterization, including the role of fluid overpressure, possibly developed during CO_2 sequestration.

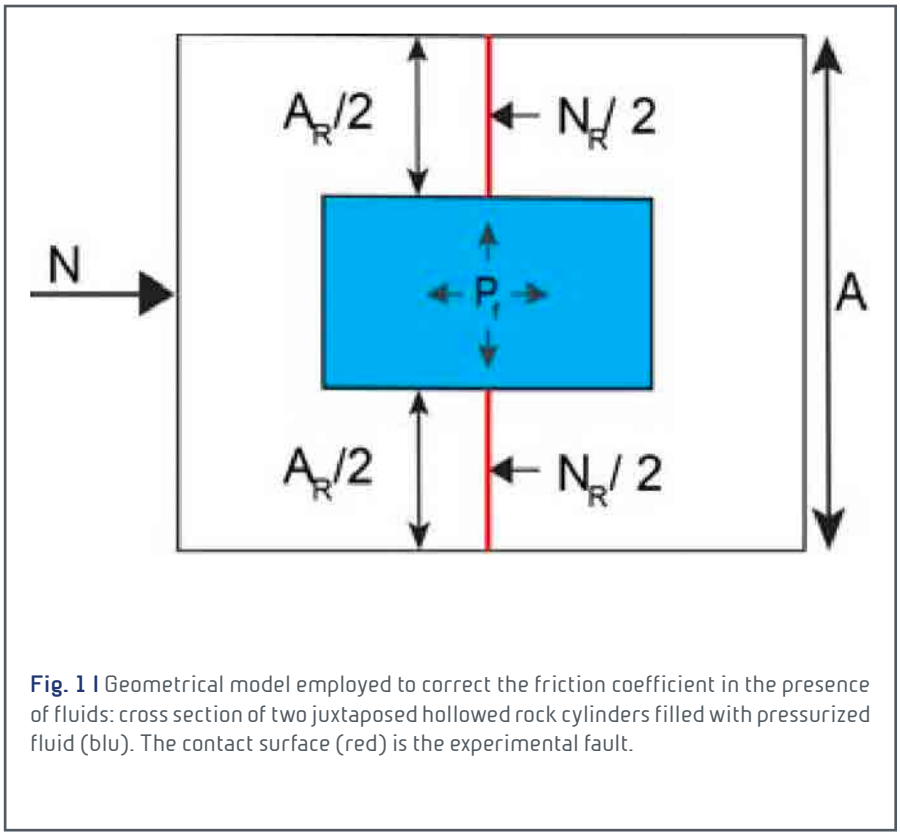

Fig. 1 I Geometrical model employed to correct the friction coefficient in the presence of fluids: cross section of two juxtaposed hollowed rock cylinders filled with pressurized fluid (blu). The contact surface (red) is the experimental fault.

To test the role of fluid pressure in the frictional properties of faults, we have performed friction experiments using the SHIVA rotary shear apparatus (INGV- Rome) at variable fluid factors λ (= fluid pressure, Pf /normal stress, σn). We performed both tests at constant displacement rate of 10 µm/s and creep experiment aimed at inducing the dynamic frictional instability.

The results show that when the correction that accounts for the geometrical model in Fig.1 is applied, the static friction coefficient, µs is ~ 0.61 independently of λ, in accordance with pre-existing literature and the lack of microstructure or

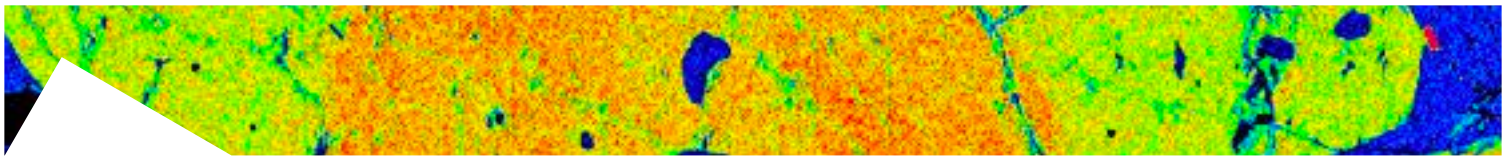

diffuse reaction softening capable of explaining a $\mu s \approx 0.4$ at $\lambda = 0.4$ when such a correction is not employed.

These data lay the ground for a correct data interpretation of the mechanical data in all the rotary-shear apparatuses with SHIVA- like settings and thus a better understanding of the mechanics of faulting in the presence of pressurized fluids.

Fault reactivation in thick fault zones: a laboratory perspective

Giorgetti C., Tesei T., Scuderi M. M., Collettini C.

Laboratory deformation and in particular friction experiments constitute a powerful tool to simulate and study faults' slip behaviour. Furthermore, microstructural observations shed light on the micromechanics and the deformation processes acting during fault deformation.

In particular, we conducted experiments with the apparatus BRAVA, installed in HP-HT Laboratory at the INGV (Rome), to investigate the role of stress field orientation and magnitude on pre-existing fault reactivation. A thorough understanding of the potential for reactivation is a crucial issue in the assessment of seismic hazard. Indeed, pre-existing fault zones constitute planes of weakness that can be reactivated depending on their frictional properties and on the orientation and magnitude of the stress field. Fault reactivation is often analytically predicted and based on the assumption that faults are ideal planar features characterized by constant friction. However, natural faults are complex structures that typically host fault cores of finite thickness consisting of cataclastic rocks. Are these analytical models applicable to gouge-bearing fault rocks?

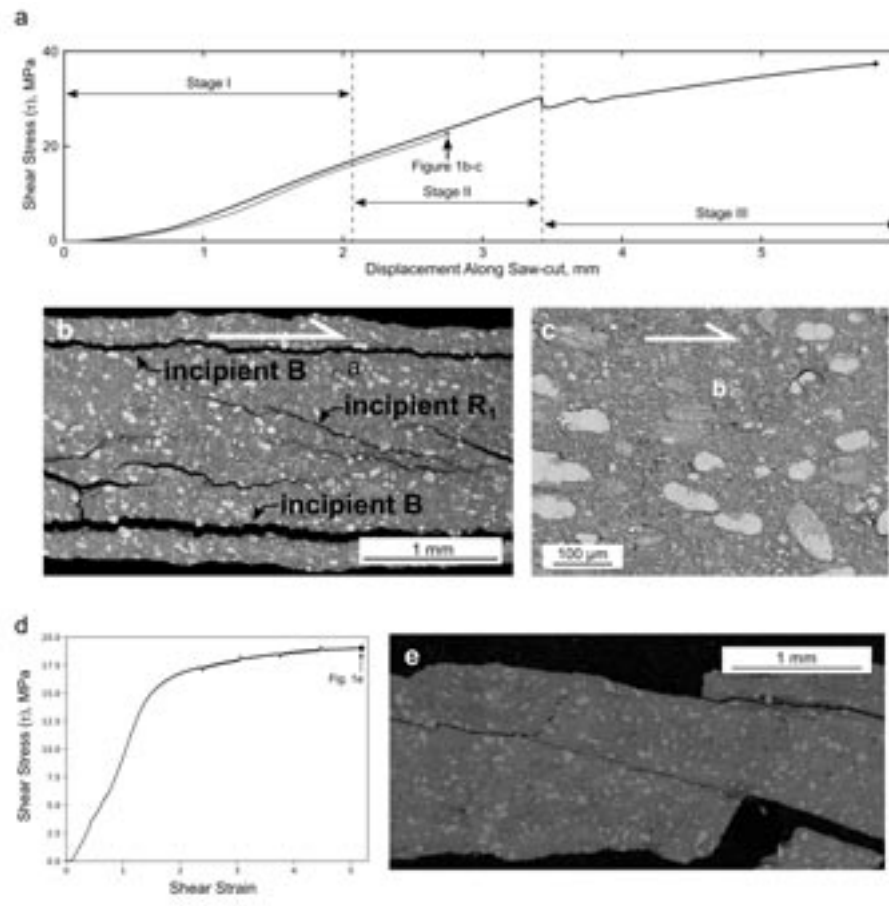

Fig. 1 | SEM micrograph showing microstructures developed in samples deformed under different configurations. (a) Shear stress vs. displacement along saw-cut plot showing at which displacement the microstructures were collected. (b) Microstructure after 2.75 mm of displacement along saw-cut characterized by elongated clasts oriented consistently with the shear direction and incipient boundary and Riedel shears. (c) Detail of microstructure after 2.75 mm of displacement in (b)showing elongated clasts oriented accordingly to the shear direction. (d) Mechanical data of a double direct shear-shear experiment. After the "run-in" phase, the shear stress vs. shear strain evolution curve shows a slightly strain-hardening trend. The gouge sample at shear strain ≈ 5 was retrieved to perform microstructural analyses. (e) SEM photomosaic showing mainly distributed deformation occurring via granular and cataclastic flows, similarly to the 50° saw-cut at 2.75 mm of shear displacement (Figure 1b-c).

We simulated gouge-bearing, pre-existing faults by

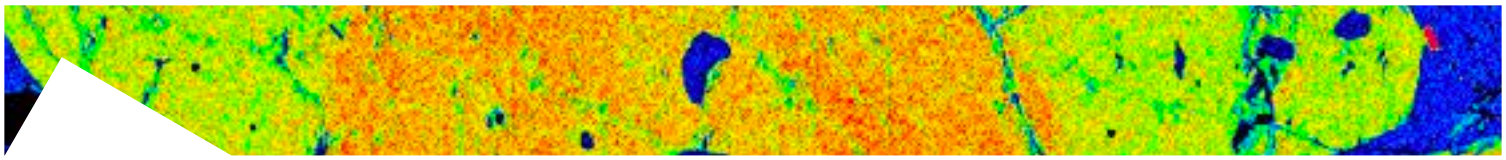

conducting triaxial experiments on sandstone cylinders containing a saw-cut, filled with gouge, at various orientations to the maximum principal stress. Firstly, we have characterized the frictional strength of the sandstone and the frictional properties of the gouge via triaxial and friction experiments, respectively. Then, triaxial saw-cut experiments on faults oriented from 30° to 80° with respect to the maximum compressive stress. Additionally, experiments with different total amount of displacement along a saw-cut with constant $\theta = 50°$ were performed to investigate the evolution of shear localization during fault reactivation. Microstructural observations were performed on thin sections parallel to the sense of shear with the JEOL JSM-6500 F thermal field emission scanning electron microscope installed in the HP-HT Laboratory at the INGV (Rome).

Triaxial saw-cut experiments show a complex reactivation behaviour, especially if compared to simple friction experiments. To understand this complex mechanical behaviour, the comparison between microstructures retrieved from saw-cut experiments and microstructures retrieved from simple friction experiments is of primary interest. The comparison between these and the previous collected microstructures allows a more complete understanding of the complex reactivation behaviour characterizing variably oriented faults (Figure 1).

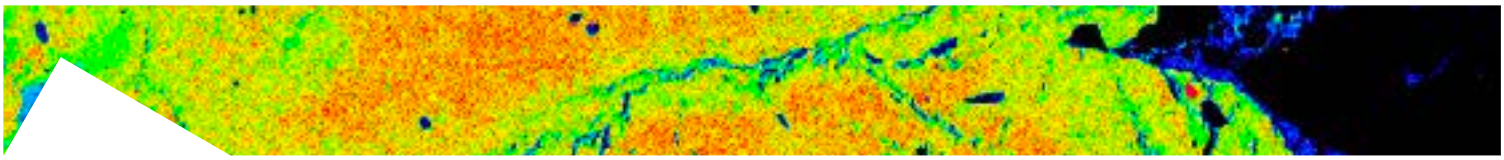

Temperature effects on acoustic measurements conducted on bitumen-saturated carbonate rocks of the Majella reservoir (Central Italy)

Ruggieri R., Trippetta F.

Unconventional oils are emerging as an alternative hydrocarbon reserve since conventional oil is depleting nowadays. A kind of unconventional oil is bitumen, which is characterized by high density, high viscosity and API gravity less than 10° and these physical properties are temperature sensitive. Thus, an accurate knowledge of the petrophysical properties of bitumen rocks as a function of temperature is a useful tool for the characterization of bitumen carbonate reservoir.

In this work, we have investigated the temperature effects on the seismic wave velocity in carbonate-bearing rocks of the Majella reservoir. This reservoir represents an interesting analogue for several onshore and offshore oil fields, and it can be defined as a natural laboratory to characterize the carbonate reservoir properties.

We have conducted ultrasonic measurements of compressional and shear wave velocities on six carbonate samples of the Bolognano formation at the HPHT laboratory of INGV, Rome. Wave velocities were measured in a range of temperature from 90 to30°Cat ambient pressure conditions. Firstly, we measured the bitumen density by HCl dissolution of the hosting rock, that has resulted to bei ncluded between 1.14 and1.26 gr/cm^3 at ambient temperature. By knowing the bitumen density, we have calculated the amount of the bitumen in each sample and it spans from about 3% (low HC-bearing sample) to 15% (high HC-bearing sample). Moreover, for all samples we have measured total porosity by using helium pycnometer and it is between 11% to 19%.

Laboratory data show that P- and S-wave velocities decrease linearly with increasing temperature (Fig. 1) and, in addition, Vp seems to be more temperature sensitive than Vs from 30 °C to 90 °C. Investigated samples exhibit a P-wave velocity spanning from 4.07 to 4.49 km/s at ambient temperature, while at high temperature Vp are in the range between 3.66 and 4.25 km/s. Consequently, the Vp/Vs ratio has a significantly drop with increasing temperature, defining a clear seismic signal, which is crucial to the determination of lithology as well as the identification of pore fluid. Moreover, Vp and Vs are also influenced by different bitumen level saturation. For the same porosity, wave velocities of low HC-bearing samples are generally higher than those of samples richer in hydrocarbon. Furthermore, the samples

with the highest bitumen content show a larger gradient of velocities change in the temperature range of about 70-50 °C, within which bitumen is in a fluid state. Conversely, below about 50 °C the velocity gradient is lower because, at this temperature, bitumen changes its phase in a solid state.

In conclusion, our results highlight a temperature dependence for HC-bearing carbonate samples and, according to the literature, they are less temperature sensitive respect to the bitumen sands, suggesting that the high stiffness of carbonate frame can inhibit the bitumen effect. Such petrophysical characterization would provide a better link between seismic parameters and the hydrocarbon properties; this is necessary to employ the seismic method for reservoir characterization as well as for production monitoring.

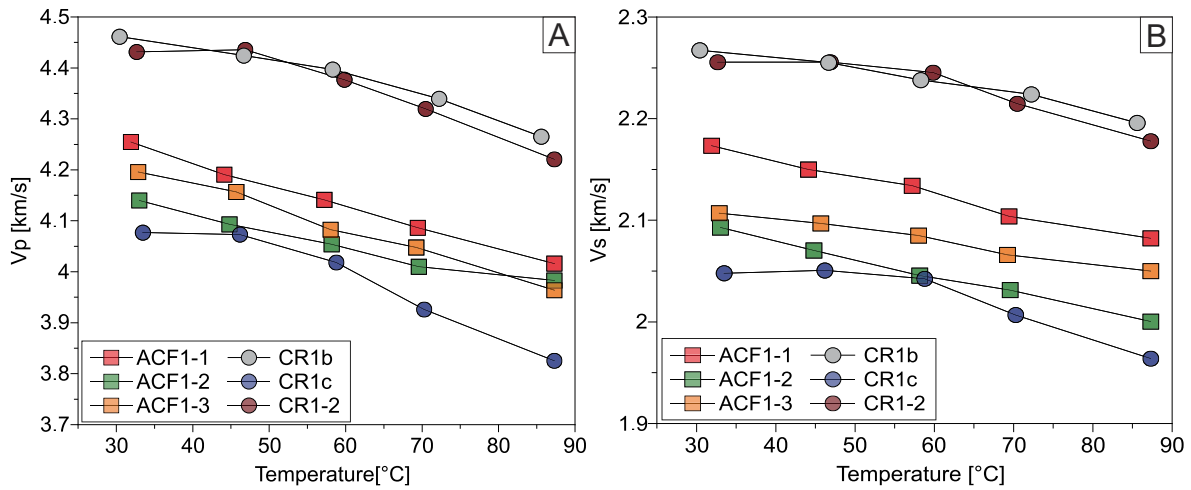

Fig. 1 I A) P- and (B) S-wave velocity variations with temperature of all investigated samples. For a better comprehension, the values of temperature and ultrasonic velocity measurements have been interpolated.

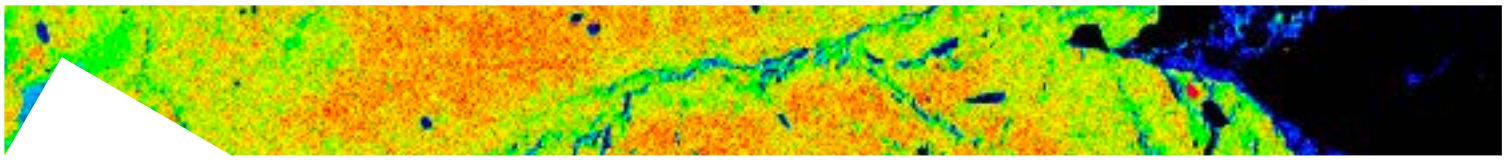

Frictional instability under fluid stimulation: insights from load-controlled experiments on pre-existing faults

Spagnuolo E., Violay M., Giacomel G., Cornelio C., Aretusini S. , Nielsen S., Di Toro G.

Fluid pressure is an important parameter controlling fault reactivation as well as natural and induced seismicity. The effective normal stress is linearly reduced by an increase in fluid pressure (Pf) via hydro-mechanical coupling which lowers the frictional strength of the fault increasing the potential for fault reactivation and seismic slip. However, during fault motion ,either seismic or aseismic, the permeability of the fault is likely to change for the effect of wear (e.g. production of gouge), healing or deformation of the asperities. This change in the transport properties of fluids through a fault zone may induce an unpredictable behavior of both fault stability and reactivation. To investigate the role of fault injection rates in seismic fault reactivation, we performed four tests using the rotary shear apparatus SHIVA, installed in the HPHT laboratory at INGV, Rome (Italy). Samples consisted in hollow cylinders of Carrara marble (50/30 mm ext/int diameter) inserted in a vessel for fluid confinement and put in surface contact under an initial effective normal stress σ_{eff}=10 MPa. The pore fluid was water in equilibrium with Carrara marble. In both cases, the shear stress was increased stepwise until the achievement of a frictional instability at a shear stress$\tau=\tau p$ (i.e. slip rate > 1 cm/s, color coded in Figure 1). Two other experiments were performed (s816 and s909) by applying a constant initial shear stress $\tau \sim 70\% \tau p$ (RH) and then pore fluid pressure was increased with an injection rate with steps of 0.5 MPa every 20 s and of 0.1 MPa every 30 s. For the ex-

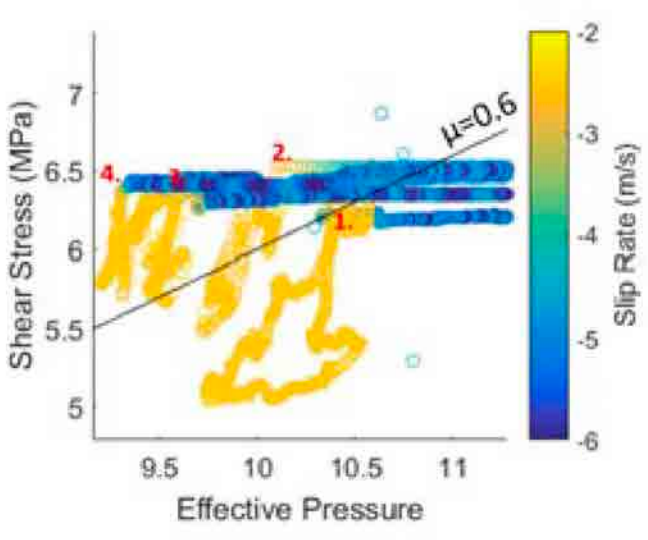

Fig. 1 I Experiment s909 was performed with a fluid injection rate of 0.1 MPa / 30 s and consisted in 4 cycles (red numbers) of fault loading by fluid pressure increase (consequently the effective pressure decreases as reported in abscissa). The series of experiments with fluid pressure show the high sensitivity of fault reactivation to fluid pressure. However, cycle after cycle, the friction coefficient at fault reactivation is gradually shifted towards higher friction values.

periments s814, s816 and s909 the fluid pressure was imposed radially from the outer ring towards the inner of the hollow cylinders.

In experiment s909, we tested the effect of four repeating cycles of loading and unloading by fluid pressure at 0.1 MPa every 30 s (Figure 1). The triggering of the main frictional instability was progressively delayed and the averaged effective friction coefficient increased gradually from 0.6 (episode 1.) to 0.8 (episode 4.) in the Mohr space. This mechanical behaviour suggests that fault permeability decreased during the test, probably because of wear and formation of gouge during the transient slip events. The permeability decrease made less effective the fluid penetration within the experimental slipping zone inhibiting the achievement of an equilibrium between the pore fluid pressure imposed externally and the actual fluid pressure within the fault. A consequence of this behaviour is that the effectiveness of the hydro-mechanical coupling is affected by fluid diffusion through pore or pre-existing fractures. This effectiveness maybe quantified considering that the normal load is on average reduced by fluid pressure according to $\sigma ave = \sigma n (1 - X/Pf)$, where X, the coupling coefficient, is reasonably affected by the diffusion time (td) over a characteristic length scale (L) required to equilibrate fluid pressure within the entire fault volume.

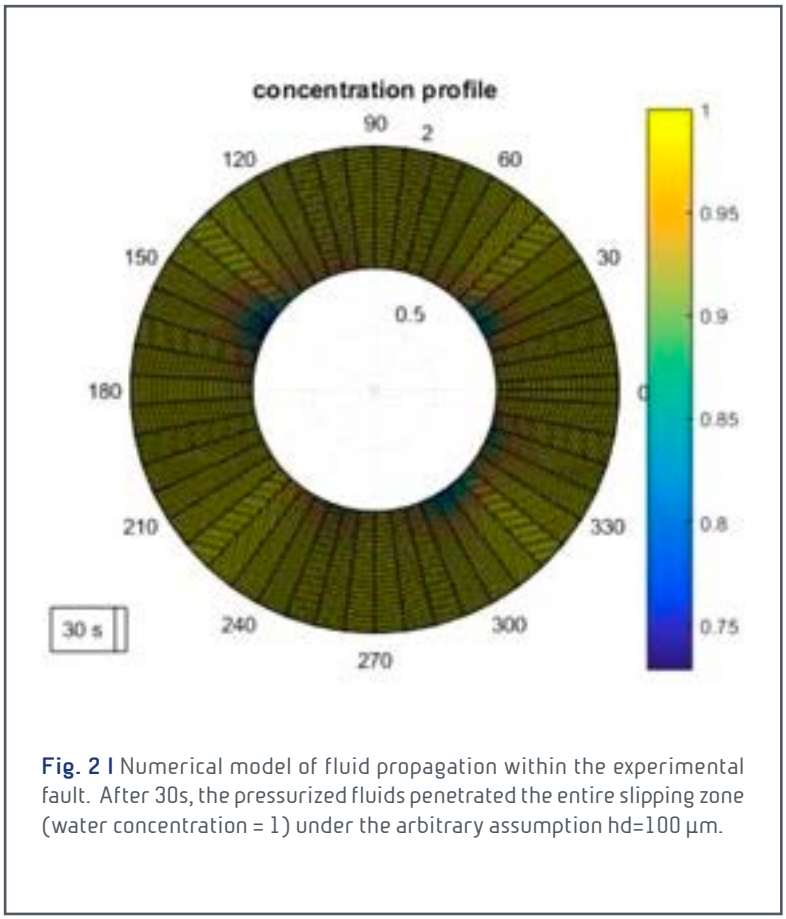

Fig. 2 I Numerical model of fluid propagation within the experimental fault. After 30s, the pressurized fluids penetrated the entire slipping zone (water concentration = 1) under the arbitrary assumption hd=100 µm.

To investigate this, we consider that the propagation of the fluid pressure disturbance obeys the Navier-Stokes equation. Its simplest solution is the cubic law representing laminar flow through two parallel plates separated by an aperture hd. Recalling the Darcy's law for flow through porous media, the permeability can be rewritten in terms of hd (m^2). By mo-

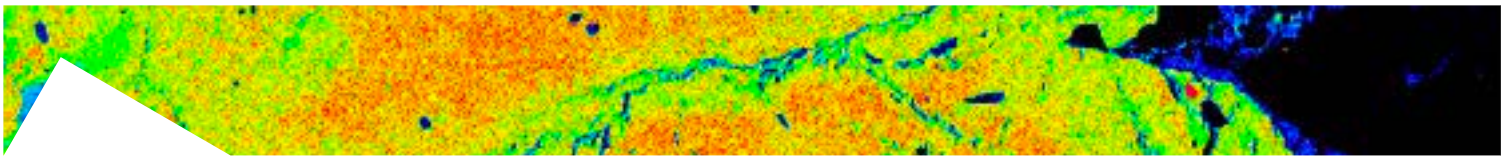

delling water flow through the hydraulic aperture under a fluid pressure step of 0.1 MPa, assuming an average hd = 100 µm and allowing random heterogeneities of hd on the fault plane, we estimated that after 30 s the fluid penetrated radially through almost the entire fault surface (Figure 2) and was effective in reactivating the fault (Figure 1, episode 1). The model support the hypothesis that the coupling coefficient X varies with the hydraulic aperture and the penetration time tp, i.e.X=f(hd, tp) which, as demonstrated in the case of experiment s909 (Figure 1), can evolve as hd evolves. Using the cubic law, with a direct measure of tp, of the effective pressure gradient, and a measured initial condition on hd (namely the initial fault roughness) we also aim at constraining the permeability change during the experiments and finding the best functional form of Xin critically loaded faults.

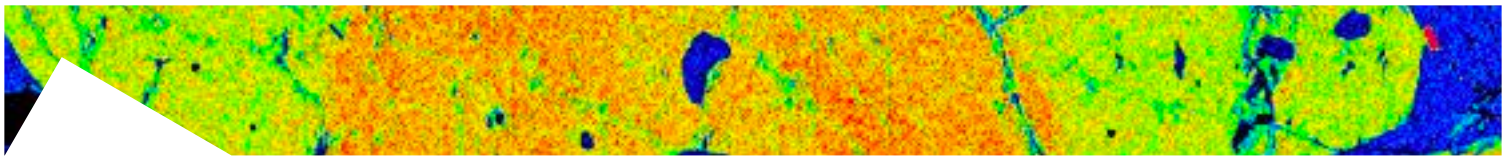

Fault stability during an experimental seismic cycle. The effect of controlled conditions of the loading rate

Spagnuolo E., Nielsen S., Violay M., Passelegue F., Di Toro G.

Earthquake nucleation is the last stage of the inter-seismic cycle where the fault surface evolves through the interplay of friction, healing, stress perturbations and strain events. Slip stability under rate-and state friction has been extensively discussed in terms of loading point velocity and equivalent fault stiffness, but fault evolution towards seismic runaway under complex loading histories (e.g. slow variations of tectonic stress, stress transfer from impulsive nearby seismic events) is not yet fully investigated. Nevertheless, the short term earthquake forecasting is based precisely on a relation between seismic productivity and loading history which remains up to date still largely unresolved.

To this end we propose a novel approach which avails of a closed loop control of the shear stress imposed on the experimental fault, a nominally infinite equivalent slip and transducers for continuous monitoring of acoustic emissions. The experimental fault has an initial roughness which mimics a population of randomly distributed asperities, here used as a proxy for natural fault patches, either far or close to failure on an extended fault. This experimental simulation allows us to study the stress dependency and temporal evolution of spontaneous slip events occurring on a pre-existing fault subjected to different loading histories and, at the same time, monitoring the evolution of the rough surface using the acoustic emissions source locations.

Our observations suggest that the increase of shear stress may trigger either spontaneous slow slip events (creep) or short-lived stick-slip bursts, eventually leading to a fast slip instability (seismic runaway) when slip rates are larger than a few cm/s. Event types and their occurrence are related to the number of asperities brought to failure as mapped by the acoustic emission source locations (Figure 1). The creep vs. stick-slip behavior and the magnitude of the slip rate are regulated in principle by the background shear stress whereas the effect of the cumulated slip is negligible. However, the slip history is conditional at first order on the loading type and an empirical relation can be established between the loading rate and the evolution of slip with time.

The extrapolation of these results to natural conditions might explain the plethora of events that often characterize

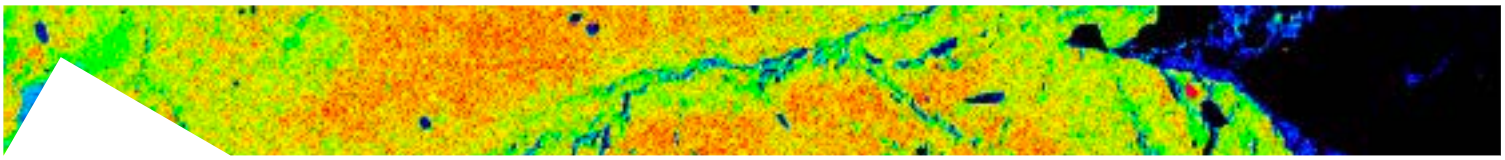

seismic sequences. Nonetheless this experimental approach helps the definition of a scaling relation between the loading rate and cumulated slip which is relevant to the definition of a recurrence model for the seismic cycle.

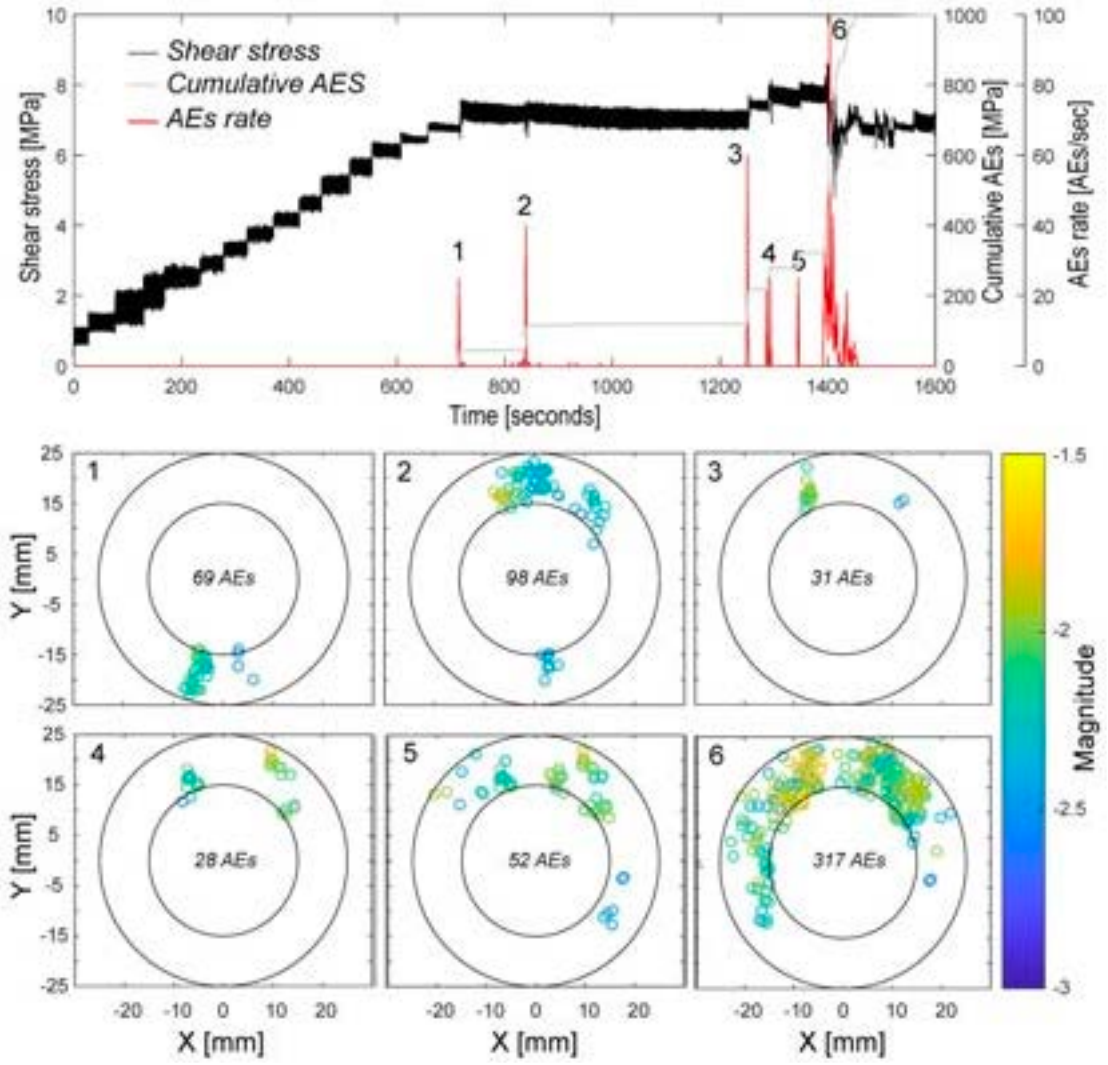

Fig. 1 | Location of AEs activity suggests the involvement of small asperities before the onset of a main instability. Microslip recorded at subcritical shear stress is a consequence of the heterogeneous distribution of the shear - and normal- stress on a rough frictional interface made up of asperities where the Coulomb friction law can be satisfied locally.
The surface from which microslips start has at first a very small area, which may quickly become very large, but at a rate not greater than the velocity of compressional elastic waves in the rock. Oscillations result from the competition between evolving micro-stiffness of the contact surface and the constant stiffness of the apparatus (0.07MPa/um, $K \approx \tau/\sigma\delta$).

Stored elastic strain energy and energy release in the north Sumatran subduction zone: experimental investigation on the input sediments

Spagnuolo E., Aretusini S., Vannucchi P., Di Toro G.

The energy budget is a key parameter to investigate earthquake mechanics. However, our knowledge about the amount of elastic strain stored in the seismogenic volume and the energy released during an earthquake is limited by: (1) the observational time (orders of magnitude shorter that the recurrence time of moderate to large earthquakes); (2) the paucity of historical records and the scarcity of instrumental coverage; (3) the availability of only indirect measures (e.g., from seismic and GPS inversion at the surface); (4) the lack of sound estimates about the energy dissipated in on-fault and off-fault processes during earthquakes.

One way to reduce the observational time and enlarge the number of observations is the experimental simulation. Experiments provide a quite robust reproduction of seismic source processes, confirmed by geological evidence (experimental fault products are very similar in many cases to natural ones) and guarantee a control on the environmental and loading

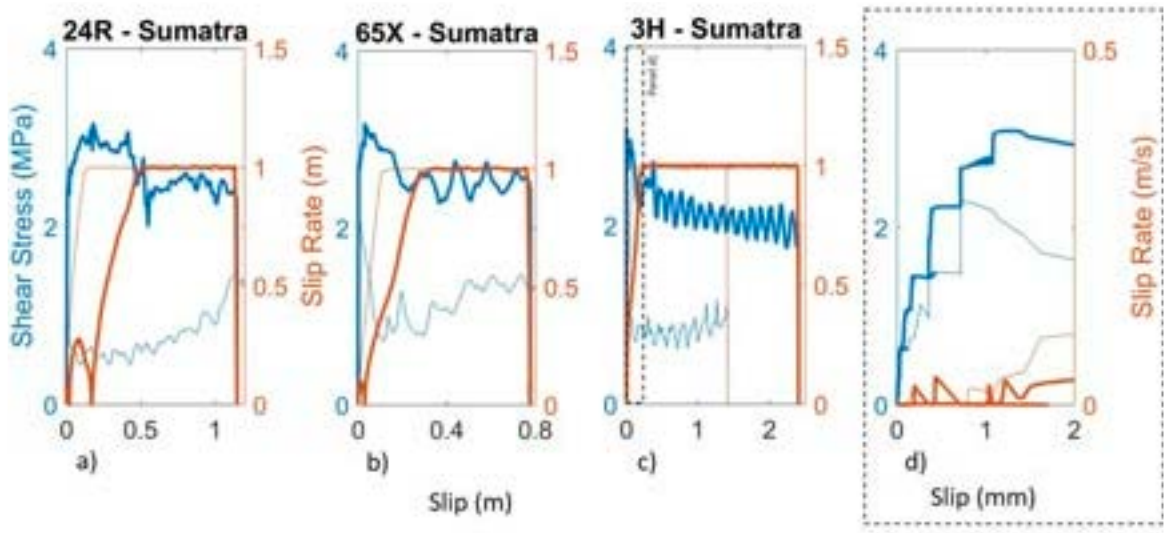

Fig. 1 I Creep test on samples 24R (dark bioturbated clays), 65X (silty clays), 3H (Carbon oozes). Shear stress in blue and light blue for RH and wet experiments respectively. Slip velocity which is here evolving spontaneously is in red and light red for RH and wet experiments respectively. For each sample, the two subpanels show an overview of the experiment (left) versus the cumulated slip and a zoom (right) on the slip behavior right before the onset of the frictional instability. Sample 24R is highly stable. It cumulates 20 cm of slip before running into a frictional instability and can cumulate a large amount of stress (shear stress of 3.5 MPa over a normal load of 5 MPa in Figure 1). On contrary 3H can cumulate the same amount of shear stress but it is highly unstable. 3H is essentially locked in comparison with 24R and cumulates only 2 mm before running into a frictional instability.

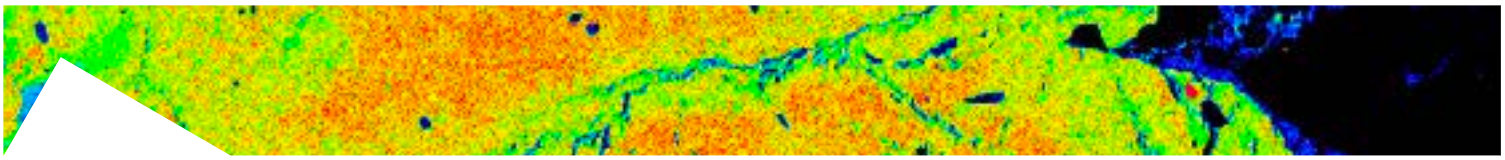

conditions of the simulated fault. In particular, experiments performed with high velocity frictional apparatuses (so imposing slip and slip rates typical of moderate to large in magnitude earthquakes), a number of constraints have been retrieved regarding the energy dissipated during seismic slip (on-fault processes) and, to some extent, the energy required to propagate seismic slip (i.e. fracture energy).

To acquire more information and shed light on the capability of fault zone rock materials and the wall rocks to store elastic strain and release it in different forms (seismic waves, grain size reduction, frictional heat, etc.), we performed experiments with a rotary shear apparatus (the stiffness of the machine simulates the wall rock stiffness) by controlling the normal stress acting on the experimental fault and (1) observing the evolution of shear stress under steps in the slip rate and (2) observing the spontaneous evolution of slip and slip rate as the shear stress is increased stepwise (e.g. with steps of 0.1 MPa every 100 s) until the experimental fault spontaneously accelerated to 1 m/s.

We tested non-cohesive materials sampled via scientific drilling in the sediment input to the north Sumatran subduction zone (IODP Exp. 362). These materials were sampled at about 200 km from the deformation front and, although they are the same that are currently deforming in the shallow portions of the subducting interface, they may underestimate future diagenesis. These experiments allowed us to measure the initial, dynamic, and residual shear stress at different stages of the seismic cycle which are essential to compute the energy budget of large megathrust earthquakes as the 2006 Mw 9.3 Sumatra-Andaman earthquake.

Our experiments revealed that fault materials at the shallow portions of the accretionary prism can store a relatively large amount of elastic strain energy, largely depending on the water content, but enough to promote seismic slip propagation when stimulated by a perturbation in the loading conditions.

Though the high velocity weakening behavior seems similar for all fault materials the way silty/dark clays (e.g. samples 65X, 24R in Figure 1) cumulate and adjust the shear stress is different from the behavior of carbonatic (sample 3H) resulting in a different available energy and in a different fault stability (Figure 1).

CARB/SIL Oozes (Figure 1, blue lines) behave like locked fault patches. They can accumulate high stress and release it all at once.

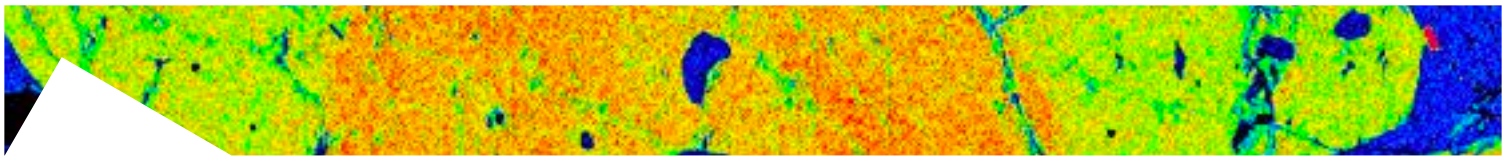

Silty/dark clays (Figure 1, green lines) behave like creeping patches. They release the stress by creep but also through small fast (> 0.1 m/s) events.

These experiments may contribute to our understanding of fault stability and the likelihood that seismic slip can propagate up to the trench, an observation that since the Mw 9.0 Tohoku Oki 2011 earthquake is puzzling our current understanding of earthquake mechanics.

8.3 TECHNOLOGY

Audio amplifier

Romeo G., Spinelli G.

Three years ago LNTS built and patented (Italian patent application n. 102015000071865) an audio amplifier.

The idea behind this amplifier is to give to the users the possibility to control the transducer's damping factor, in the same way a seismologist can control the damping factor of a geophone. This allows to reach a quality in sound reproduction unreachable without the perfect coupling amplifier-loudspeaker.

The original prototypes were derived from amplifiers dedicated to control the power of dc brushed motors, thought for ACS control of stratospheric balloons payloads.

We built a third prototype employing components suited for audio use, and providing a better designed power section, with a perceivable improvement of performance.

The prototype won the participation to the National Geographic Science Festival in Rome scheduled for April 8-14, 2019.

Fig 1 sows the last prototype (left) and a internal detail of the vu-meter.

Fig. 1 I The last prototype of the audio amplifier (left). The first knob allows the use to tune the loudspeaker damping factor. On the right a particular of the vu-meter.

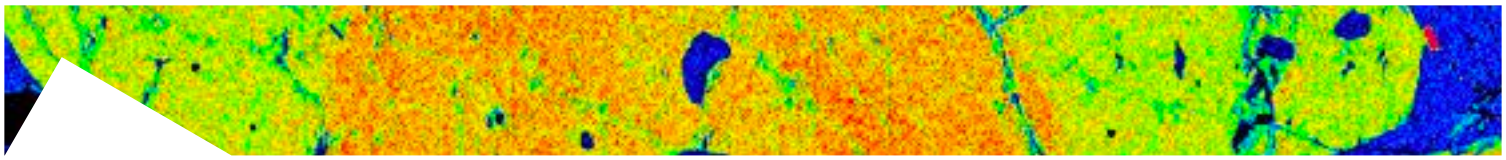

Machine shop activity

M. Mari

Although it cannot be counted as research work, the machine shop work is essential to the conduct of all experimental investigations. Moreover the machine shop is the reference facility for the whole INGV Rome site, and performs several machining on request. Usually the machining average is of 1000 machining per year, from consumable for physics rocks experiments to more complex dedicated parts.

Olimpo Integration

Di Stefano G., Pongetti F., Romeo G., Spinelli G.

Since 2003 INGV is part of the Olimpo collaboration, offering its skill in electronic design and prototyping. In 2018 Olimpo has been launched from Longyearbyen (Svalbard Islands) and INGV participated to the integration campaign before launch.

The INGV role:

- general support in electronics design and debug;

- design and building fine and coarse sun sensors;

- upgrading the fine sun sensor with a auto-ranging system;

- Interfacing old Boomerang's sun sensors with the ACS computer;

- Stabilize the telescope azimuth positioning loop.

Some electronic devices and some code have been produced to accomplish these tasks.

In particular a data collector and encoder was designed to allow the sun sensors to communicate with the ACS computer (Fig. 1) introducing some redundancy in data transfer.

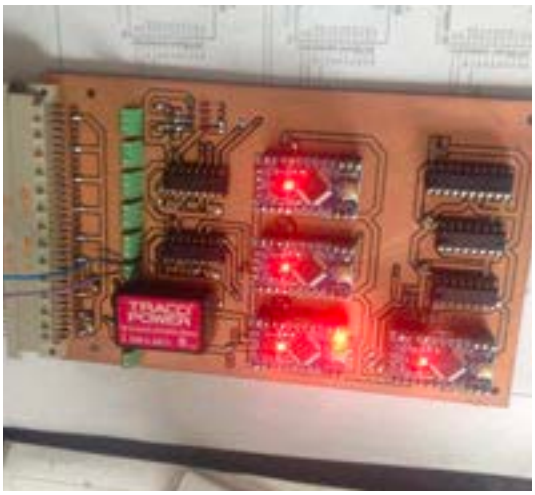

Fig. 1 I Data collector and interface based on several Arduino mini pro.

Fig. 2 I Galvanically isolated serial interfaces have been widely used to allow electrically safe connections between sections of the gondola electronics.

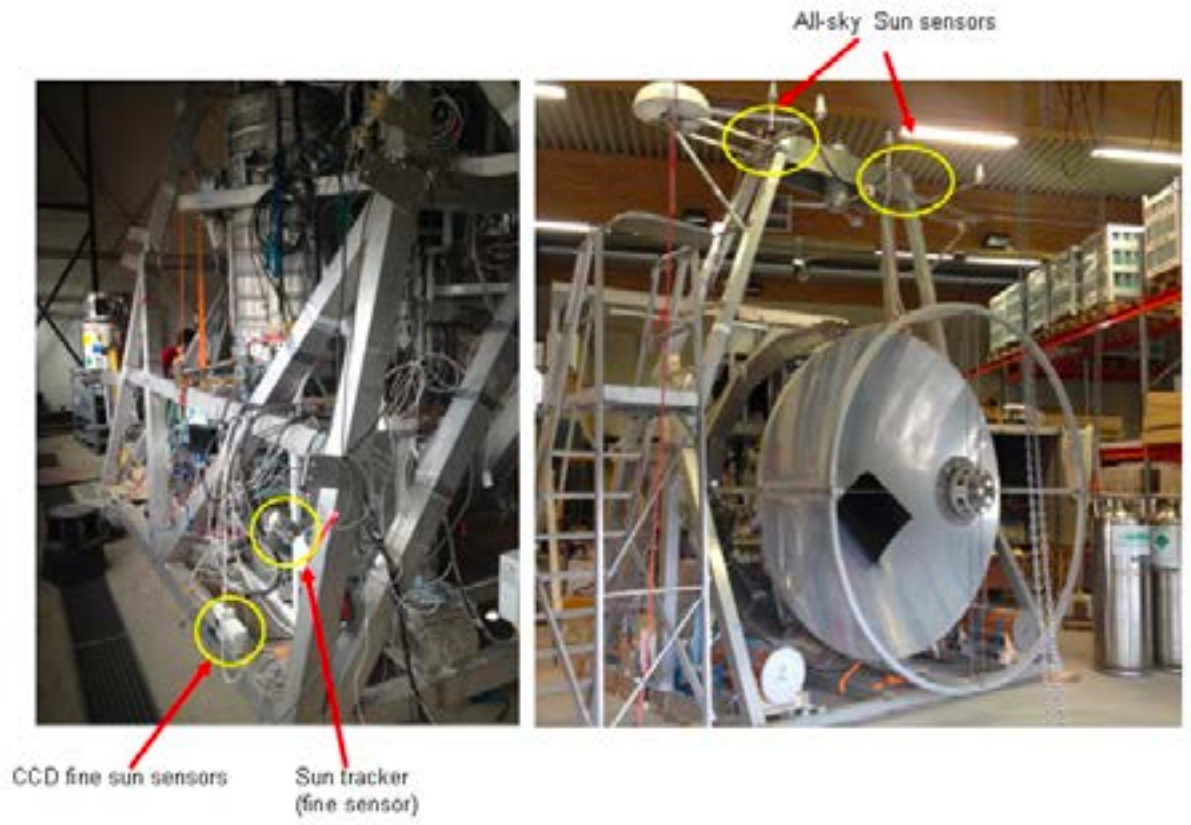

Fig. 3 I The Olimpo gondola during the integration. Yellow circles evidence the LNTS stuff.

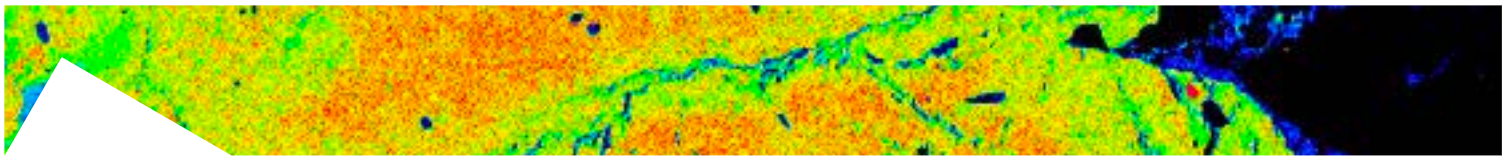

An autoranging redout system for 4-quadrants or PSD light detectors

Romeo G., Spinelli G., Di Stefano G.

PSD (Position Sensitive Detectors) sensors are a simple choice to detect the barycentre of a light spot. The PSD Theory of operation is depicted in fig.1. It may be demonstrated that the position is proportional to the ratio of difference and sum of the currents i1 and i2:

$$\frac{i_1 - i_2}{i_1 + i_2} = \frac{d_2 - d_1}{d_2 + d_1} = \frac{2 \cdot d_2 - D}{D} \tag{1}$$

where $D = d_2 + d_1$

This ratiometric method is directly usable when the light intensity is known or controllable to fit the dynamic range of electronics. If not (and this is the case of the natural light sources) a method may be provided to keep the signal in range. The principle used is shown in figure 2.

$$V_{out}(t) = \frac{1}{C}\int_0^T I(t)dt \tag{2}$$

Figure 2 shows a transresistance device whose amplification is tied to the integration time. In this way we may keep

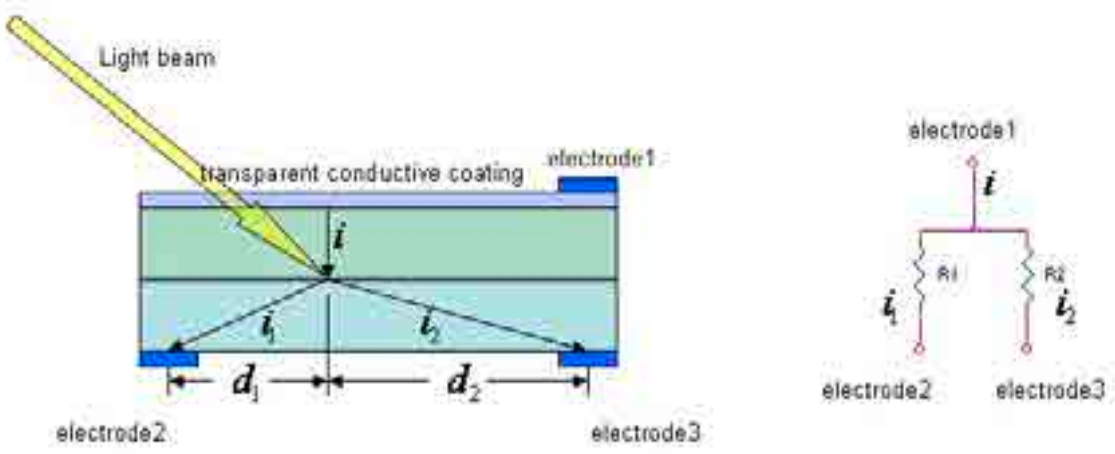

Fig. 1 I The light beam on the junction produces two currents whose values are used to determine the position of the light incidence point.

constant the quantity i1+i2, just stopping the integration time after reaching a threshold. Moreover keeping constant the denominator of the (1) avoids the need of the division and performs a kind of anti aliasing filter on the light position.

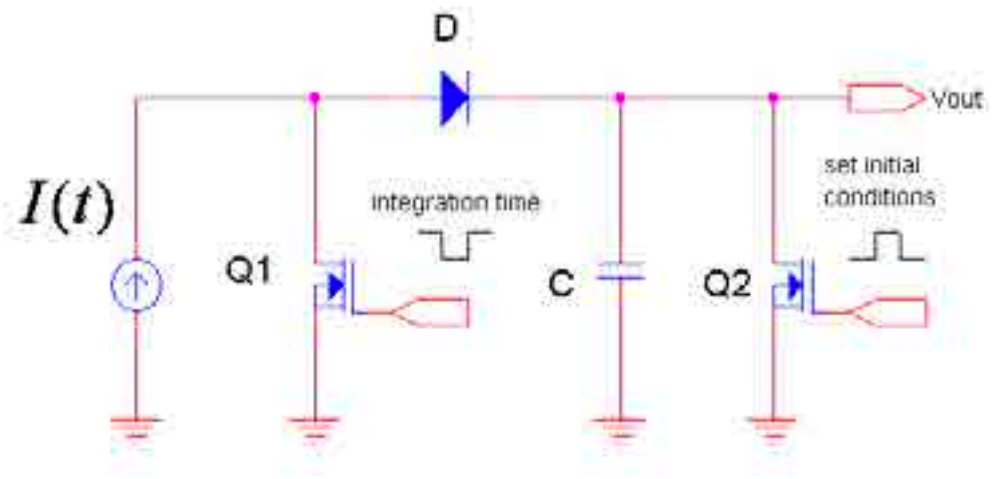

Fig. 2 I A current to voltage converter using a capacitor charge. After setting the initial conditions the length of the integration time determines the gain of the current to voltage converter.

A prototype based on this idea (Fig. 3) has been built, tested and used in the ACS system of Olimpo, the stratospheric telescope launched from Longyearbyen the June 22nd, 2018. It offered a gain spanning 2 orders of magnitude, allowing both ground test and stratospheric operation with no modification, and worked as expected during one week in stratosphere.

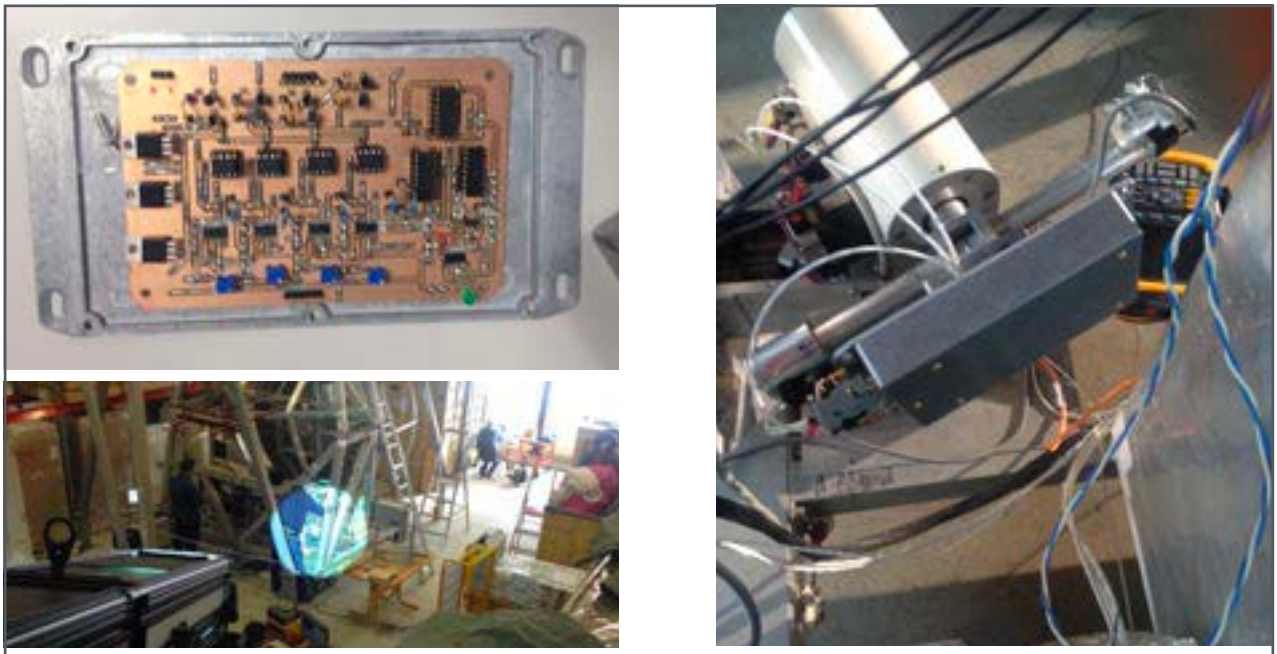

Fig. 3 I A PSD redout redout (left) in his aluminium box, mounted on the moving head of the sun sensor (the grey box in the middle), and installed on the Olimpo gondola (right), in the middle of the lit circle. This circle simulated the direction of the sunlight (roughly 1/8 of the effective light expected in the stratosphere) and was used for testing purposes.

MEMS gravimeter

Romeo G., Mari M,. Iarocci A.

A gravimeter designed to measure intensity and direction of gravity is now under debug. We cannot report the detail of the design to avoid invalidating its patentability.

The device (Fig. 1, left) is based on a high quality accelerometer MEMS used in an unconventional way and can return one axis tilt information as well as the absolute value of the gravity. Currently the feedback intended for temperature stabilization is not closed yet, and the temperature completely blinds the gravity intensity measurements. The instrument's tiltmetric capability is not strongly affected by the temperature, and a one-day recording (the first test) showed a 12 hours period wave form that is not correlated with the temperature (24 hours period) figure 1, right.

One of the requirements for the instrument is the precise and smooth control of a motor. Several way have been attempted to do that. One of them uses two DDS (Digital Direct Synthesizer), and two hi-current operational amplifier (to provide the high currents for the motor windings).

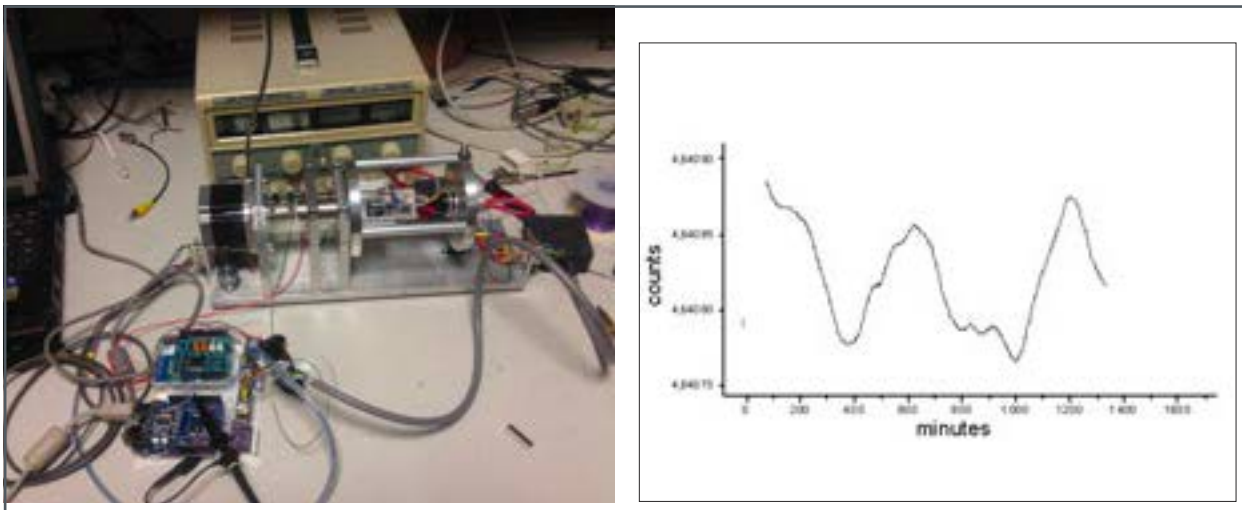

Fig. 1 I Left a partial assembly of the instrument under test; right a 12 hours period tilt recorded during the first test. This period is not correlated to the room temperature.

Rotational seismometer

Romeo G., Mari M., Govoni A., Di Virgilio A., Orazi M.

The modification described in the previous report (Fig. 1) has been performed and the experimental instrument has been installed in Pisa, near the GINGER Laser Gyro (Fig. 2) and in the Rocca di Papa Museum, near a liquid-mass rotational seismometer eentec E-1. Because of the inclination of the GINGER and the impossibility to install the sts-1 on the same rotational plane made impossible to have a nice comparison of the two instruments. The comparison between the STS-1 and the E-1 has not been done yet.

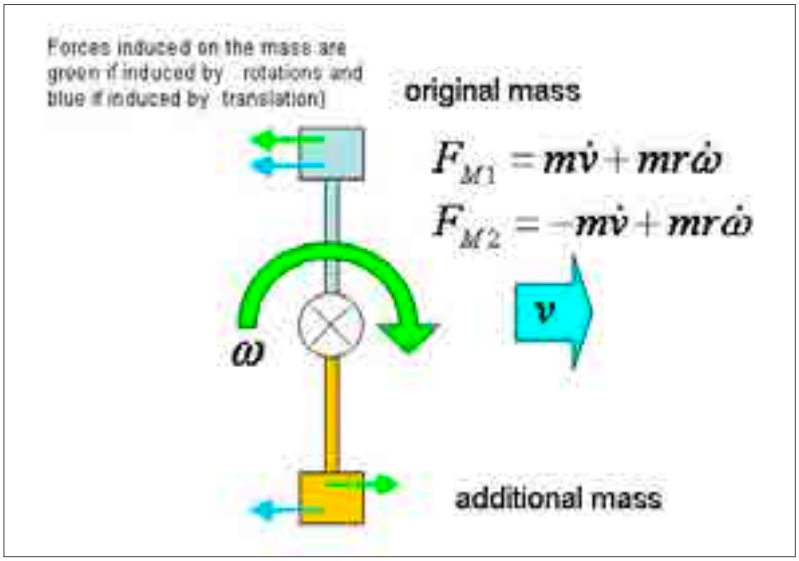

Fig. 1 I A seismometer with a pivot-suspended mass naturally exhibits some sensitivity to both translation and rotation. An additional mass cancels its sensitivity to translation, increasing the sensitivity to rotation.

Fig. 2 I Experimental installation of the rotational sts-1 near GINGER (left) and in Rocca di Papa museum basement (right).

Amplifier add-on

Romeo G., Spinelli G.

This device allows tuning the damping factor of an electromagnetic transducer regardless to the amplifier it is connected to. For this device a patent application has been submitted in Italy (application 102018000003588, March 15 2018).

This is the natural extension of the INGV's audio amplifier and allows any amplifier to get performances close to it. It is an active device who adds a correction to an existing system operating on the power transducer path.

Figure 1 shows the prototype and the time diagram of the transducer position (simulation output) before (black) and after (red) inserting the device.

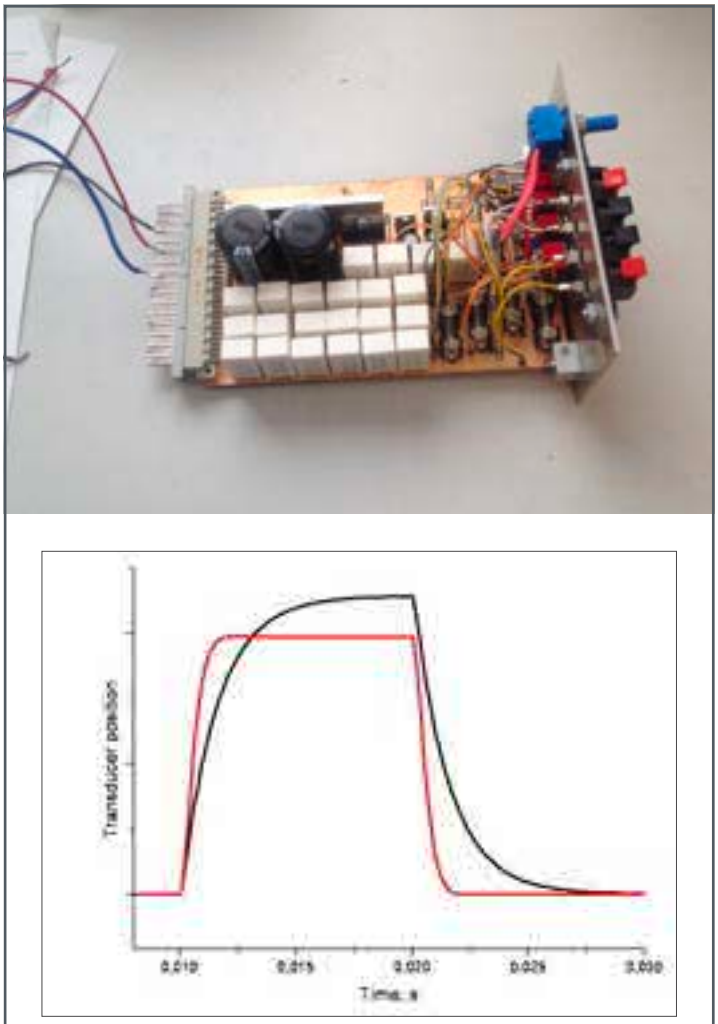

Fig. 1 I The prototype (left) and the time diagram of the transducer response (position) to a square wave excitation. The black track shows the transducer's response before inserting the device, the red track after inserting the device.

Radon meter housing

Tozzi M.

A 3d-printed housing and a high efficiency switching power supply have been designed and built to power Radon stations of the IRON network. The power supply incorporates an automatic buck/boost feature, and keeps a stable output voltage even if the input voltage is below the output voltage. The circuit offers short circuit ant thermal protections. The efficiency spans from 50 to 90% depending of the input voltage and allows more than 3 years of continuous operation of an ALGADE radon meter. Figure 1 shows the 3d-printed box and the small power supply PCB.

Fig. 1 I Radon housing with power supply. On the left the small power supply PCB.

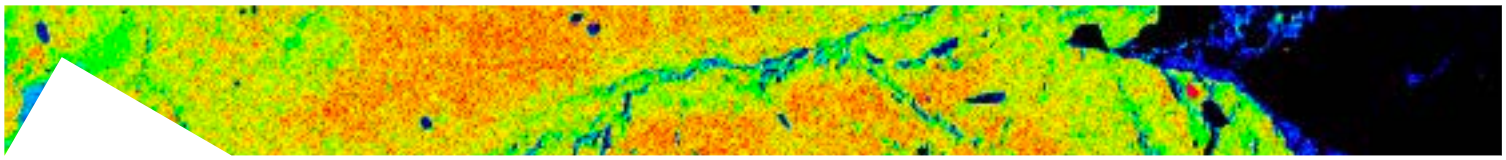

9| SEMINARS and TEACHING

Seminars

Del Bello E. | L'attività esplosiva basaltica: osservazioni sui vulcani attivi italiani | Università Roma Tre, Scienze Geologiche, corso di Introduzione alla vulcanologia | Roma, Italy **|** 23 May 2018

Taddeucci J. | Volcanic eruption styles: lights and shadows (as seen by a field and experimental perspective) | Short Course on Melts, Eruptions and Risks, Università di Perugia | Perugia, Italy **|** 20-22 March 2018

Taddeucci J. | HOW DEEP CAN YOU GO? Problems and perspectives in retrieving the source depth of Strombolian-style explosive volcanic eruptions | Ludwig Maximillians Universitat of Munich | Munich, Germany **|** 5 June 2018

Training

1. **Pennacchia F.** | Stage | **Imaging techniques for the study of eruptive parameters | Supervisors:** Del Bello E. - INGV – Roma1

2. **Chiominto G.** | Stage | **Analisi di video ad alta velocità dell'attività esplosiva di tipo stromboliano | Supervisors:** Taddeucci J. - INGV – Roma1 | Palladino D. M. - Sapienza Università di Roma

Thesis

1. **Chiominto G.** | Master Thesis | **Dinamiche di esplosioni con cariche multiple e loro implicazioni sulle eruzioni vulcaniche | Supervisors:** Taddeucci J. - INGV – Roma1 | Palladino D. M. - Sapienza Università di Roma

2. **Moltoni R.** | Triennale Thesis | **Caratterizzazione di rocce di faglia sperimentali | Supervisors:** Collettini C. – Sapienza Università di Roma | Ruggieri R. – Sapienza Università di Roma

3. **Palummo F.** | Master Thesis | **Magma dynamics at Vulcano island (Aeolian archipelago) as revealed by clinopyroxene zoning: a thermobarometric approach | Supervisors:** Mollo S. – Sapienza Università di Roma | De Astis G. - INGV Roma1

PhD

1. **Nazzari M.** | PhD | **Unravelling the effect of undercooling on (dis)equilibrium textures and compositions of basaltic magmas | Supervisors:** Mollo S. - Sapienza Università di Roma

2. **Giorgetti C.** | PhD | **Caratterizzazione strutturale e meccanica in faglie in misture di carbonati e fillosilicati | Supervisors:** Collettini C. - Sapienza University of Rome | Scuderi M. - Sapienza Università di Roma

3. **Mercuri M.** | PhD | **Struttura e comportamento meccanico di zone di faglia carbonatiche in presenza di plaghe argillose | Supervisors:** Collettini C. - Sapienza University of Rome | Carminati E. - Sapienza Università di Roma

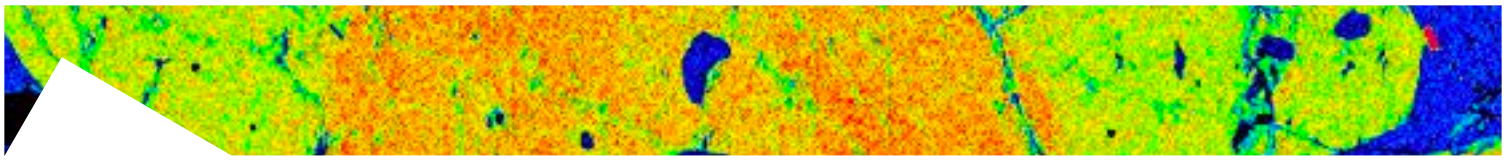

4. **Giacomel P.** I PhD I **Laboratory investigation on the frictional properties of basalts interacting with H_2O- and CO_2-rich fluids and implications for CO_2 storage I Supervisors:** Collettini C. - Sapienza University of Rome I Spagnuolo E. - INGV Roma1 I Di Toro G. - Università di Padova

5. **Ruggieri R.** I PhD I **Experimental investigation on fault stability of clay-bearing carbonate fault rocks I Supervisors:** Trippetta F. - Sapienza Università di Roma I Scuderi M. – Sapienza Università di Roma I Di Stefano G. -INGV Roma 1

6. **Tournigand P-Y.** I PhD I **Field-based study of volcanic ash via visible and thermal high-speed imaging of explosive eruptions I Supervisors:** Palladino D.M. - Sapienza Sapienza Università di Roma I Taddeucci J. - INGV Roma1

7. **Salvatore V.** I PhD I **Strombolian explosions: relationships between the conduit system and the resulting explosive activity at the vents I Supervisors:** Palladino D.M. - Sapienza Università di Roma I Taddeucci J. - INGV Roma1

8. **Di Stefano F.**I PhD I **Olivine-clinopyroxene-plagioclase-melt cation exchange reactions as a tool for understanding magma dynamics I Supervisors:** Mollo S. - Sapienza Università di Roma I Scarlato P. - INGV Roma1

9. **Palummo F.**I PhD I **Reconstruction of the intensive variables and magmatic architecture of Vulcano island (Aeolian Arc, Italy) I Supervisors:** Mollo S. - Sapienza Università di Roma I De Astis G. and Nazzari M. - INGV Roma1

10. **Lang S.** I PhD I **Kinetic aspects of major and trace element partitioning between olivine and melt during solidification of terrestrial and extraterrestrial basaltic materials I Supervisors:** Mollo S. - Sapienza Università di Roma I Lyderic France – CRPG; Université de Lorraine I Misiti V. - INGV Roma1

11. **Pontesilli A.** I PhD I **Unravelling the origin and differentiation of alkaline magmas feeding both effusive and explosive eruptions I Supervisors:** Brenna M. and White J. – University of Otago I Masotta M. – University of Pisa I Mollo S. - Sapienza Università di Roma I INGV Roma1

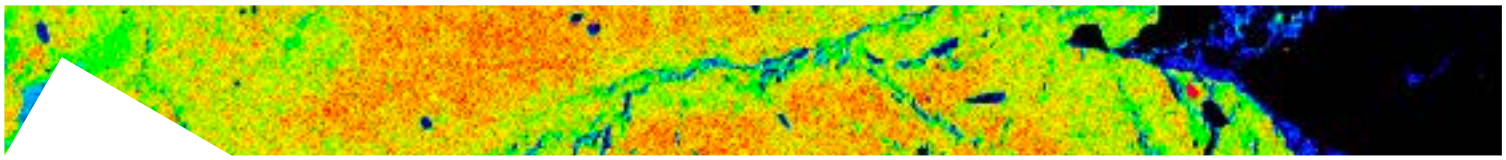

10| VISITING SCIENTISTS

Ubide T. | University of Queensland | Australia | *May*

Pontesilli A. | University of Otagol New Zealand | *July*

Marone C. | Penn State University | Pennsylvania, USA | *October*

Johnson J. | Boise State University | Idaho, USA | *November*

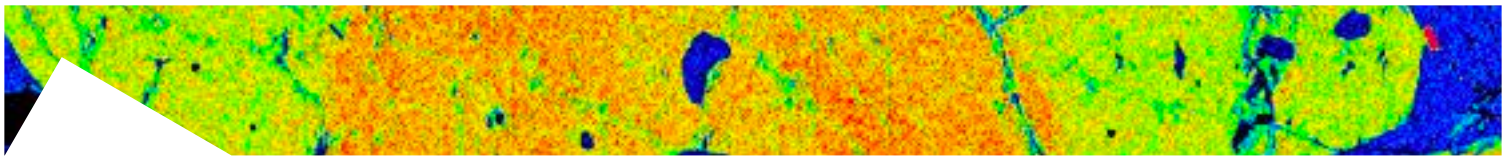

11| MEETINGS, WORKSHOP and SYMPOSIA

Meetings and sessions organization

Calvari S., Bertagnini A., Giudicepietro F., Paonita A., Scarlato P.
Giornate di studio INGV sul Vulcano Stromboli | Catania, Italia | 27-28 February

Agard P., Romano F., Mouslopoulou V., Rondenay S., Spagnuolo E., Rietbrock A.
Session: Subduction interface properties and large subduction earthquakes: integrating geological and geophysical observations, laboratory results, and numerical modeling (co-sponsored by JpGU) (co-organized)
European Geoscience Union | Wien, Austria | 8-13 April

Mollo S., Masotta M., Putirka K., Bachmann O. Scarlato P.
Session: Magma dynamic in volcanoes environments: crystallization, mixing and contamination processes
Goldschmidt Conference 2018 | Boston, USA | 12-17 August

Graettinger A., Lefebvre N., Ross P.-S., Taddeucci J., Valentine G., White J.D.L
Session: Phreatomagmatic eruptions: how do you know and how does it matter?
Cities on Volcanoes | Napoli, Italia | 2-7 September

Ricci T., Esposti Ongaro T., Liotta M., Sciarra A., Tomasek I.
Session: Volcanic-hydrothermal systems: structure, dynamics, monitoring and hazards
Cities on Volcanoes | Napoli, Italia | 2-7 September

Vona A., Del Bello E., Capponi A., De Michieli Vitturi M., Russell K., Perugini D.
Session title: The contribution of experimental and numerical investigations of eruptive processes for improving hazard assessment at volcanoes
Cities on Volcanoes | Napoli, Italia | 2-7 September

Scarlato P. Taddeucci J., Del Bello E., Ricci T., Andronico D., Kueppers U.
Broadband Acquisition Imaging Operation Workshop | Stromboli, Italia | 8-13 September

Meetings and sessions attendance

The 54th annual conference of the Volcanic and Magmatic Studies Group | University of Leeds, UK | **January**

Ubide T., Mollo S., Zhao J.X., Nazzari M., Scarlato P.
Sector zoned clinopyroxene records magma mixing and ascent

Giornate di studio INGV su Stromboli | Catania, Italia | **February**

Del Bello E., Taddeucci J.,Scarlato P., Gaudin D., Capponi A., Andronico D., Ricci T.
Vent plugging modulates explosivity of strombolian eruptions

Taddeucci J., Alatorre-Ibargüengoi M. A., Del Bello E., Scarlato P.
In-flight dynamics of volcano ballistic projectiles at Stromboli

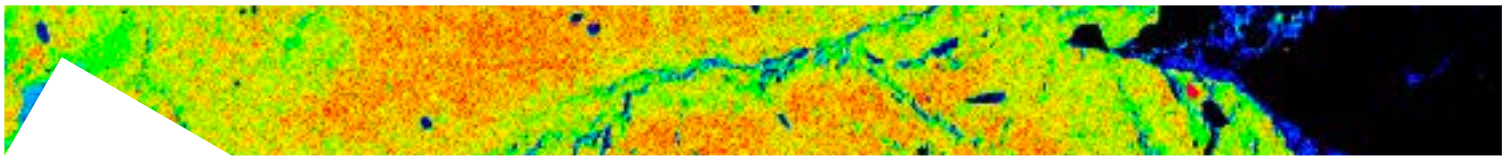

European Geoscience Union General Assembly | Wien, Austria | 8-13 April

Cigala V., Arciniega-Ceballos A., Salvatore V., Taddeucci J., Kueppers U.
Particles in motion: coupling high-resolution videos and geophysical techniques in the lab to decipher pyroclast ejection dynamics

Deegan F.M., Bédard J.H., Troll V.R., Dewing K., Grasby S., Sanei H., Harris C., Yakimchuk C., Sheih S., Freda C., Misiti V., Mollo S., Geiger H., Evenchick C.A.
The Stiff Upper LIP: investigating the thermal impact of basaltic sills on sedimentary host rocks in the High Arctic Large Igneous Province

Del Bello E., Taddeucci J., Houghton B., Patrick M., Orr T., Scarlato P., Gaudin D.
Small-scale outgassing dynamics at the Halema'uma'u' lava lake

Kueppers U., Taddeucci J.,Cigala V., Turner N., Houghton B., Andronico D., Biasse S., Cimarelli C., Colombier M.,Del Bello E., Gaudin D., Knüver M., Mueller S., Pisello A., Scarlato P., Sesterhenn J., Ricci T., Tournigand P.Y., Walker B., Zaia Z.
Rapid evolution of vent and crater morphology at Stromboli volcano

Lanzafame G., Iezzi G., Ventura G., Mancini L., Tamburrino S., Mollo S., Signanini P.
Proximal and distal deep submarine tephra deposits: the Marsilian-like eruptions

Pontesilli A., Masotta M., Nazzari M., Mollo S., Scarlato P., Brenna M.
Amphibole thermobarometry of trachyte/syenite bodies in the Dunedin Volcano: implications for the plumbing system evolution

Taddeucci J., Gaudin D.,Turner N.,Kueppers U.,Knüver M.,Peña Fernandez J.,Del Bello E.,Ricci T.,Sesterhenn J.,Cimarelli C.,Houghton B.,Scarlato P., Bucci A., Rao S.
Signals and sources of Strombolian explosions: linking acoustic and thermal infrared recordings with UAV-based vent geometries

Tournigand P.Y., Taddeucci J., Gaudin D., Peña Fernandez J., Perugini D., Del Bello E., Scarlato P., Kueppers U., Sesterhenn J.
Morphological and dynamical evolution of transient volcanic plumes and their relationship to source properties

Goldschmidt 2018 | Boston, USA | 12-17 August

Di Stefano F., Mollo S., Scarlato P., Nazzari M., Bachmann O., Caruso M.
Olivine compositional changes in primitive skarn environments: A reassessment of divalent cation partitioning models to quantify the effect of carbonate assimilation

Masotta M., Pontesilli A., Ubide T., Armienti P., Mollo S., Nazzari M., Scarlato P.
Very fast magma dynamics at Mt. Etna revealed by clinopyroxene growth rates

Nazzari M., Di Stefano F., Mollo S., Scarlato P., Tecchiato V., Ellis B., Bachmann O., Ferlito C.
Modeling the Crystallization and Emplacement Conditions of a Basaltic Trachyandesitic Sillat Mt. Etna Volcano

Scarlato P., Mollo S., Tuccimei P., Galli G., Iezzi G., Soligo M.
Enhanced radon emissions from volcanic rocks exposed to high-temperature conditions: Implications for the geochemical survey and public health in densely populated volcanic areas

Geosciences for the environment, natural hazard and cultural heritage | Catania, Italy | 12-14 September

Caricchi C., Winkler A., Macrì P., Nazzari M., Guidotti M., Owczarek M., Amoroso A., Di Giosa A., Listrani S.
Biomonitoring of air pollution by magnetic measurements on native and transplanted lichens from area subjected to arsons in Rome, Italy

De Cristofaro S.P., Polo L., Giordano D., Janasi V., Masotta M., Mollo S.
Preliminary experimental petrology investigation of Caxias do Sul magmas of the Paraná-Etendeka Magmatic Province

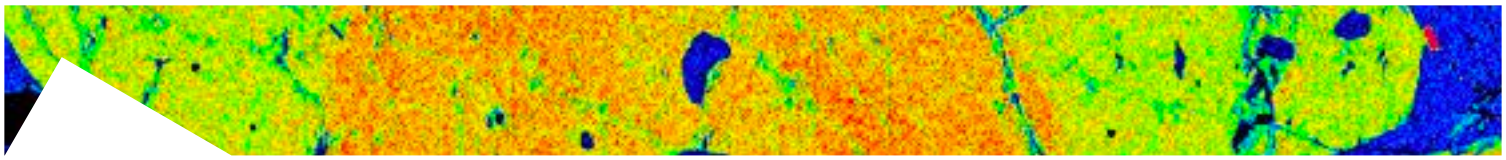

Giuliani L., Iezzi G., Vetere F., Nazzari M., Mollo S., Misiti V., Ventura G.
Effects of variable cooling rates on crystal-chemistry of solidified phases from a basaltic melt

Iezzi G., Giuliani L., Vetere F., Nazzari M., Mollo S., Cavallo A., Misiti V., Ventura G., Behrens H.
Solidification of silicate melts: an experimental perspective
Iezzi G., Giuliani L., Vetere F., Nazzari M., Mollo S., Cavallo A., Misiti V., Ventura G., Behrens H.
Solidification of silicate melts: an experimental perspective

Lanzafame G., Iezzi G., Ventura G., Mancini L., Tamburrino S., Behrens H., Mollo S., Signanini P.
Marsilian explosive phenomena investigated by analysis of proximal and distal deposits
Masotta M., Pontesilli A., Mollo S., Armienti P., Scarlato P.
Extremely fast magma dynamics at Mt. Etna revealed by clinopyroxene growth

Monaco L., Stagno V., Greaux S., Nazzari M., Irifune T.
Plagioclase records variable-H_2O contents in basaltic to andesitic magmas from Capo Marargiu Volcanic District (Sardinia, Italy)

Tecchiato V., Gaeta M., Mollo S., Perinelli C., Bachmann O., Scarlato P.
Plagioclase records variable-H_2O contents in basaltic to andesitic magmas from Capo Marargiu Volcanic District (Sardinia, Italy)

CITIES ON VOLCANOES General Assembly | Napoli, Italy | 2-7 September

Brenna M., Mollo S., Masotta M., Pontesilli A., Cronin S.
How to make phonolites? An experimental approach

Del Bello E., Taddeucci J., Merrison J., Alois S., Iversen J.J., Scarlato P.
Modelling the resuspension threshold of volcanic ash in dry and wet environments by wind-tunnel experiments at controlled humidity

Di Nezza M., Misiti V., D'Addezio G.
How could hand laboratory games will improve acknowledgement to the correct volcanic risk perception?

Di Stefano F., Mollo S., Scarlato P., Nazzari M., Bachmann O., Caruso M.
Olivine compositional changes in primitive skarn environments: A reassessment of divalent cation partitioning models to quantify the effect of carbonate assimilation

Forni F., Degruyter W., Bachmann O., De Astis G., Mollo S.
Insights into caldera cycles at Campi Flegrei by combining eruptive history, petrology, and numerical modelling

Forni F., De Astis G., Bachmann O., Petricca E., Piochi M., Mollo S.
The role of magma evolutionary processes and cumulate melting in the Campanian Ignimbrite and Neapolitan Yellow Tuff caldera-forming eruptions (Campi Flegrei, Southern Italy)

Nazzari M., Di Stefano F., Mollo S., Scarlato P., Tecchiato V., Ellis B., Bachmann O., Ferlito C.
Modeling the crystallization and emplacement conditions of a basaltic trachyandesitic sill at Mt. Etna volcano

Rausch J., Jaramillo Vogel D., Meier M., Swanson D., Ricci T., Pardo N., Avellaneda J.D.
Automated SEM/EDX morpho-chemical single particle (ash) analysis: A powerful tool to monitor active volcanoes and understand past volcanic activities

Robidoux P., Rizzo A.L., Aguilera F., Aiuppa A., Artale M., Liuzzo M., Nazzari M., Zummo F.
The $^{3}He/^{4}He$ signature of two Chilean volcanoes: Lascar and Lastarria.

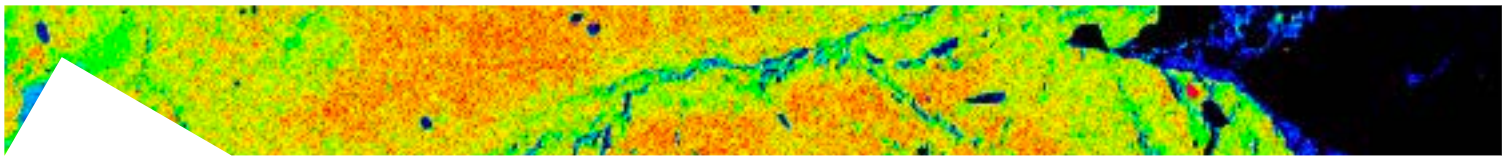

Taddeucci J., Salvatore V., Cigala V., Gaudin D., Pena-Fernandez J.J., Arciniega-Ceballos A., Kueppers U., Palladino D.M., Sesterhenn J.
Shock-tube investigation on jet development and pyroclast acceleration during transient explosive eruptions

Ubide T., Mollo S., Blundy J.B., Zhao J.X.,Nazzari M., Scarlato P.
Clinopyroxene sector zoning revisited: magma mixing vs. kinetic effects

Hyperspectral Imaging and Sounding of the Environment 2018 | Singapore | November

Taddeucci J., Scarlato P., Del Bello E., Tamburello, G., Gaudin D.
Eruptions from UV to TIR: multispectral high-speed imaging of explosive volcanic activity

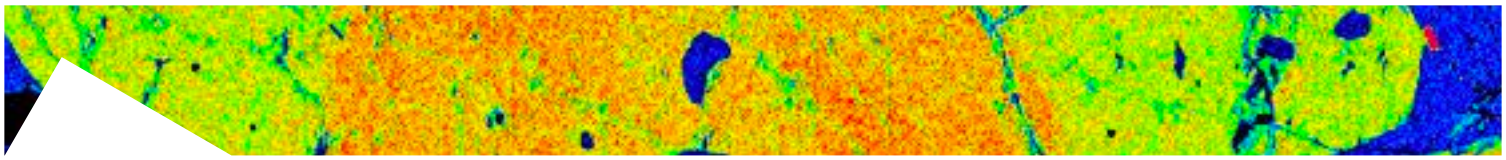

12| PUBLICATIONS

1. *Del Bello E., Taddeucci J., Merrison J., Alois S., Iversen J.J., Scarlato P.*
Experimental simulations of volcanic ash resuspension by wind under the effects of atmospheric humidity
Scientific Reports | 8, 14509

2. *Del Carlo P., Di Roberto A., D'Orazio M., Petrelli M., Angioletti A., Zanchetta G., Maggi V., Daga R., Nazzari M., Rocchi S.*
Late Glacial-Holocene tephra from southern Patagonia and Tierra del Fuego (Argentina, Chile): a complete textural and geochemical fingerprinting for distal correlations in the Southern Hemisphere
Quaternary Science Reviews | 195, 153-170

3. *Del Gaudio P., Ventura G.*
Flow Behavior of Clay-Silt to Sand-Silt Water-Rich Suspensions at Low to High Shear Rates: Implications for Slurries, Transitional Flows, and Submarine Debris-Flows
Acta Geologica Sinica | 92, 1685-1699

4. *Di Felice F., Mazzini A., Di Stefano G., Romeo G.*
Drone high resolution infrared imaging of the Lusi mud eruption
Marine and Petroleum Geology | 9, 38–51

5. *Di Nezza M., Misiti V., Castello B., Amici S., D'Addezio G.*
PROGETTO PILOTA PER LA SCUOLA DELL'INFANZIA: LABORATORI "A PROVA DI VULCANI E TERREMOTI"
Miscellanea | 41

6. *Di Stefano F., Mollo S., Scarlato P., Nazzari M., Bachmann O., Caruso M.*
Olivine compositional changes in primitive magmatic skarn environments: A reassessment of divalent cation partitioning models to quantify the effect of carbonate assimilation
Lithos | 316–317, 104–121

7. *Di Stefano G., Romeo G., Mazzini A., Iarocci A., Hadi S., Pelphrey S.*
The Lusi drone: A multidisciplinary tool to access extreme environments
Marine and Petroleum Geology | 90, 26-37

8. *Etiope G., Ifandi E., Nazzari M., Procesi M, Tsikouras B., Ventura G., Steele A., Tardini R., Szatmari P.*
Widespread abiotic methane in chromitites
Science Advances | 4, 9401

9. *Forni F., Degruyter W., Bachmann O., De Astis G., Mollo S.*
Long-term magmatic evolution reveals the beginning of a new caldera cycle at Campi Flegrei
Scientific Reports | 8, 1-10

10. *Forni F., Petricca E., Bachmann O., Mollo S., De Astis G., Piochi M.*
The role of magma mixing/mingling and cumulate melting in the Neapolitan Yellow Tuff caldera-forming eruption (Campi Flegrei, Southern Italy)
Contributions to Mineralogy and Petrology | 173, 45

11. *Giacomel P., Spagnuolo E., Nazzari M., Marzoli A., Passelegue F., Youbi N., Di Toro G.*
Frictional Instabilities and Carbonation of Basalts Triggered by Injection of Pressurized H_2O- and CO_2-Rich Fluids
Geophysical Research Letters | 45, 1-10, (GRL57585)

12. *Giacomoni P.P, Coltorti M., Mollo S., Ferlito C., Braiato M., Scarlato P.*
The 2011-2012 paroxysmal eruptions at Mt. Etna volcano: Insights on the vertically zoned plumbing system
Journal of Volcanology and Geothermal Research | 349, 370-391

13. *Gresse M., Vandemeulebrouck J., Byrdina S., Chiodini G., Roux P., Rinaldi A., Wathelet M., Ricci T., Letort J., Petrillo Z., Tuccimei P., Lucchetti C., Sciarra A.*
Anatomy of a fumarolic system inferred from a multiphysics approach
Scientific Reports | doi:10.1038/s41598-018-25448-y

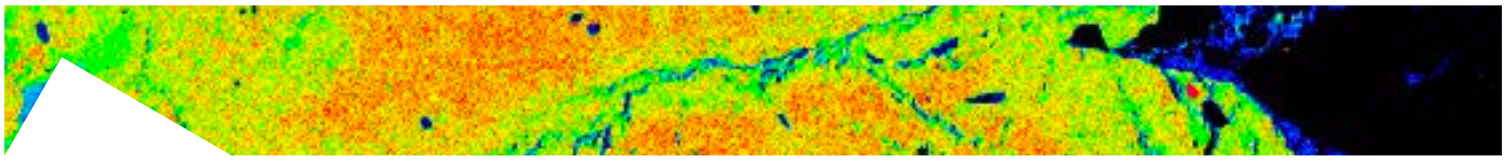

14. *Guimbretière G., Duraipandian S., Ricci T.*
Field remote Stokes/Anti-Stokes Raman characterization of sulfur in hydrothermal vents
Journal of Raman Spectrosc | doi:10.1002/jrs.5378

15. *Kirilova M., Toy V., Rooney J.S., Giorgetti C., Gordon, K.C., Collettini C., Takeshita T.*
Structural disorder of graphite and implications for graphite thermometry
Solid Earth | doi.org/10.5194/se-9-223-2018

16. *Leah H., Fondriest M., Lucca A., Storti F., Balsamo F., Di Toro G.*
Coseismic extension recorded within the damage zone of the Vado di Ferruccio Thrust Fault, Central Apennines, Italy
Journal of Structural Geology | 114, 121–138

17. *Lucci F., Della Ventura G., Conte A.M., Nazzari M., Scarlato P.*
Naturally Occurring Asbestos (NOA) in Granitoid Rocks, A Case Study from Sardinia (Italy)
Minerals | 8, 442–465

18. *Lupi M., Mazzini A., Sciarra A., Collignon M., Schmid D.W., Husein A., Romeo G., Obermann A., Karyono K.*
Enhanced hydrothermal processes at the new-born Lusi eruptive system, Indonesia
Journal of Volcanology and Geothermal Research | 366, 47–57

19. *Masotta M., Mollo S., Nazzari M., Tecchiato V., Scarlato P., Papale P., Bachmann O.*
Crystallization and partial melting of rhyolite and felsite rocks at Krafla volcano: A comparative approach based on mineral and glass chemistry of natural and experimental products
Chemical Geology | 483, 603-618

20. *Mercuri M., Scuderi M.M., Tesei T., Carminati E., Collettini C.*
Strength evolution of simulated carbonate-bearing faults: The role of normal stress and slip velocity
Journal of Structural Geology | doi.org/10.1016/j.jsg.2017.12.017

21. *Misiti V., Cavallo A., Natali M., Angeloni L., Reggente M., Bettucci A., Passeri D., Mura F., Vlassak J.J. Rossi M.*
Nanomechanical characterization of K-basalt from Roman comagmatic province: A preliminary study
American Institute of Physics | doi.org/10.1063/1.5047763

22. *Mollo S., Blundy J., Scarlato P., De Cristofaro S.P., Tecchiato V., Di Stefano F., Vetere F., Holtz F., Bachmann O.*
An integrated P-T-H_2O-lattice strain model to quantify the role of clinopyroxene fractionation on REE+Y and HFSE patterns of mafic alkaline magmas: Application to eruptions at Mt. Etna
Earth-Science Reviews | 185, 32-56

23. *Mollo S., Tuccimei P., Soligo M., Galli G., Scarlato P.*
Advancements in understanding the radon signal in volcanic areas: A laboratory approach based on rock physico-chemical changes
In Integrating Disaster Science and Management. Editors: PijushSamui, DookieKim, and Chandan Ghosh | Elsevier, 309-328

24. *Mueller S. P., Helo C., Keller F., Taddeucci J., Castro J.M.*
First experimental observations on melting and chemical modification of volcanic ash during lightning interaction
Scientific Reports | 8, 1389

25. *Murphy S., G. Di Toro, F. Romano, A. Scala, S. Lorito, E. Spagnuolo, S. Aretusini, G. Festa, A. Piatanesi, S. Nielsen*
Tsunamigenic earthquake simulations using experimentally derived friction laws
Earth and Planetary Science Letters | 486, 155-165

26. *Orellana L.F., Scuderi M.M., Collettini C., Violay M.*
Frictional Properties of Opalinus Clay: Implications for Nuclear Waste Storage
Journal of Geophysical Research: Solid Earth | doi.org/10.1002/ 2017JB014931

27. *Masotta M., Mollo S., Nazzari M., Tecchiato V., Scarlato P., Papale P., Bachmann O.*
Crystallization and partial melting of rhyolite and felsite rocks at Krafla volcano: A comparative approach based on mineral and glass chemistry of natural and experimental products
Chemical Geology | 483, 603-618

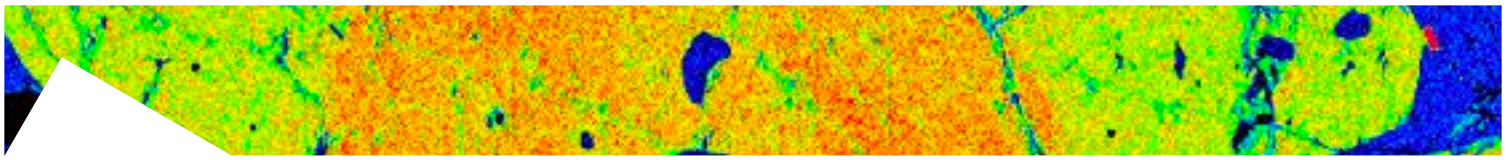

28. *Perinelli C., Mollo S., Gaeta M., De Cristofaro S.P., Palladino D.M., Scarlato P.*
Impulsive Supply of Volatile-Rich Magmas in the Shallow Plumbing System of Mt. Etna Volcano
Minerals | 8, 482

29. *Piacentini F., Coppolecchia A., de Bernardis P., Di Stefano G., Iarocci A., Lamagna L., Masi S., Peterzen S., Romeo G.*
Winter long duration stratospheric balloons from Polar regions
Mem. S. A. It. | 75, 282

30. *Rempe M., Mitchell T., Renner J., Smith S.A.F., Bistacchi A., Di Toro G.*
The relationship between microfracture damage and the physical properties of fault-related rocks: The Gole Larghe Fault Zone, Italian Southern Alps
Journal of Geophysical Research | 123, 7661-7687

31. *Revil A., Qi Y., Ghorbani A., Soueid Ahmed A., Ricci T., Labazuy P.*
Electrical conductivity and induced polarization investigations at Krafla volcano, Iceland
Journal of Volcanology and Geothermal Research | doi:10.1016/j.jvolgeores.2018.11.008

32. *Salvatore V., Silleni A., Corneli D., Taddeucci J., Palladino D.M., Sottili G., Bernini D., Andronico D., Cristaldi A.*
Parameterizing multi-vent activity at Stromboli Volcano (Aeolian Islands, Italy)
Bulletin of Volcanology | 80, 64

33. *Savage H., Rabinowitz H., Spagnuolo E., Aretusini S., Polissar P., Di Toro G.*
Biomarker thermal maturity experiments at earthquake slip rates
Earth and Planetary Science Letters | 502, 253-261

34. *Scuderi M.M., Collettini C.*
Fluid Injection and the Mechanics of Frictional Stabilityof Shale-Bearing Faults
Journal of Geophysical Research: Solid Earth | doi.org/10.1029/ 2018JB016084

35. T*addeucci J., Scarlato P., Del Bello E., Tamburello G., Gaudin D.*
Eruptions from UV to TIR: multispectral high-speed imaging of explosive volcanic activity
Hyperspectral Imaging and Sounding of the Environment

36. *Tecchiato V., Gaeta M., Mollo S., Bachmann O., von Quadt A., Scarlato P.*
Snapshots of primitive arc magma evolution recorded by clinopyroxene textural and compositional variations: The case of hybrid crystal-rich enclaves from Capo Marargiu Volcanic District (Sardinia, Italy)
American Mineralogist | 103, 899-910

37. *Tesei T., Harbord CWA., Collettini C., Viti C.*
Friction of Mineralogically Controlled Serpentinites and Implications for Fault Weakness
Journal of Geophysical Research: Solid Earth | doi.org/10.1029/ 2018JB016058

In press

38. *Di Stefano F., Mollo S., Blundy J., Scarlato P., Nazzari M., Bachmann O.*
The effect of CaO on the partitioning behavior of REE, Y and Sc between olivine and melt: Implications for basalt-carbonate interaction processes
Lithos

39. *Guerin-Marthe S., Nielsen S., Bird R., Di Toro G., Giani S.*
Earthquake Nucleation Size: Evidence of Loading Rate Dependence in Laboratory Faults
Journal of Geophysical Research | doi: 10.1029/2018JB016803

40. *Rowe C., Lamothe K., Rempe M., Andrews M., Mitchell T., Di Toro G., White J.C., Aretusini S.*
Earthquake lubrication and healing explained by amorphous nanosilica
Nature Communications

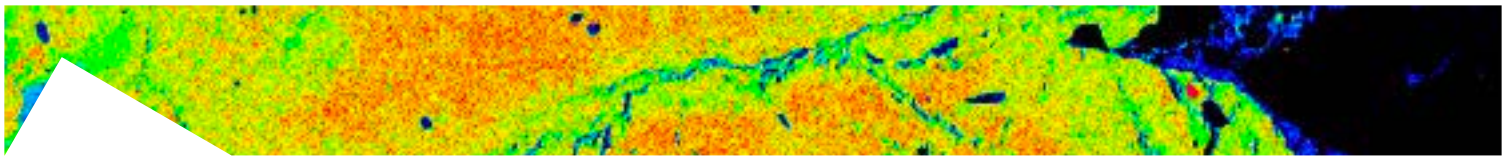

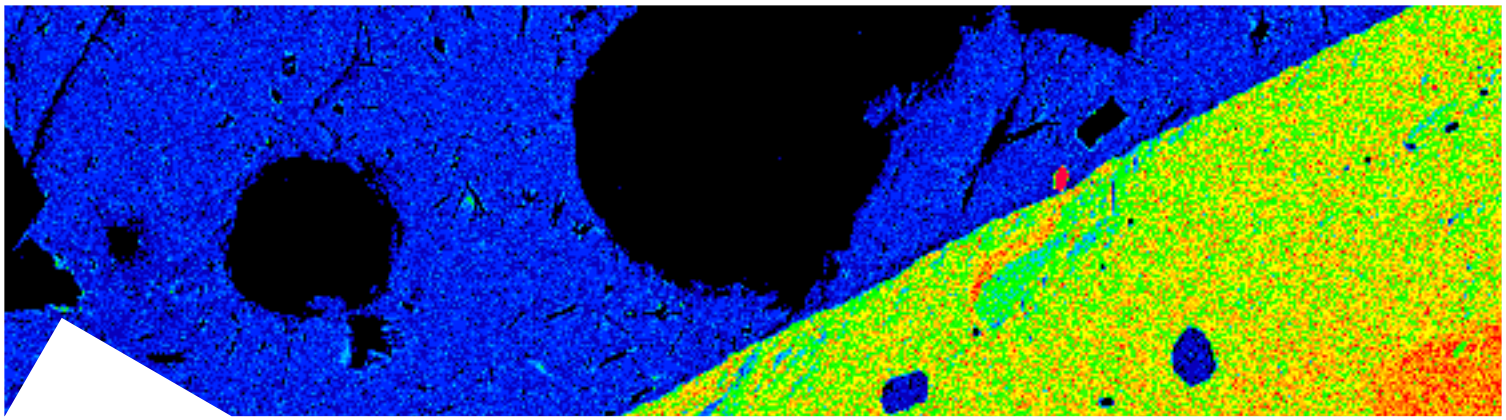

Design by
Laboratorio Grafica e Immagini INGV

Rome, 27 March 2019

Editing by Valeria Misiti